

Urban traffic resilience control - An ecological resilience perspective

Shengling Gao

School of Mathematical Sciences, Beihang University, Beijing, China. shengling_gao@buaa.edu.cn

Zhikun She

Corresponding author. School of Mathematical Sciences, Beihang University, Beijing, China. zhikun.she@buaa.edu.cn

Quanyi Liang

Co-Corresponding author. School of Mathematical Sciences, Beihang University, Beijing, China. qyliang@buaa.edu.cn

Nan Zheng

Co-Corresponding author. Institute of Transport Studies, Department of Civil Engineering, Monash University, Clayton, Australia. Nan.Zheng@monash.edu

Daqing Li

School of Reliability and Systems Engineering, Beihang University, Beijing, China. daqingl@buaa.edu.cn

Abstract. Urban traffic resilience has gained increased attention, with most studies adopting an engineering perspective that assumes a single optimal equilibrium and prioritizes local recovery. On the other hand, systems may possess multiple metastable states, and ecological resilience is the ability to switch between these states according to perturbations. Control strategies from these two different resilience perspectives yield distinct outcomes. In fact, ecological resilience oriented control has rarely been viewed in urban traffic, despite the fact that traffic system is a complex system in highly uncertain environment with possible multiple metastable states. This absence highlights the necessity for urban traffic ecological resilience definition. To bridge this gap, this paper defines urban traffic ecological resilience as the ability to absorb uncertain perturbations by shifting to alternative states. The goal is to generate a system with greater adaptability, without necessarily returning to the original equilibrium. Our control framework comprises three aspects: portraying the recoverable scopes; designing alternative steady states; and controlling system to shift to alternative steady states for adapting large disturbances. Among them, the recoverable scopes are portrayed by attraction region; the alternative steady states are set close to the optimal state and outside the attraction region of the original equilibrium; the controller needs to ensure the local stability of the alternative steady states, without changing the trajectories inside the attraction region of the original equilibrium as much as possible. Note that, this paper gives inner and outer estimations of attraction region with explicit algebraic expressions, as the attraction region for nonlinear systems are usually very complex and difficult to obtain. Comparisons with classical engineering resilience oriented urban traffic resilience control schemes show that, proposed ecological resilience oriented control schemes have better adaptability and can generate greater resilience. These results will contribute to the fundamental theory of future resilient intelligent transportation system.

Key words: Urban traffic resilience; resilience control; ecological resilience; macroscopic fundamental diagram; attraction region; stability; alternative steady state

1. Introduction

Traffic congestion is plaguing most of megacities (Huang et al. (2020a), Zeng et al. (2019)). Congested transportation systems are highly vulnerable, and often fall into collapse under extreme events such as poor weather and accidents. Such vulnerability of transportation network operations is a "persistent urban

disease". Therefore, how to sustain functional road transportation systems has been a long-standing research topic, in particular the challenging objective is to improve the resilience of operations towards uncertain perturbations.

Resilience, first proposed by [Holling \(1973\)](#) in the ecology field, denotes the system ability to absorb unexpected disturbances and to keep persistence. Over the past few decades, resilience has been greatly developed in various disciplines including ecology, engineering, and psychology ([Martin-Breen and Anderies \(2011\)](#), [Hosseini, Barker, and Ramirez-Marquez \(2016a\)](#)). In general, there are two perspectives on resilience: engineering resilience and ecological resilience ([Holling \(1996\)](#)). Noteworthy, this categorization of resilience is discipline-independent. One can use ball-and-cup heuristic to illustrate these two perspectives ([Scheffer et al. \(1993\)](#), [Rölfer, Celliers, and Abson \(2022\)](#), [Liao \(2012\)](#), [Walker et al. \(2004\)](#)), as shown in Fig. 1: when the ball is at the cup bottom, it symbolizes a steady state, known as an ‘‘attractor’’; the shape of the cup portrays the recoverable phase space of the corresponding attractor, usually described as the shape of potential function (landscape) or attraction basin; the yellow arrows represent perturbations and system responses. Fig. 1(a) illustrates the engineering resilience, which usually assumes there exists a single steady state and characterizes the system ability to absorb disturbances and recover to this single steady state. Studies related to engineering resilience typically aim at rapid local or global recovery of a single steady-state system ([Tilman and Downing \(1994\)](#), [O’Neill et al. \(1986\)](#), [Pimm \(1984\)](#)). In contrast, Fig. 1(b) shows the ecological resilience, which features multiple metastable states and the perturbations are absorbed through a multi-state shifting, without requiring the returning to a single steady state. Clearly, ecological resilience emphasizes persistence with uncertainty ([Holling \(1973\)](#), [Folke \(2006\)](#), [Zeng et al. \(2022\)](#)). As such, ecological resilience can transform a system under instability from one basin of attraction to another ([Holling \(1973\)](#)), even for cases where they are far from the stable equilibrium as defined otherwise in engineering resilience.

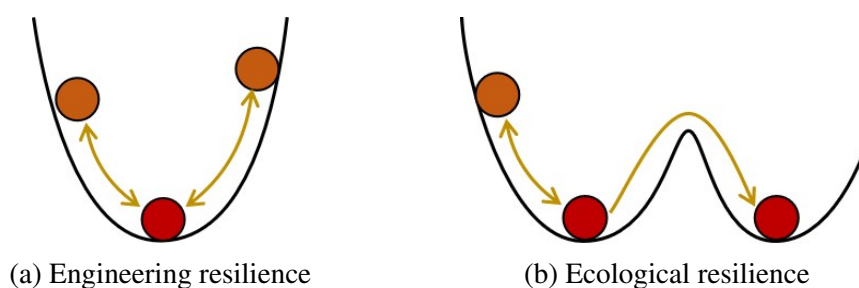


Figure 1 Schematic diagram of (a) engineering resilience and (b) ecological resilience ([Liao \(2012\)](#), [Rölfer, Celliers, and Abson \(2022\)](#))

Road network resilience is an emerging research subject. Most of the developed works are towards engineering resilience, aiming at a rapid recovery to a non-congested equilibrium or a single optimal equi-

librium. For example, the classic perimeter control schemes developed based on the macroscopic fundamental diagram (short for MFD) characterization of congestion dynamics, have received much attention in recent years (Geroliminis and Daganzo (2008), Haddad and Geroliminis (2012), Aghamohammadi and Laval (2020), Laval, Leclercq, and Chiabaut (2017), Johari et al. (2021), Haddad (2015), Khwais and Haddad (2022), Haddad and Zheng (2020), Mariotte, Leclercq, and Laval (2017), Haddad and Mirkin (2020), Ramezani, Haddad, and Geroliminis (2015), Li, Yildirimoglu, and Ramezani (2021), Mohajerpoor, Cai, and Ramezani (2023), Kouvelas, Saeedmanesh, and Geroliminis (2023), Tsitsokas, Kouvelas, and Geroliminis (2023), Yang, Menendez, and Zheng (2019), Dantsuji, Fukuda, and Zheng (2021), Ampountolas, Zheng, and Geroliminis (2017), Yang, Zheng, and Menendez (2018), Su et al. (2020)). The perimeter control schemes regulate the proportion of entering traffic at the perimeter of the networks via traffic signal control. In this direction, Haddad and Geroliminis (2012) calculated the "region of attraction" (short for RA) and designed a state feedback control to increase the RA for enlarging the recoverable area towards a single non-congested stable equilibrium. One pre-condition though, is that the system is within the states as defined by RA. In face of the so-called "hyper-congestion" which is far beyond the stable equilibrium state (e.g. a congestion density value twice as much as the critical density) and beyond RA, recovering to the desired system equilibrium cannot be guaranteed, and the system will inevitably fail, e.g. becoming unrecoverable grid lock. On the other hand, Zhong et al. (Zhong et al. (2020a, 2018a,b)) and Huang et al. (Huang et al. (2020b)) developed control schemes where the control would aim at a designated point, for example the point near the critical density or critical accumulation where the network flow reaches its maximum. However, the sufficient conditions of these controllers require that the disturbance to the systems, i.e. the incoming traffic demand to the road networks, cannot be high and fast-varying over time, which limits the controllability towards real world traffic situations. Most recently, Gao et al. (2022) proposed a novel control scheme based on RA, denoted as RCS-single, focusing specifically towards the recovery to the single optimal equilibrium from hyper-congested states. This is one of the first exploratory works looking at the "resilience" of system control. Nevertheless, this work was still within the framework of a single equilibrium system, and the recovery speed is very slow. For systems where instability is coupled with complex disturbances, in the case of hyper-congestions accompanied by persistently high travel demand, the existing controls are not only time-consuming, but also the objective of returning to single equilibrium is impractical. In literature, the impact of large changes in travel demand causing the instability of MFD was pointed out in multiple studies, such as Daganzo, Gayah, and Gonzales (2011), Zhong et al. (2020b), Haddad and Zheng (2020).

Urban traffic is a complex dynamic system, which may exist multiple metastable states (Zeng et al. (2020)). Given the above discussion on the limitation of the single-objective control schemes, a more realistic way appears to be guiding the system to switch between multiple metastable states under perturbations. While the engineering resilience-oriented system controls have its values, there is a need to address the

limitation towards system perturbations. Future resilient traffic system, that is capable of withstanding large and rapidly changing environments and contingencies, absorbing environmental uncertainties and developing different adaptive landscapes, would be by nature an ecosystem-like dynamic system. In other words, controlling such system should embrace an ecological perspective, where the ecological operation essentially enables the system to shift among alternative stable states (Holling (1996), Folke et al. (2010), Walker and Salt (2012), Gunderson (2000), Dakos and Kéfi (2022), Scoones et al. (2020)). Therefore, this work develops an ecological resilience control for managing congested urban road systems. The control aim is to enhance road traffic flow systems with greater adaptability towards different perturbations, such as congestion, unusual travel demand, sudden infrastructure closure, and accidents. Our work will, for the first time, provide an analytical modeling framework and the proves on system shifting between alternative steady states. Our work will demonstrate that such system is superior and much more resilient, comparing to controlled systems that aiming at returning to a single state, such as an original equilibrium or a pre-defined optimal state.

Built upon the MFD-based traffic flow representation system, this paper proposes a methodology for deriving ecological resilience control under large disturbances. Our control methodology comprises three aspects: portraying the recoverable system states, designing the target steady system states, and developing control mechanisms to regulate system towards steady states. Specifically, the RA framework will be adopted but extended, where the recoverable scopes are portrayed by attraction region; the alternative steady states are set close the optimal state and outside the attraction region of the original equilibrium; the controller is devised to guarantee the local stability of the alternative steady states, without changing the dynamics around the original equilibrium as much as possible. We showcase the proposed methodology in two-region road systems (i.e. two congested road networks whose traffic flow and congestion interact with each other, and each road network has its own MFD to describe its traffic dynamics). We first derive the explicit algebraic expressions of the boundaries of inner and outer estimations of the attraction regions. Building upon these theoretical boundary delineations, we then design two distinct resilience control schemes, denoted as RCS-1 and RCS-2, respectively. Considering a four-equilibria system as an illustration, we test two resilient control schemes. The control performance can be seen in Fig. 13 and Fig. 15 (more details and discussions will be provided in section 5). CPC (denotes constant perimeter control) and RCS-single (proposed by Gao et al. (2022)) are two benchmark methods. As a general remark, the proposed resilience control schemes and RCS-single can prevent the evolution of vehicle density (also called vehicle accumulation) n_1 or n_2 to jam vehicle density (corresponding to zero completion flow), while CPC is unable to impede such occurrences. Furthermore, the resilience measures summarized in Table 2 indicate that, RCS-1 and RCS-2 outperform RCS-single as they exhibit greater resilience measures in most cases, corresponding to smaller resilience triangle (resilience loss). This superiority stems from the ability

of RCS-1 and RCS-2 to guide the trajectories towards alternative stable states that are more easily attainable, thereby enhancing adaptability. Moreover, the local landscape (local Lyapunov function (Wang et al. (2021), Willems (1971), Blanchini (1995))) near the target point of controlled system with RCS-2 clearly shows the effect of our control scheme.

The main contributions of this study encompass three key aspects:

- (1) We establish a theoretical foundation for the approximate depiction of recoverable states for multi-equilibrium systems, by deriving the inner and outer estimations of attraction regions with explicit algebraic expressions for multi-equilibrium MFD dynamics, utilizing invariant sets. Note that the computation of RA for multiple equilibria nonlinear systems is especially intricate and hard to obtain.
- (2) We innovatively propose a leap from single-steady state control (from an engineering resilience perspective) to multi-steady states control (from an ecological resilience perspective), by leveraging the developed theory of approximate depiction of recoverable states and the stability theory of switch systems. This effort yields explicit control methodological, providing a clear pathway for the implementation of a control system that navigates across different stability landscapes.
- (3) We innovatively design a resilience measure utilizing the classical resilience triangle and completion flow. And it intuitively depicts the loss of completed trips compared to the maximum potential number of trips that could have been completed during the recovery period.

2. The control system dynamics and its ecological resilience

This paper showcases the advancement and performance of an ecological resilience-oriented control in a two-region system (known also as two-reservoir system in literature) traffic flow control problem, where the traffic dynamics of the two regions follow an MFD-based representation. Sec. 2.1 firstly gives the mathematical description of the MFD-based modeling framework, Sec. 2.2 illustrates the ecological resilience control framework for MFD dynamics, and then Sec. 2.3 defines ecological resilience measure.

2.1. Two-region MFD dynamics

To start with, we consider a two-region MFD system, illustrated in Fig. 2. The urban traffic network is partitioned into three parts: Region 1, Region 2, and the Outside. Our primary focus lies on Regions 1 and 2, and each endowed with its own MFD. The MFD delineates the correlation between the travel completion flow $G_i(n_i(t))$ and vehicle accumulation (density) n_i of region i at time t , manifesting a single peak, characterized by an initial ascent succeeded by a descent. Classical perimeter control methodologies regulate the traffic flow ratio entering Regions 2 and 1 through signal controls, denoted as allowed pass rates u_1 and u_2 . As illustrated in Fig. 2, for each region at time t , there are two inflows (marked as gray arrows directed toward region i) and one completion flow $G_i(n_i(t))$ (marked as gray circle). The first inflow, $u_j G_j(n_j(t))$ ($j = 1, 2, j \neq i$) signifies the allowed traffic inflow transferred from j to i with the pass rate u_j . The second inflow,

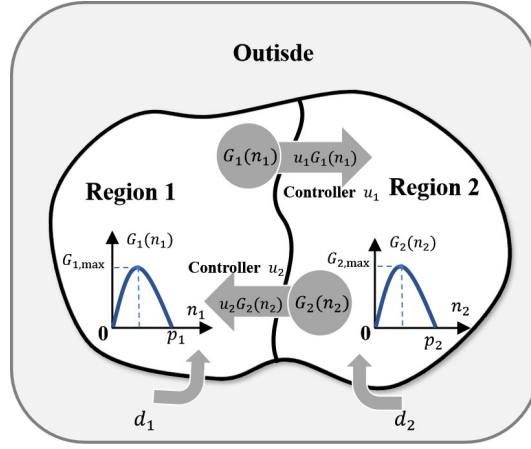


Figure 2 Two region MFD dynamics (Aboudolas and Geroliminis (2013), Gao et al. (2022)).

denoted as d_i , represents the fixed net inflow from the outside to i , encapsulating uncontrollable demand, commonly known as disturbance.

The model can be described by MFD dynamic (Aboudolas and Geroliminis (2013), Gao et al. (2022)):

$$\begin{aligned} \frac{dn_1(t)}{dt} &= F_1(n_1(t), n_2(t)) := -G_1(n_1(t)) + u_2 G_2(n_2(t)) + d_1, \\ \frac{dn_2(t)}{dt} &= F_2(n_1(t), n_2(t)) := -G_2(n_2(t)) + u_1 G_1(n_1(t)) + d_2, \end{aligned} \quad (1)$$

with the boundary condition:

$$\begin{aligned} 0 &\leq n_1(t) \leq p_1, 0 \leq n_2(t) \leq p_2, \\ 0 &\leq u_1 \leq u_{1,max}, u_{1,max} = \min \left\{ 1, \frac{G_{2,max}}{G_{1,max}} \right\}, \\ 0 &\leq u_2 \leq u_{2,max}, u_{2,max} = \min \left\{ 1, \frac{G_{1,max}}{G_{2,max}} \right\}. \end{aligned} \quad (2)$$

Let $\mathbf{n} = (n_1(t), n_2(t))$, $\mathbf{F}(\mathbf{n}) = ((F_1(n_1(t), n_2(t)), F_2(n_1(t), n_2(t))))$, and $\dot{\mathbf{n}} = \frac{d\mathbf{n}}{dt}$, system (1) can be simplified to $\dot{\mathbf{n}} = \mathbf{F}(\mathbf{n})$. Note that perimeter controllers u_1 and u_2 are assumed to be constants. Therefore, they can be denoted as constant perimeter control, short for CPC. The fixed net inflow d_i is also assumed to be constants. Moreover, as a realistic scene, we here use the parabolic-MFD: $G_i(n_i) = -a_i n_i (n_i - p_i)$ with opening size $a_i > 0$ and jam accumulation p_i of region i , as shown in Fig. 2 and Fig. 3. Then we have the maximum capacity $G_{i,max} = \frac{a_i p_i^2}{4}$ at the critical vehicle accumulation $\frac{p_i}{2}$. Note that $d_j \leq G_{j,max}$, $u_i G_{i,max} \leq G_{j,max}$ and $u_1 \times u_2 \neq 1$ are satisfied to avoid overflow. Without loss of generality, we can assume $G_{1,max} \leq G_{2,max}$, then the condition of u_1 and u_2 in Eq. (2) can be simplified as Condition (H):

$$0 \leq u_1 \leq 1, 0 \leq u_2 \leq \frac{G_{1,max}}{G_{2,max}}, \text{ but } u_1 \times u_2 \neq 1. \quad (3)$$

For the two-region MFD dynamic (1) with boundary condition (2) under traffic demand (d_1, d_2) , given the MFD function $(G_1(n_1), G_2(n_2))$, we aim to generate a transportation system from ecological resilience perspective by combining the stability characteristics of the MFD dynamics.

To achieve this objective, we first introduce concepts related to stability characteristics. The stability characteristics can be elucidated by phase portrait, where the phase portrait is a geometric representation of the dynamic system trajectories on the phase plane. As shown in Fig. 3(a), the phase plane is $n_1 - n_2$, and each point (state) in $n_1 - n_2$ plane denotes the vehicle accumulation in two regions. Progressing to the right or upward along the $n_1 - n_2$ plane signifies a corresponding increase in the vehicle accumulation within Region 1 (Region 2). Moreover, the axis n_2 in Fig. 3(a) corresponds to the ordinate of the right MFD and axis n_1 corresponds to the abscissa of the upper MFD. The completion flow $G_1(n_1)(G_2(n_2))$ increases with the vehicle accumulation before the critical vehicle accumulation $\frac{p_1}{2}(\frac{p_2}{2})$, reaching a peak $G_{1,max} (G_{2,max})$, and subsequently decreases until it diminishes to zero at the right (upper) boundary, signifying a traffic jam. As shown in Fig. 3(a), the attraction region (light pink region) of the equilibrium point $\mathbf{n}^0 = (n_1^0, n_2^0)$ (green circle) is a set of the initial points. The trajectories start from these initial points will converge towards \mathbf{n}^0 , while trajectories start from outside attraction region will move away from \mathbf{n}^0 and towards either the upper or right boundary. Note that equilibrium point $\mathbf{n}^0 = (n_1^0, n_2^0)$ satisfies $F_1(n_1^0, n_2^0) = 0$, $F_2(n_1^0, n_2^0) = 0$. We can introduce the definition of attraction region for the general equilibrium $\mathbf{n}^* = (n_1^*, n_2^*)$ as follows:

DEFINITION 1. (Gao et al. (2022)) For system (1) with boundary restrictions (2), denoting $n(t) = (n_1(t), n_2(t))$ and $\mathbb{D} = \{(n_1(t), n_2(t)) | 0 \leq n_i(t) \leq p_i, i = 1, 2\}$, define

$$\mathcal{R}(n^*) = \left\{ n_{init} \in \mathbb{D} | n(0) = n_{init} \text{ and } \lim_{t \rightarrow +\infty} n(t) = n^* \right\}, \quad (4)$$

as the attraction region for $\mathbf{n}^* = (n_1^*, n_2^*)$.

Note that, the classical concept of the "attraction domain" was originally defined for asymptotically stable equilibria (Wang, She, and Ge (2020b), Zheng et al. (2018), Ratschan and She (2010), Wang, She, and Ge (2020a)). Especially, for MFD dynamic (1), Gao et al. (2022) defined the "attraction region" for the unstable single equilibrium point. Differently, we here in this paper define for the general equilibrium (n_1^*, n_2^*) , including both unstable equilibrium and stable equilibrium.

2.2. Ecological resilience control framework for MFD dynamics

In the traffic flow theory and traffic control community, how to recover the traffic system from congestion has been a challenging research question. The classical perimeter control schemes, which utilizes MFD as references for optimal control, target on recovering the traffic system to a specified equilibrium. Such schemes are known to be constrained and uneconomical for hyper-congestion conditions, because these conditions are far from the single optimal control objective and there exist complex dynamics in the system that prevent the system from even getting closer to the targeted equilibrium. For this reason, our approach defines a new control objective, built upon which a corresponding control methodology is developed.

In essence, ecological resilience considers the existence of multiple metastable states in a dynamic system, and it enables the system to shift between states as a way to absorb or adapt to rapid external changes.

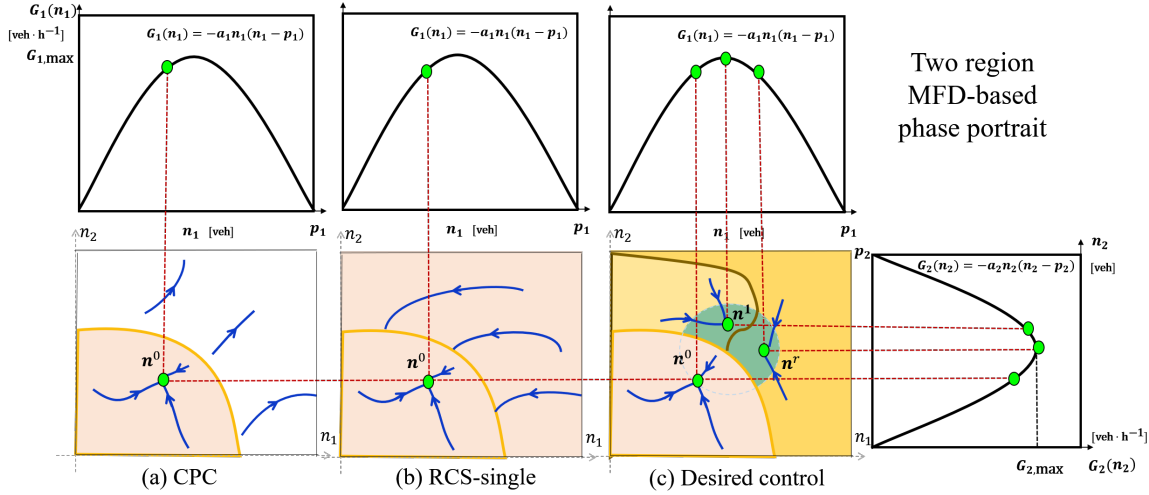


Figure 3 Schematic representation of the phase portraits under (a) CPC, (b) RCS-single, and (c) desired control. Note that desired phase portraits exhibit multiple metastable states. The attraction region of each metastable state is demarcated by different colors. The green area signifies the selectable range of the alternative steady states. the green circle represents the steady states; the blue lines with arrows depict state trajectories, indicating the evolution of a point (state) over time. The phase portraits and the Macroscopic Fundamental Diagram (MFD) exhibit a correlation. Each point in the phase portraits corresponds to the vehicle density (accumulation) in two regions, and the corresponding completion flows can be identified on the MFD.

Inspired by this nature, we aim to construct an ecological resilience traffic system resembling Fig. 3(c), with multiple metastable states (marked as green circles), where multiple metastable states includes the original uncongested equilibrium \mathbf{n}^0 and alternative steady states $\mathbf{n}^i = (n_1^i, n_2^i)$ ($i = 1, \dots, r$ with number of alternative steady states r).

To generate the ecological resilience traffic system resembling Fig. 3(c), our first critical issue is how to select multiple metastable states. Initially, we aim to leverage the inherent landscape of the system as much as possible. Therefore, we preserve the original non-congested equilibrium point of the system, denoted as \mathbf{n}^0 . This point coincidentally aligns with the single equilibrium point set by the classical CPC control system (as shown in Fig. 3(a)) or the single equilibrium point of the RCS-single control system proposed by Gao et al. (2022) (as depicted in Fig. 3(b)), satisfying $F_1(\mathbf{n}^0) = 0$, $F_2(\mathbf{n}^0) = 0$. After determining \mathbf{n}^0 , the next step involves selecting alternative stable states $\mathbf{n}^i = (n_1^i, n_2^i)$. There are two key criteria for selecting alternative stable states: one to position them as close to the optimal and critical vehicle accumulation $(\frac{p_1}{2}, \frac{p_2}{2})$ as possible; the other is to position them outside the attraction region $\mathcal{R}(\mathbf{n}^0)$ (depicted in the light pink region) of the original non-congested equilibrium point \mathbf{n}^0 . The first criterion seeks to increase the completion flow, given that such completion flow tends to decline as the vehicle accumulation gets further from the critical vehicle accumulation (see Fig. 3(c)). The second criterion is crucial because states within the attraction region of \mathbf{n}^0 will spontaneously recover to \mathbf{n}^0 . Here, we provide a quantitative description of the selectable

range. For the first criterion, we aim to select $\mathbf{n}^i = (x, y)$, such that the absolute distance between completion flow $(G_1(x), G_2(y))$ and maximum completion flow $(G_{1,max}, G_{2,max})$ is less than Δ_0 , where Δ_0 denotes the absolute distance between completion flow of the original equilibrium \mathbf{n}^0 and maximum completion flow. That is,

$$|G_1(x) - G_{1,max}| + |G_2(y) - G_{2,max}| \leq \Delta_0, \quad (5)$$

substituting $G_i(n_i) = -a_i n_i (n_i - p_i)$ and $G_{i,max} = \frac{a_i p_i^2}{4}$, yields

$$\mathcal{E} = \left\{ (x, y) \mid \frac{(x - \frac{p_1}{2})^2}{a_2} + \frac{(y - \frac{p_2}{2})^2}{a_1} \leq \frac{\Delta_0}{a_1 a_2} \right\}, \quad (6)$$

\mathcal{E} corresponds to the interior of an ellipse. Combining the second criterion, the selectable range of alternative stable states \mathcal{S} is

$$\mathcal{S} = \left\{ (x, y) \mid (x, y) \in \mathcal{E} \wedge (x, y) \notin \mathcal{R} \right\}, \quad (7)$$

as the green region shown in Fig. 3(c).

Once multiple metastable states have been chosen, the next consideration is how to devise a control scheme that enables the system to recover to appropriate steady states. Controlling a system with multi-steady states poses more challenges compared to a system with a single stable state. The first challenge lies in determining which state the system should recover to, and the second challenge is devising a strategy to facilitate the system recovery to the respective target stable state. To address the first challenge, we need to identify the attraction region of the original equilibrium. It is essential to note that, for nonlinear systems, the attraction region is typically intricate, and obtaining explicit algebraic expressions for it can be challenging. In this direction, [Gao et al. \(2022\)](#) derived the attraction region with explicit algebraic expressions for the single-equilibrium MFD dynamics. Different from their work, we consider multi-equilibria (including two-equilibria and four-equilibria) systems in this paper. Given the involvement of multiple equilibrium points and nontrivial boundary shapes, their approach can not be applicable here. To this end, our first effort is the estimation of the attraction region for the multi-equilibria systems (see Sec. 3 and App. A). Upon obtaining an estimation of the attraction region with explicit expressions for the boundaries (including inner and outer estimations) of the original uncongested equilibrium point, a natural boundary between the original uncongested equilibrium and the alternative steady state emerges.

The second challenge, i.e., how to devise a strategy to facilitate the system recovery to the respective target steady state is also intricate. To tackle this issue, we make a second effort using a switched controlled system and design two control schemes based on the inner and outer estimations of the attraction region (see Sec. 4). It is essential to emphasize that [Gao et al. \(2022\)](#) also explored this direction. Their switched controlled system is depicted in Fig. 3(b), where trajectories originating outside the attraction region are directed towards its boundary before spontaneously converging towards the single equilibrium. The proposed control, however, addresses a significantly different and more complex problem. We aim to utilize

the escaped trajectories (from attraction region) and guide them to appropriate steady points. Therefore, this novel framework faces new technical barriers, namely how to find a feasible control that can recover system to ε – *Neighborhood* of target point (\bar{n}_1, \bar{n}_2) within recovery time t_f under corresponding perturbations, where ε denotes an arbitrarily small positive number; and ε – *Neighborhood* of a state (\bar{n}_1, \bar{n}_2) is described as the set $\{(n_1, n_2) : (n_1 - \bar{n}_1)^2 + (n_2 - \bar{n}_2)^2 \leq \varepsilon\}$. Note that the target point (\bar{n}_1, \bar{n}_2) can be any state in multiple metastable states, depending on the size of the perturbation; and system can switch between multiple metastable states in facing with different perturbations. Moreover, the system can also switch between optimal and suboptimal states, if the optimal state satisfies the conditions of the alternative steady states.

2.3. Measuring urban traffic resilience

We have depicted the envisioned ecological traffic resilience system and presented the resilience control framework. However, a quantitative indicator for traffic ecological resilience is still absent. It is imperative to establish a quantitative measure for traffic ecological resilience, thereby enhancing a more intuitive perception of the ecological resilience of traffic and facilitating a more straightforward evaluation and reference for control effectiveness.

The quantitative assessment of resilience can be categorized into two main types: general resilience measure methods and structure-based model-driven resilience measure (Hosseini, Barker, and Ramirez-Marquez (2016b)). We prioritize general resilience measure in this paper, given that the second type is more reliant on specific models. Among general resilience measure, the “resilience triangle” introduced in Bruneau et al. (2003) has gained notable attention. Originally designed for assessing a community resilience loss during earthquakes, it calculates the resilience loss through a definite integral:

$$RL = \int_{t_0}^{t_1} (1 - Q(t)) dt, \quad (8)$$

where $Q(t)$ represents community service quality at time t , expressed as a percentage scale from 0 to 100%. $Q(t)$ starts declining at t_0 and returns to the normal state at t_1 . The deviation between the quality of degraded infrastructure and the normal infrastructure quality is quantified through $1 - Q(t)$. A higher RL indicates lower resilience, while a lower RL suggests higher resilience.

In this direction, Gao et al. (2022) marks one of the initial attempts to provide a quantitative interpretation of urban traffic resilience. They defined urban traffic resilience as the integral of the absolute deviation between vehicle density (vehicle accumulation) and the optimal vehicle density during the recovery period. However, the defined resilience measure lacks an evident physical interpretation. Thus, we revise the definition of deviation $D_s(t)$ as the difference between the completion flow $G_i(n_i)$ ($i = 1, 2$) and the maximum completion flow $G_{i,max}$. That is:

$$D_s(t) = |G_1(n_1) - G_{1,max}| + |G_2(n_2) - G_{2,max}|. \quad (9)$$

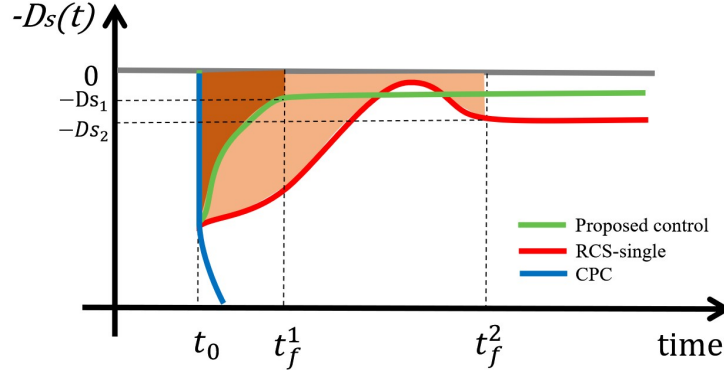


Figure 4 Schematic representation of resilience triangle. Here we consider hyper-congestion (large $D_s(t_0)$) scenario, and we assume that the original equilibrium is a non-congested equilibrium (not the optimal state). CPC is unable to recover the system, and instead leading to a rapid collapse. Proposed control (RCS-single) recovers the system to a functional level with deviation $-Ds_1$ ($-Ds_2$) from the maximum completion flow at t_f^1 (t_f^2), having a smaller (larger) resilience loss, depicted as the dark (light) brown shaded region. Note that the resilience loss is the absolute value of the area enclosed by the resilience triangle. Proposed control outperforms RCS-single, as proposed control can recover system to a functional state with less deviation ($Ds_1 < Ds_2$) faster ($t_f^1 < t_f^2$).

Note that, the unit of $D_s(t)$ is $[veh/h]$. Based on the defined $D_s(t)$, we can define the ecological traffic resilience measure as follows:

$$R = \int_{t_0}^{t_f} (0 - D_s(t)) dt = - \int_{t_0}^{t_f} D_s(t) dt. \quad (10)$$

Here t_f is the time when system recovers and stabilizes at functional steady states. Formula (10) implies that R is negative. Thus, $-R$ corresponds to the area of the resilience triangle, depicted as the dark brown shaded region in 4. Noteworthy, the unit of resilience measure R is $[veh]$, and it denotes the loss of completed trips compared to the maximum potential number of trips that could have been completed during the recovery period.

We depict a schematic diagram of the resilience triangle under three different controls, as shown in Fig. 4. Notably, under hyper-congestion, CPC fails to recover system and instead rapidly collapses system; while RCS-single and the proposed control can ensure recoverability. The resilience control proposed in this paper outperforms RCS-single, as it enables the system to recover to an alternative stable states with higher completion flow within a shorter time. Thus, the resilience triangle (loss) under our proposed control method (the dark brown area in Fig. 4) is smaller than that of RCS-single (the light brown area). Note that the original equilibrium is assumed to be a stable non-congested state, rather than an optimal state.

3. Stability analysis and spontaneous attraction region estimation for multi-equilibria system

In the previous section, for multi-equilibria system, we defined ecological resilience of urban traffic with an MFD-based representation. In this section, we will derive the global phase portrait and the spontaneous

attraction region for the multi-equilibria system under CPC (u_1 and u_2). Sec. 3.1 discusses and verifies the local stability of the MFD dynamic; Sec. 3.2 derives and illustrates the global phase portrait; and Sec. 3.3 presents the estimation of spontaneous attraction region that are used to design the proposed control in Sec. 4. Note that multiple equilibria systems include both two-equilibrium systems and four-equilibrium systems. According to Gao et al. (2022), two equilibria exist if and only if Condition (\mathbb{K}^{2a}): $\frac{u_2 d_2 + d_1}{1 - u_1 u_2} = G_{1,max} \wedge \frac{u_1 d_1 + d_2}{1 - u_1 u_2} < G_{2,max}$ or Condition (\mathbb{K}^{2b}): $\frac{u_2 d_2 + d_1}{1 - u_1 u_2} < G_{1,max} \wedge \frac{u_1 d_1 + d_2}{1 - u_1 u_2} = G_{2,max}$ holds; four equilibria exist if and only if Condition (\mathbb{K}^4): $\frac{u_2 d_2 + d_1}{1 - u_1 u_2} < G_{1,max} \wedge \frac{u_1 d_1 + d_2}{1 - u_1 u_2} < G_{2,max}$ holds. We in this section mainly present the theoretical analysis for two-equilibria system. The theoretical analysis for four-equilibria system can be found in App A.

3.1. Local stability verification

Consider the two-equilibria case with Condition (\mathbb{K}^{2a}). According to Condition (\mathbb{K}^{2a}), we have:

$$\begin{aligned} d_1 &= (1 - u_1 u_2) G_{1,max} - u_2 d_2, \\ d_2 &< G_{2,max} - u_1 G_{1,max}. \end{aligned} \quad (11)$$

Bringing the first equation of (11) into system (1), the system dynamics become:

$$\begin{aligned} \frac{dn_1(t)}{dt} &= -u_2 a_2 (n_2(t) - \frac{p_2}{2})^2 + a_1 (n_1(t) - \frac{p_1}{2})^2 + u_2 \left(\frac{a_2 p_2^2}{4} - u_1 \frac{a_1 p_1^2}{4} - d_2 \right), \\ \frac{dn_2(t)}{dt} &= -u_1 a_1 (n_1(t) - \frac{p_1}{2})^2 + a_2 (n_2(t) - \frac{p_2}{2})^2 + \left(\frac{u_1 a_1 p_1^2}{4} - \frac{a_2 p_2^2}{4} + d_2 \right). \end{aligned} \quad (12)$$

For systems (12), the two equilibria can be denoted as $P_k^{2a} = (\frac{p_1}{2}, p_k^{2a})$ ($k = 1, 2$), where $p_k^{2a} = \frac{p_2 + (-1)^k \times M}{2}$, $M = \sqrt{p_2^2 - \frac{4d_2 + u_1 a_1 p_1^2}{a_2}}$. Upon substituting Formula (11) into Formula (1), the system (1) reduces by one variable, d_1 , significantly simplifying our analysis. However, Formula (12) remains cumbersome. To further simplify the system for subsequent analysis, we shift equilibrium point P_1^{2a} of the system (12) to $(0, 0)$. That is, letting $x_1(t) = n_1(t) - \frac{p_1}{2}$ and $x_2(t) = n_2(t) - p_1^{2a}$, we can simplify system (12) as:

$$\begin{aligned} \frac{dx_1(t)}{dt} &= H_1^{2a}(x_1(t), x_2(t)) := u_2 a_2 M x_2(t) + (a_1 x_1^2(t) - u_2 a_2 x_2^2(t)), \\ \frac{dx_2(t)}{dt} &= H_2^{2a}(x_2(t), x_2(t)) := -a_2 M x_2(t) + (-u_1 a_1 x_1^2(t) + a_2 x_2^2(t)), \end{aligned} \quad (13)$$

The two equilibria for the new system (13) are $\hat{P}_1^{2a} = (0, 0)$ and $\hat{P}_2^{2a} = (0, M)$. Noteworthy, system (13) possesses the same properties as system (12) since system (13) is obtained by shifting system (12). Due to the simpler formulation of system (13), we in the following use system (13) to derive local stability characteristics, global phase portraits, and attraction region estimations. The properties obtained are equally valid for system (12). Therefore, all our propositions and theorems are summarized for system (12).

From the aforementioned conversion, we derive the following proposition for its two equilibria.

PROPOSITION 1. *Under Condition (\mathbb{H}), the two equilibria P_1^{2a} and P_2^{2a} of system (12) are both saddle-node points.*

Proof: We have that P_1^{2a} and P_2^{2a} of system (12) are equivalent to \hat{P}_1^{2a} and \hat{P}_2^{2a} of system (13), thus we consider the stability of \hat{P}_1^{2a} and \hat{P}_2^{2a} . For \hat{P}_1^{2a} , we have $\left(\begin{array}{cc} \frac{\partial H_1^{2a}(x_1, x_2)}{\partial x_1} & \frac{\partial H_1^{2a}(x_1, x_2)}{\partial x_2} \\ \frac{\partial H_2^{2a}(x_1, x_2)}{\partial x_1} & \frac{\partial H_2^{2a}(x_1, x_2)}{\partial x_2} \end{array} \right) \Big|_{(0,0)} = \begin{pmatrix} 0 & u_2 a_2 M \\ 0 & -a_2 M \end{pmatrix}$, indicating that:

$$\text{Rank} \left\{ \left(\begin{array}{cc} \frac{\partial H_1^{2a}(x_1, x_2)}{\partial x_1} & \frac{\partial H_1^{2a}(x_1, x_2)}{\partial x_2} \\ \frac{\partial H_2^{2a}(x_1, x_2)}{\partial x_1} & \frac{\partial H_2^{2a}(x_1, x_2)}{\partial x_2} \end{array} \right) \right\} \Big|_{(0,0)} = 1,$$

and

$$\text{div}(H_1^{2a}, H_2^{2a})|_{(0,0)} = \frac{\partial H_1^{2a}(0,0)}{\partial x_1} + \frac{\partial H_2^{2a}(0,0)}{\partial x_2} \neq 0.$$

According to Theorem 7.1 in Zhang (2006), we can analyze the nature of equilibrium points \hat{P}_1^{2a} by calculating the bifurcation function $B(x_1(t))$ (defined in Zhang (2006)), yields:

$$B(x_1(t)) = H_1^{2a}(x_1, x_2(x_1)) = H_1^{2a}(x_1, \pm \sqrt{\frac{u_1 a_1 x_1^2}{a_2} + \frac{M^2}{4} + \frac{M}{2}}) = (1 - u_1 u_2) x_1^2(t),$$

where $x_2(x_1) = \pm \sqrt{\frac{u_1 a_1 x_1^2}{a_2} + \frac{M^2}{4} + \frac{M}{2}}$ is obtained by letting $H_2^{2a}(x_1, x_2) = 0$. Since Condition (H) holds, we have $B(x_1(t)) > 0$ holds for all $x_1(t) \in [-\frac{M}{2}, \frac{M}{2}]$ except $x_1(t) = 0$. Moreover, the power exponent of function $B(x_1(t))$ is 2. Thus, $(0,0)$ is a saddle-node point (see Zhang (2006) Theorem 7.1(iii)), indicating that P_1^{2a} is a saddle-node point. Similarly, we can prove that P_2^{2a} is a saddle-node point. \square

Proposition 1 reveals that, for system (1) under (\mathbb{K}^{2a}) , the two equilibria P_1^{2a} and P_2^{2a} are both saddle-node point. Similarly, for system (1) under (\mathbb{K}^{2b}) , we can also prove that two equilibria P_1^{2b} and P_2^{2b} are both saddle-node point. These results will help us to reveal the local stability of the two equilibria, which will assist in subsequent derivations of attraction region, providing foundation for understanding the global properties of the system.

For the four-equilibria system, we also try to capture the local stability through linearization, and the detailed analysis can be found in App. A.1. In App. A.1, we denote the four equilibria as P_m^4 ($m = 1, 2, 3, 4$), and we have that P_1^4 is a locally stable node, P_2^4 and P_3^4 are saddle points, P_4^4 is an unstable node, which can be summarized as Proposition 2 in App. A.1.

3.2. Global phase portrait derivation

To capture more properties of the system, we aim to delve further into its global nature. Global analysis of dynamical systems is often intricate, lacking a unified analytical approach. For MFD dynamics, we overcome this gap by first dividing the phase space into several subregions using demarcation lines, followed by delineating the trajectory trends within each subregion, and ultimately analyzing and deriving the global phase portrait leveraging the trajectory trends in each subregion. For simplicity in analysis, we continue to consider the more straightforward formulation of Formula (13). Note that, the aforementioned demarcation lines are obtained by solving $\frac{dx_1(t)}{dt} = 0$ or $\frac{dx_2(t)}{dt} = 0$ respectively. The trajectory trends in each region are determined by $\frac{dx_1(t)}{dt}$ and $\frac{dx_2(t)}{dt}$. For instance, if $\frac{dx_1(t)}{dt} > 0$ ($\frac{dx_2(t)}{dt} > 0$), the trajectories move to the right (upward),

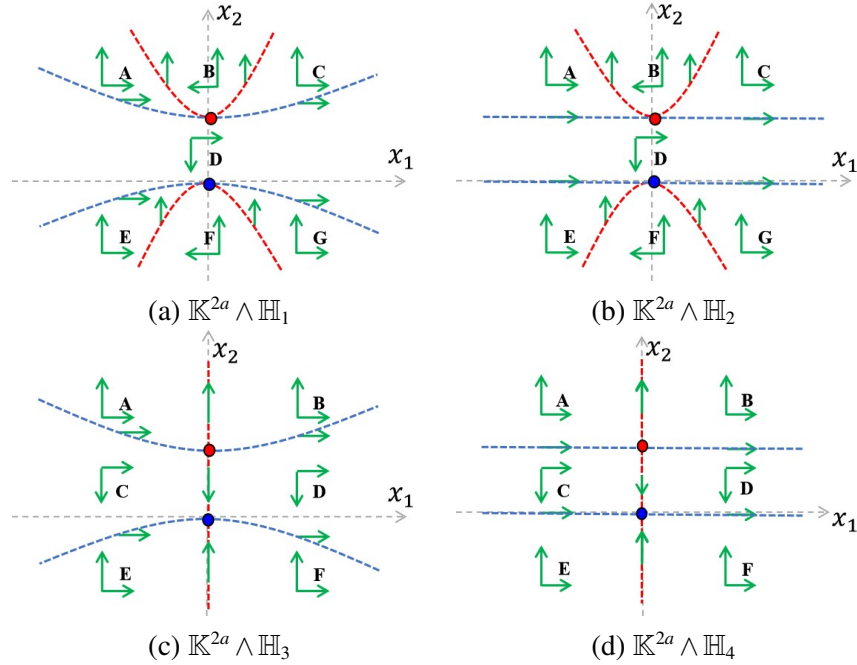


Figure 5 Theoretical schematic phase portraits of the two equilibria for system (13) under Condition $(\mathbb{K}^{2a} \wedge \mathbb{H})$. Red circle: undesired saddle-node equilibrium. Blue circle: desired saddle-node equilibrium. Red dotted curves: $\dot{x}_1 = 0$, blue dotted curves: $\dot{x}_2 = 0$, green arrows: trajectory directions.

while if $\frac{dx_1(t)}{dt} < 0$ ($\frac{dx_2(t)}{dt} < 0$), the trajectories move to the left (downward). Furthermore, considering that the demarcation lines $\frac{dx_1(t)}{dt} = 0$ or $\frac{dx_2(t)}{dt} = 0$ take different shapes under four distinct parameter conditions, we will separately examine these under four conditions.

First consider Condition (\mathbb{H}_1) : $0 < u_1, u_2 \leq 1 \wedge u_1 u_2 \neq 1$. Under this condition, both demarcation lines manifest as hyperbolas, illustrated by the red and blue dotted curves in Fig. 5(a), with the expressions $\frac{(x_2 - \frac{M}{2})^2}{\frac{M^2}{4}} - \frac{x_1^2}{\frac{u_2 a_2 M^2}{4a_1}} = 1$ and $\frac{(x_2 + \frac{M}{2})^2}{\frac{M^2}{4}} - \frac{x_1^2}{\frac{a_2 M^2}{4u_1 a_1}} = 1$. In addition, we have $\frac{dx_1(t)}{dt} = 0$ and $\frac{dx_2(t)}{dt} = (1 - u_1 u_2) a_2 x_2(t) (x_2(t) - M) > 0$ on the red dotted curves except for $(0, 0)$ and $(0, M)$; and we have $\frac{dx_2(t)}{dt} = 0$ and $\frac{dx_1(t)}{dt} = \frac{1 - u_1 u_2}{u_1} a_2 x_2(t) (x_2(t) - M) > 0$ on the blue dotted curves except for $(0, 0)$ and $(0, M)$. It is worth mentioning that, since $\frac{u_2 a_2 M^2}{4a_1} < \frac{a_2 M^2}{4u_1 a_1}$ holds, the location of these four curves are uniquely determined, as shown in Fig. 5(a). Then, the plane \mathbb{R}^2 can be divided into seven unbounded regions by these four curves. Moreover, Table 1 summarizes the symbols of $\frac{dx_i(t)}{dt}$ ($i = 1, 2$) in these seven regions. On the basis of Table 1, the phase portrait of (13) under Condition (\mathbb{H}_1) can be obtained, as shown in Fig. 5(a).

Table 1 Symbols of the seven regions for system (13) under Condition (\mathbb{H}_1) .

| Derivative | Symbol in region | | | | | | |
|----------------------|------------------|---|---|---|---|---|---|
| | A | B | C | D | E | F | G |
| $\frac{dx_1(t)}{dt}$ | + | - | + | + | + | - | + |
| $\frac{dx_2(t)}{dt}$ | + | + | + | - | + | + | + |

Subsequently, we can verify that regions B and E are both positive invariant sets by utilizing proof by contradiction. Given that the trajectories starting from B and E will not escape, we can further obtain that there exist no close orbits for system (13) under Condition (\mathbb{H}_1) .

When Condition $(\mathbb{H}_2): u_1 = 0 \wedge 0 < u_2 \leq 1$, $(\mathbb{H}_3): 0 < u_1 \leq 1 \wedge u_2 = 0$ or $(\mathbb{H}_4): u_1 = 0 \wedge u_2 = 0$ hold, the two demarcation lines can manifest as one hyperbola and one straight line (as shown in Fig. 5(b) and 5(c)) or as two straight lines (as shown in Fig. 5(d)). After obtaining the demarcation lines, we follow similar steps as above. As such, we verify that no close orbits exist under these conditions, and the corresponding phase portraits are illustrated in Fig. 5(b), 5(c) and 5(d). Similarly, we can also obtain the phase portrait for system (1) under Condition (\mathbb{K}^{2b}) , and there also exists no close orbit.

For the four-equilibria system, we also try to capture the global phase portraits, and the detailed analysis can be found in App. A.2. Note that the steps of global phase portrait derivation differ from that used for two-equilibrium system. Due to the increased number of equilibria, the combination of demarcation lines becomes intricately complex. On one hand, variations in demarcation line types (e.g., two hyperbolas, one hyperbola and one straight line, two straight lines, etc.) lead to different phase portraits. On the other hand, different relative positions of demarcation lines (e.g., whether the foci of two hyperbolas lie on the same axis) add another layer of complexity. The method for two equilibria are insufficient to address the challenges posed by four equilibria. Furthermore, the increased number of equilibrium points also hinders us from directly determining the locations of corresponding separatrices. New methods are required to capture the global phase portrait. We solve these in App. A.2 by subdividing Condition (\mathbb{K}^4) into five new distinct conditions. That is, Condition $(\hat{\mathbb{K}}_1^4): M_1 < 0 \wedge M_2 < 0$; Condition $(\hat{\mathbb{K}}_2^4): M_1 = 0 \wedge M_2 < 0$; Condition $(\hat{\mathbb{K}}_3^4): M_1 < 0 \wedge M_2 = 0$; Condition $(\hat{\mathbb{K}}_4^4): M_1 > 0 \wedge M_2 < \min\left\{-\frac{M_1}{u_2}, -u_1 M_1\right\}$; Condition $(\hat{\mathbb{K}}_5^4): M_1 < \min\left\{-u_2 M_2, -\frac{M_2}{u_1}\right\} \wedge M_2 > 0$, where $M_1 = d_1 + u_2 \frac{a_2 p_2^2}{4} - \frac{a_1 p_1^2}{4}$; and $M_2 = d_2 + u_1 \frac{a_1 p_1^2}{4} - \frac{a_2 p_2^2}{4}$. The five conditions mentioned above correspond to different positions of demarcation lines. In App. A.2, by discussing the shape of critical demarcation lines under each condition, we have summarized 20 distinct phase portraits for four-equilibria system and verifies that no closed orbit exists.

3.3. Spontaneous attraction region estimation

In the following, for two-equilibria system (12), the attraction region for the unstable saddle-node point P_1^{2a} will be derived. Note that, Gao et al. (2022) developed a method to find certain special trajectories, e.g., $x_2(t) = qx_1(t)$ for system with single-equilibrium. This form of special solution cannot apply here for multi-equilibrium systems. In this case, the theoretical attraction region boundaries are identified by finding certain separatrices of the equivalent systems (13), and the inner and outer attraction regions can be obtained by finding the positive invariant sets, under the aforementioned four conditions respectively.

Firstly, we consider Condition (IH₁). As shown in Fig. 6(a), the two red dotted demarcation curves can be denoted as $x_2 = \hat{r}_i^{2a}(x_1)$ ($i = 1, 2$), where $\hat{r}_i^{2a}(x_1) = (-1)^i \sqrt{\frac{a_1}{u_2 a_2} x_1^2 + \frac{M^2}{4}} + \frac{M}{2}$. Similarly, the two blue dotted demarcation lines can be denoted as $x_2 = \hat{b}_i^{2a}(x_1)$ ($i = 1, 2$), where $\hat{b}_i^{2a}(x_1) = (-1)^i \sqrt{\frac{u_1 a_1}{a_2} x_1^2 + \frac{M^2}{4}} + \frac{M}{2}$. Obviously, the vertexes of the demarcation lines are exactly the two equilibria $\hat{P}_1^{2a} = (0, 0)$ and $\hat{P}_2^{2a} = (0, M)$.

Assuming the lower blue dotted line $x_2 = \hat{b}_1^{2a}(x_1)$ intersects $x_1 = -k_1$ with $k_1 > 0$ at $(-k_1, x_D^1)$ and $(-k_1, x_D^2)$, where $x_D^1 < x_D^2$. The trajectory starting from $(-k_1, x_D^1)$ and $(-k_1, 0)$ will go into \hat{P}_1^{2a} in E as $t \rightarrow +\infty$; and the trajectory starting from $(-k_1, x_D^2)$ will escape A from the upper boundary of A and stay in B moving away from \hat{P}_1^{2a} as $t \rightarrow +\infty$. Thus, due to the continuous dependence theorem of solutions on initial conditions (Zhang (2006)), there exists a D^* with $0 < D^* < x_D^2$, such that the trajectory starting from any $(-k_1, x_D)$ with $0 < x_D \leq D^*$ will enter E and then go to \hat{P}_1^{2a} in E as $t \rightarrow +\infty$, and the trajectory starting from any $(-k_1, x_D)$ with $D^* < x_D \leq x_D^2$ will enter A, then escape A from the upper boundary of A and stay in B moving away from \hat{P}_1^{2a} as $t \rightarrow +\infty$. Thus, the trajectory starting from $(-k_1, x_{D^*})$, denoted as $\hat{\Phi}^1(\hat{P}_1^{2a}) = \hat{\Phi}_t^{2a,1}(-k_1, x_{D^*})$, is a stable separatrix of \hat{P}_1^{2a} , as shown in Fig. 6(a). Similarly, assuming the lower red dotted line $x_2 = \hat{r}_1^{2a}(x_1)$ intersect $x_2 = -k_2$ with $k_2 > 0$ at $(x_F^1, -k_2)$ and $(x_F^2, -k_2)$. By similar analysis, we can obtain that there exists an F^* with $0 < F^* < x_F^2$, such that the trajectory starting from any $(x_F, -k_2)$ with $0 < x_F \leq F^*$ will enter E and then go to \hat{P}_1^{2a} in E as $t \rightarrow +\infty$, and the trajectory starting from any $(x_F, -k_2)$ with $F^* < x_F \leq x_F^2$ will enter G, then escape G from the upper boundary of G and stay in D moving away from \hat{P}_1^{2a} as $t \rightarrow +\infty$. Thus, the trajectory starting from $(x_{F^*}, -k_2)$, denoted as $\hat{\Phi}^2(\hat{P}_1^{2a}) = \hat{\Phi}_t^{2a,2}(x_{F^*}, -k_2)$, is a stable separatrix of \hat{P}_1^{2a} , as shown in Fig. 6(a).

Subsequently, combining with phase portrait Fig. 5(a), we can verify that the region \hat{S}_m^{2a} is a positive invariant set utilizing proof by contradiction, where $\hat{S}_m^{2a} = \{(x_1, x_2) | x_i \leq 0, i = 1, 2\}$, depicted as the light blue zone in Fig. 6(a). Or else, there will be at least one trajectory originated from \hat{S}_m^{2a} , and enter \hat{V}_1^{2a} (or \hat{V}_2^{2a}) through the upper boundary (or right boundary) of \hat{S}_m^{2a} , where $\hat{V}_1^{2a} = \{(x_1, x_2) | x_1 < 0, 0 < x_2 < \hat{b}_2^{2a}(x_1)\}$ and $\hat{V}_2^{2a} = \{(x_1, x_2) | x_1 > 0, x_2 < \hat{r}_1^{2a}(x_1)\}$. Obviously, it is contradictory with the trajectory direction in phase portrait 5(a). Further, joining Fig. 6(a) with Fig. 5(a), we have that: the trajectory starting from any point in $D \cap \hat{S}_m^{2a}$ will escape D from the lower boundary of D and entering E, and the trajectory starting from any point in $F \cap \hat{S}_m^{2a}$ will escape F from the left boundary of F and entering E. Since E is a positive invariant set, and we have $\dot{x}_1 > 0$ and $\dot{x}_2 > 0$ in E, the trajectory starting from any point in E will go to \hat{P}_1^{2a} as $t \rightarrow +\infty$. Thus, the trajectory starting from any point in the positive invariant set \hat{S}_m^{2a} will go to \hat{P}_1^{2a} as $t \rightarrow +\infty$, implying $\hat{S}_m^{2a} \subset \mathcal{R}(\hat{P}_1^{2a})$, i.e., \hat{S}_m^{2a} is an inner estimation of attraction region (Zheng et al. (2018), Wang, She, and Ge (2020b)) for \hat{P}_1^{2a} .

Similarly, region $\hat{U}^{2a} = \hat{U}_1^{2a} \vee \hat{U}_2^{2a} \vee \hat{U}_3^{2a}$ (the light yellow region shown in Fig. 6(a)) is also a positive invariant set, where

$$\hat{U}_1^{2a} = \{(x_1, x_2) | (x_1 < 0 \wedge x_2 \geq \hat{b}_2^{2a}(x_1)) \vee (x_1 > 0 \wedge x_2 \geq \hat{r}_2^{2a}(x_1))\},$$

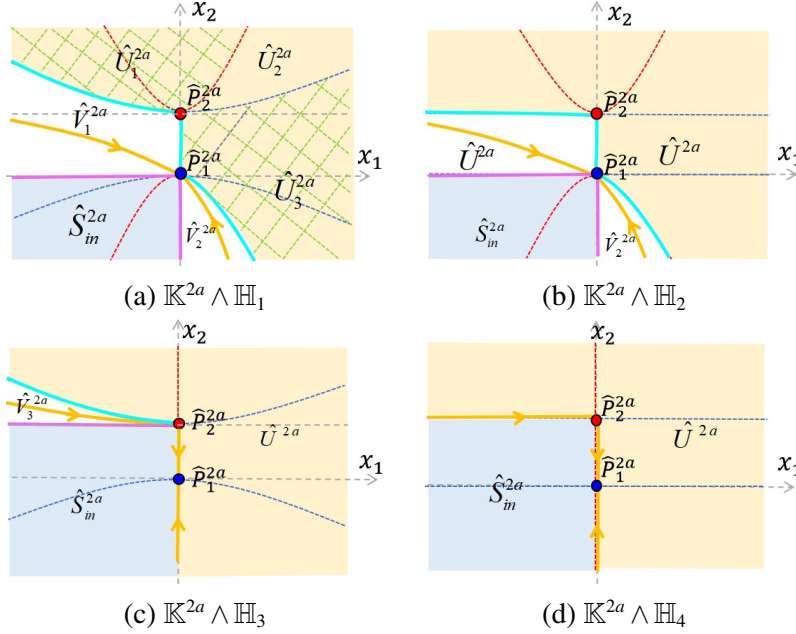


Figure 6 Certain separatrices of $\hat{P}_1^{2a}=(0,0)$ or $\hat{P}_2^{2a}=(0,M)$, and the inner and outer estimations of attraction regions for system (13). Red dotted curves $\dot{x}_1 = 0$; blue dotted curves: $\dot{x}_2 = 0$; yellow curves: separatrices, also serving as boundaries of attraction region; purple lines: boundary of the inner estimation of attraction region; bright blue lines: boundary of the outer estimation of attraction region. The green dashed grid is to distinguish \hat{U}_1^{2a} , \hat{U}_2^{2a} and \hat{U}_3^{2a} .

$$\hat{U}_2^{2a} = \{(x_1, x_2) | x_1 > 0 \wedge \hat{b}_2^{2a}(x_1) \leq x_2 \leq \hat{r}_2^{2a}(x_1)\},$$

$$\hat{U}_3^{2a} = \{(x_1, x_2) | x_1 \geq 0 \wedge \hat{r}_1^{2a}(x_1) \leq x_2 < \hat{b}_2^{2a}(x_1)\} / (0,0).$$

Note that \hat{U}_1^{2a} and \hat{U}_3^{2a} are also positive invariant sets. In addition, the trajectory starting from point in \hat{U}_2^{2a} will escape from the upper boundary of \hat{U}_2^{2a} and enter \hat{U}_1^{2a} moving far from \hat{P}_1^{2a} , or escape from the lower boundary of \hat{U}_2^{2a} and enter \hat{U}_3^{2a} moving far from \hat{P}_1^{2a} . Thus, we can obtain that $\mathcal{R}(\hat{P}_1^{2a}) \subset \hat{S}_{out}^{2a} = \mathbb{R}^2 \setminus \hat{U}^{2a}$, i.e., the region \hat{S}_{out}^{2a} is an outer estimation of attraction region for \hat{P}_1^{2a} . Further, we can obtain that $\hat{\Phi}^1(\hat{P}_1^{2a}) \in \hat{V}_1^{2a}$ and $\hat{\Phi}^2(\hat{P}_1^{2a}) \in \hat{V}_2^{2a}$, as the yellow lines shown in Fig. 6(a).

When Condition (\mathbb{H}_2) hold, we can obtain two stable separatrices $\hat{\Phi}^1(\hat{P}_1^{2a})$ and $\hat{\Phi}^2(\hat{P}_1^{2a})$ of \hat{P}_1^{2a} ; the inner estimation of attraction region \hat{S}_{in}^{2a} ; and outer estimation of attraction region \hat{S}_{out}^{2a} by similar analysis. Furthermore, we have $\hat{\Phi}^1(\hat{P}_1^{2a}) \in \hat{V}_1^{2a}$ and $\hat{\Phi}^2(\hat{P}_1^{2a}) \in \hat{V}_2^{2a}$, as shown in Figs. 6(b). When (\mathbb{H}_3) or (\mathbb{H}_4) hold, we can first simplify the system (13) by bringing in corresponding conditions. Then, by repeating the above analysis, we can obtain corresponding results, as shown in Figs. 6(c) and 6(d).

Consequently, for the system (13), the estimation of the attraction region for the saddle-node points \hat{P}_1^{2a} has been obtained. Further, letting $n_1(t) = x_1(t) + \frac{p_1}{2}$ and $n_2(t) = x_2(t) + \frac{p_2 - M}{2}$, the estimation of attraction region for P_1^{2a} can be obtained. Denoting $b_i^{2a}(n_1) = \hat{b}_i^{2a}(n_1 - \frac{p_1}{2}) + \frac{p_2 - M}{2}$ and $r_i^{2a}(n_1) = \hat{r}_i^{2a}(n_1 - \frac{p_1}{2}) + \frac{p_2 - M}{2}$, where $i = 1, 2$, we can obtain the theorem as below.

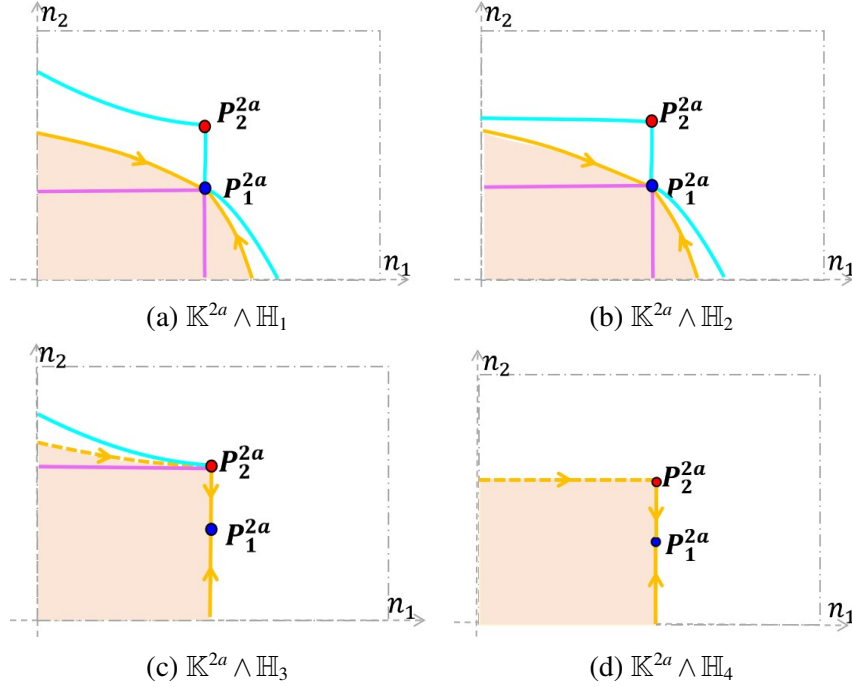


Figure 7 Attraction region of the P_1^{2a} for system (12) under Condition $\mathbb{K}^{2a} \wedge \mathbb{H}_i$ ($i = 1, 2, \dots, 4$). Red circle: undesired saddle-node equilibrium. Blue circle: desired saddle-node equilibrium. The yellow curves: the separatrices, also serving as boundaries of attraction region. Purple lines and bright blue lines denote the boundary of inner and outer estimations of attraction regions, respectively.

THEOREM 1. For the unstable saddle-node point P_1^{2a} , under Condition (\mathbb{H}) , we have $S_{in}^{2a} \subseteq S_A^{2a} = \mathcal{R}(P_1^{2a}) \subseteq S_{out}^{2a}$, where the attraction region S_A^{2a} , the inner estimation of attraction region S_{in}^{2a} and the outer estimation of attraction region S_{out}^{2a} are defined as follows:

(1) Under Conditions (\mathbb{H}_1) and (\mathbb{H}_2) , $S_A^{2a} = \{(n_1, n_2) | n_1 \leq g_2^{2a}(n_2), n_2 \leq g_1^{2a}(n_1)\}$, where $n_2 = g_1^{2a}(n_1)$ and $n_1 = g_2^{2a}(n_2)$ denotes the two stable separatrices $\Phi^1(P_1^{2a})$ and $\Phi^2(P_1^{2a})$ of P_1^{2a} , respectively;

$$S_{in}^{2a} = \{(n_1, n_2) | n_1 \leq \frac{p_1}{2}, n_2 \leq \frac{p_2 - M}{2}\}; S_{out}^{2a} = S_{out}^{2a,1} \vee S_{out}^{2a,2}, \text{ where}$$

$$S_{out}^{2a,1} = \{(n_1, n_2) | n_1 \leq \frac{p_1}{2}, n_2 < b_2^{2a}(n_1)\} \text{ and } S_{out}^{2a,2} = \{(n_1, n_2) | \frac{p_1}{2} \leq n_1 \leq p_1, n_2 < r_1^{2a}(n_1)\}.$$

(2) Under Condition (\mathbb{H}_3) , $S_A^{2a} = \{(n_1, n_2) | n_1 \leq \frac{p_1}{2}, n_2 < g_3^{2a}(n_1)\}$, where $n_2 = g_3^{2a}(n_1)$ denotes the stable separatrix $\Phi(P_2^{2a})$ of P_2^{2a} ; $S_{in}^{2a} = \{(n_1, n_2) | n_1 \leq \frac{p_1}{2}, n_2 < \frac{p_2 + M}{2}\}$; $S_{out}^{2a} = S_{out}^{2a,1}$;

(3) Under Condition (\mathbb{H}_4) , $S_{in}^{2a} = S_A^{2a} = S_{out}^{2a} = \{(n_1, n_2) | n_1 \leq \frac{p_1}{2}, n_2 < \frac{p_2 + M}{2}\}$.

Note that $n_i \geq 0$ ($i = 1, 2$) holds all the time.

The geometries of S_A^{2a} in Theorem 1 are illustrated as the pale pink region shown in Fig. 7.

Similarly, for system (1) under Condition (\mathbb{K}^{2b}) , we can obtain the inner (S_{in}^{2b}) and outer (S_{out}^{2b}) estimations of attraction regions for P_1^{2b} under four different conditions, as shown in Fig. 8.

For the four-equilibrium system, we also try to obtain the inner (S_{in}^4) and outer (S_{out}^4) estimations of attraction regions, and the detailed analysis can be found in App. A.3. Note that for the four-equilibrium

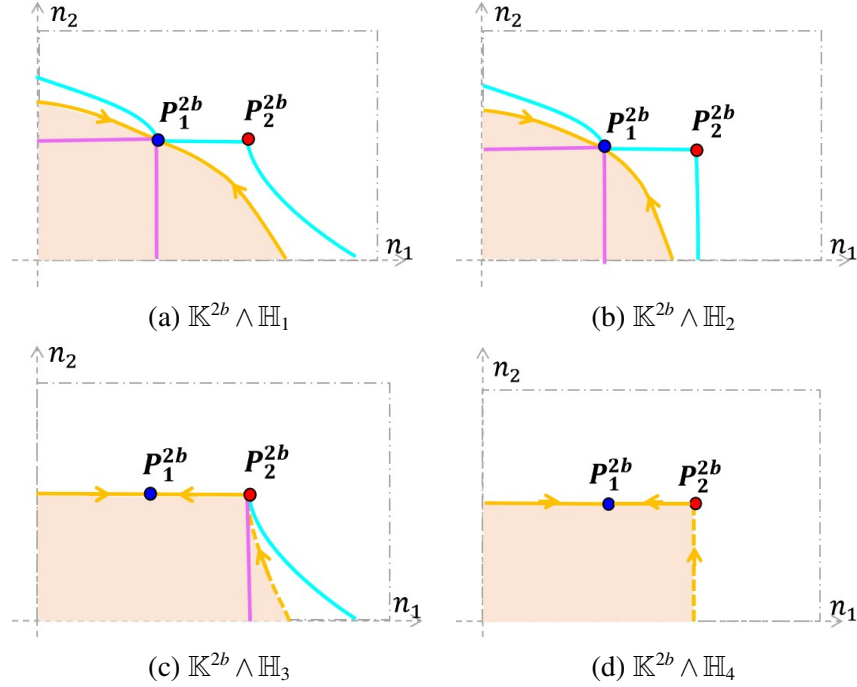


Figure 8 Attraction region of the P_1^{2b} for system (1) under Condition $\mathbb{K}^{2b} \wedge \mathbb{H}_i$ ($i = 1, 2, \dots, 4$). Red circle: undesired saddle-node equilibrium. Blue circle: desired saddle-node equilibrium. The yellow curves: the separatrices, also serving as boundaries of attraction region. Purple lines and bright blue lines denote the boundary of inner and outer estimations of attraction regions, respectively.

system, the attraction regions become more intricate due to the increased number of equilibria. In App. A.3, through a novel classification method, we obtained 20 distinct inner and outer estimations of attraction regions, which can be summarized as Theorems 2, 3, and 4 in App. A.3. The geometries of the attraction region for the four-equilibrium system are illustrated as the pale pink region shown in Fig. 9.

4. Ecological resilience control design

In the previous two sections, we obtain the inner (S_{in}) and outer (S_{out}) estimations of attraction regions with explicit algebraic expressions under each condition for a multi-equilibria MFD-represented traffic dynamic system (1). Note that for two-equilibria system, S_{in} corresponds to S_{in}^{2a} or S_{in}^{2b} , and S_{out} corresponds to S_{out}^{2a} or S_{out}^{2b} ; for two-equilibria system, S_{in} corresponds to S_{in}^4 and S_{out} corresponds to S_{out}^4 . While In this section, we will design two distinct resilience control schemes, aiming to facilitate the recoverability of the system to its respective steady states while minimally altering the original landscape, utilizing the obtained S_{in} and S_{out} . Sec. 4.1 illustrates the resilience control schemes utilizing S_{in} , denoted as RCS-1, and Sec. 4.2 provides the resilience control schemes utilizing S_{out} , denoted as RCS-2.

The trajectories starting from inside attraction region (or inner estimations of attraction regions) can converge to the original equilibrium, while for those that starting from outside attraction region (or outer estimations of attraction regions) will move away from the equilibrium. Our primary task is to control the trajectories that move away from the equilibrium point and guide them towards an alternative steady state. For

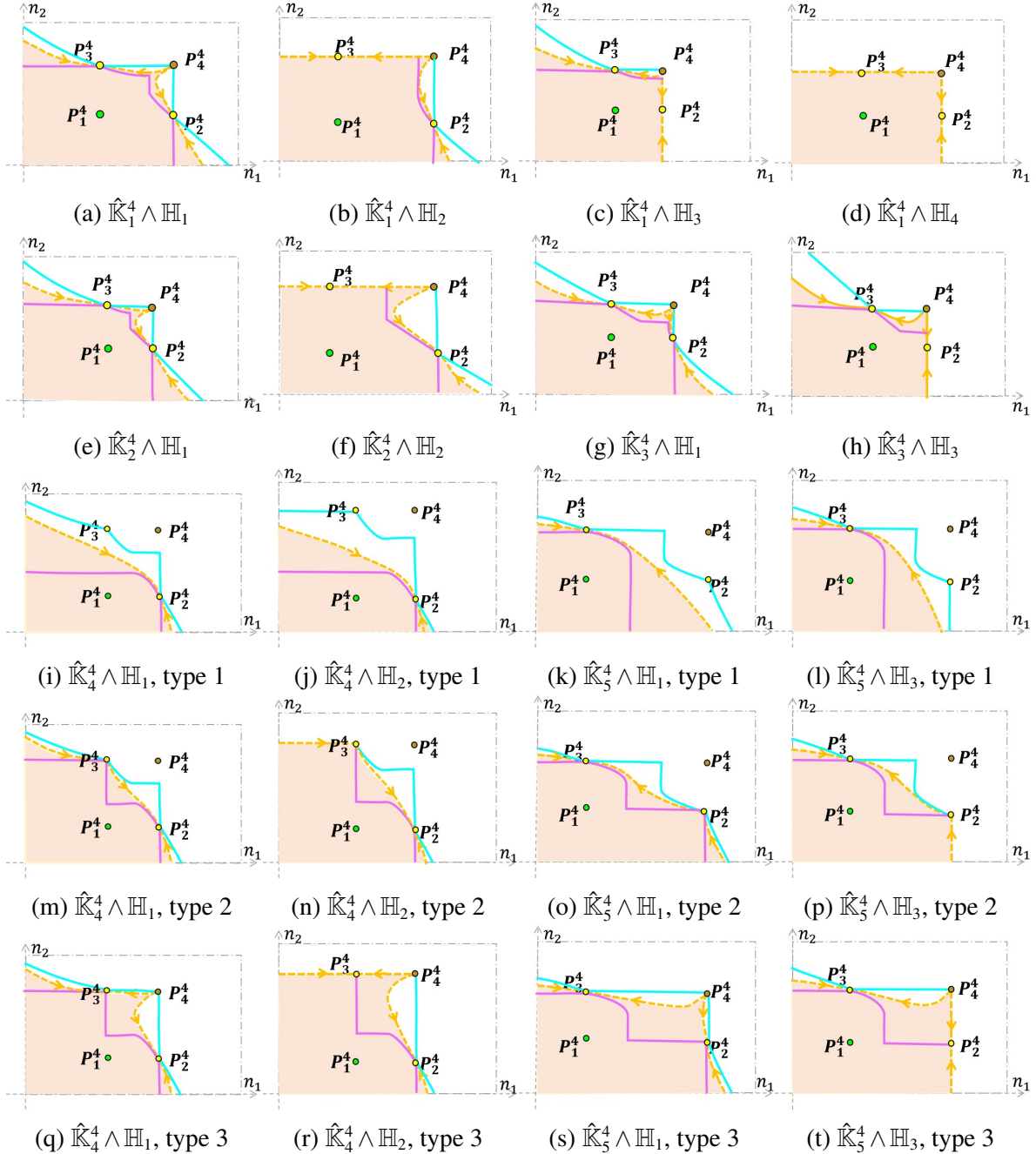


Figure 9 Attraction region of the P_1^4 of system (1) under Condition $\hat{\mathbb{K}}_s^4 \wedge \mathbb{H}_i$ ($s = 1, 2, \dots, 5$ and $i = 1, 2, \dots, 4$). Green circle: desired uncongested stable equilibrium. Yellow circle: saddle equilibrium. Yellow-brown circle: unstable equilibrium. Yellow curves with arrows: the separatrices, also serving as boundaries of attraction region. Purple lines and bright blue lines denote the boundary of inner and outer estimations of attraction regions, respectively.

multi-equilibria systems (1), we set up an alternative steady state $\mathbf{n}^1 = (n_{s1}, n_{s2})$ in $\mathbb{D} \setminus S_{in}$ or $\mathbb{D} \setminus S_{out}$, respectively. Then, the control schemes (RCS-1 and RCS-2) shall steer the trajectories to the ε -Neighborhood of \mathbf{n}^1 within the recovery time t_f . Note that the control does not necessarily bring the system to the equi-

librium state \mathbf{n}^0 , which allows the system to be adaptive (to a feasible steady state) and recoverable (to less congested state progressively).

Generally speaking, there are three main differences between the RCS-1 and RCS-2 schemes. With respect to control ‘‘intensity’’, RCS-1 is more aggressive than RCS-2. That is, the control region for RCS-1 is much larger than RCS-2, as control action $U_1(\mathbf{n})$ ($U_2(\mathbf{n})$) are imposed in $\mathbb{D} \setminus S_{in}$ ($\mathbb{D} \setminus S_{out}$) under RCS-1 (RCS-2) and we have $S_{in} \subset S_{out}$. With respect to control mechanism, RCS-1 has a universal control algorithm applied to all alternative steady states, while RCS-2 applies three forms of control, depending on the location of the alternative steady state. Here, we choose three control methods to prevent the emergence of new equilibrium points on the boundary of outer estimation of attraction regions. For instance, trajectories from the boundary of S_{out} tend to escape S_{out} , and one control scheme might lead to intersections between trajectories from $\mathbb{D} \setminus S_{out}$ and trajectories from S_{out} . This could potentially generate new equilibrium points on the boundary of the outer estimation of attraction regions, complicating theoretical derivations and causing control inefficiencies. With respect to control effect, the trajectories starting from $\mathbb{D} \setminus S_{out}$ will move towards \mathbf{n}^1 , while trajectories starting from $\mathbb{D} \setminus S_{in}$ will move towards \mathbf{n}^1 (Fig. 10(b)), or \mathbf{n}^0 (Fig. 10(c)).

4.1. Control formulation of RCS-1

The domain \mathbb{D} can be divided into two subregions: S_{in} and $\mathbb{D} \setminus S_{in}$, as shown in Fig. 10. If the starting points are in S_{in} , CPC u_1 and u_2 that satisfy Conditions \mathbb{K}^{2a} , \mathbb{K}^{2b} or \mathbb{K}^4 are conducted. According to Theorems 1, 2 and 4, trajectories from these starting points will move towards the \mathbf{n}^0 . Instead, if the initial states are in $\mathbb{D} \setminus S_{in}$, new control action $U^{in}(\mathbf{n})$ is activated for recovering trajectories starting from $\mathbb{D} \setminus S_{in}$ to the ε – *Neighborhood* of the target point within the recovery time t_f . The target point can be the uncongested equilibrium \mathbf{n}^0 or the alternative steady state \mathbf{n}^1 in $\mathbb{D} \setminus S_{in}$. Specifically, for system (1), if the starting states are in $\mathbb{D} \setminus S_{in}$, we apply the following control $U^{in}(n_1, n_2) = (U_1^{in}(n_1, n_2), U_2^{in}(n_1, n_2))$, defined by:

$$\begin{aligned} U_1^{in}(n_1, n_2) &= -\gamma_1(n_1 - ns_1) - u_2 G_2(n_2(t)) + G_1(n_1(t)) - d_1, \\ U_2^{in}(n_1, n_2) &= -\gamma_2(n_2 - ns_2) - u_1 G_1(n_1(t)) + G_2(n_2(t)) - d_2. \end{aligned} \quad (14)$$

where $\gamma_i = \frac{2G_{i,max}}{p_i}$. By adding proposed controller (14) to system (1), the trajectories starting from $\mathbb{D} \setminus S_{in}$ will move towards \mathbf{n}^1 directly (Fig. 10(b)), or intersect S_{in} (Fig. 10(c)). Once intersecting S_{in} , we rest the control, i.e., $U_1^{in} = U_2^{in} = 0$ immediately, as such that the trajectories will follow the initial system (1). According to Theorems 1, 2 and 4, trajectories from these starting points will move towards the \mathbf{n}^0 .

By doing so, we have developed a switched controlled system (She and Xue (2014), Skafidas et al. (1999), Gao et al. (2022), She et al. (2020)) as:

$$\dot{\mathbf{n}} = \mathbf{F}(\mathbf{n}) + U_1(\mathbf{n}),$$

where $U_1(\mathbf{n}) \equiv \mathbf{0}$ when $\mathbf{n} \in S_{in}$, $U_1(\mathbf{n}) = U^{in}(n_1, n_2)$ when $\mathbf{n} \in \mathbb{D} \setminus S_{in}$.

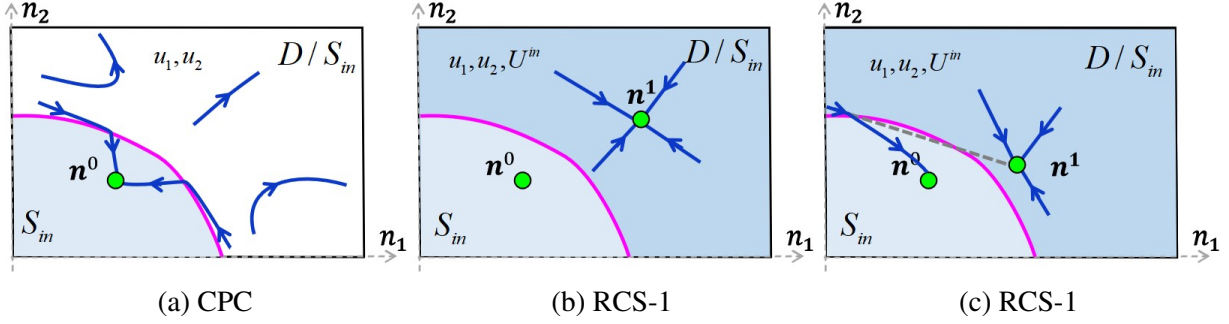


Figure 10 Schematic representation of phase portraits under CPC (a) and RCS-1 ((b) and (c)). Notice that in (c), the trajectories under RCS-1 intersect S_{in} . Once intersecting S_{in} , we rest the control $U^{in} = 0$ immediately, then trajectories spontaneously move towards the n^0 .

REMARK 1. For multi-equilibria systems (1), certain inner estimations of attraction regions do not contain its partial boundaries l_{ex} (e.g. Figs. 6(d), 8(d), 9(b) etc.). This is because the trajectories starting from the partial boundaries will deviate from the uncongested equilibrium point. In such cases, $U^{in}(\mathbf{n})$ are imposed until the trajectories intersect with \hat{l}_{ex} , where \hat{l}_{ex} is obtained by moving the line l_{ex} down (or left) by ε .

4.2. Control formulation of RCS-2

RCS-2 is designed based on S_{out} . Likewise, the domain \mathbb{D} can be divided into S_{out} and $\mathbb{D} \setminus S_{out}$, and $\mathbb{D} \setminus S_{out}$ can be further divided into R_1 , R_2 and R_3 , as illustrated in Fig. 11. If the starting states are in S_{out} , CPC u_1 and u_2 that satisfy Conditions \mathbb{K}^{2a} , \mathbb{K}^{2b} or \mathbb{K}^4 will be conducted. According to Theorems 1, 2 and 4, trajectories from these starting points will move towards n^0 or escape from the upper boundaries of S_{out} and enter $\mathbb{D} \setminus S_{out}$. Once the states enter in $\mathbb{D} \setminus S_{out}$, control action $U^{out}(\mathbf{n})$ will be activated for recovering trajectories to the ε -Neighborhood of n^1 in $\mathbb{D} \setminus S_{out}$ within the recovery time t_f .

Specifically, for a given system (1), there are three cases of control action $U^{out}(\mathbf{n})$, depending on the location of n^1 . First consider Case 1, where n^1 lies in R_1 , as depicted in Fig. 11(b). In this case, proposed RCS-2 is as follows: in addition to u_1 and u_2 , we will apply an additional control $U_1^{out}(n_1, n_2) = (U_{1,1}^{out}(n_1, n_2), U_{1,2}^{out}(n_1, n_2))$ in $R_1 \vee R_2$, and $U_2^{out}(n_1, n_2) = (U_{2,1}^{out}(n_1, n_2), U_{2,2}^{out}(n_1, n_2))$ in R_3 , where $U_1^{out}(n_1, n_2)$ are defined by:

$$\begin{aligned} U_{1,1}^{out}(n_1, n_2) &= -\gamma_1(n_1 - ns_1) - u_2 G_2(n_2(t)) + G_1(n_1(t)) - d_1, \\ U_{1,2}^{out}(n_1, n_2) &= -\gamma_2(n_2 - ns_2) - u_1 G_1(n_1(t)) + G_2(n_2(t)) - d_2, \end{aligned} \quad (15)$$

and $U_2^{out}(n_1, n_2)$ are defined by:

$$\begin{aligned} U_{2,1}^{out}(n_1, n_2) &= -u_2 G_2(n_2(t)) + G_1(n_1(t)) - d_1, \\ U_{2,2}^{out}(n_1, n_2) &= -\gamma_2 n_2 - u_1 G_1(n_1(t)) + G_2(n_2(t)) - d_2. \end{aligned} \quad (16)$$

by adding proposed controller (16) to system (1), the trajectories starting from R_3 will vertically escape from the upper boundary of R_3 and enter R_2 . Moreover, by adding proposed controller (15) to system (1),

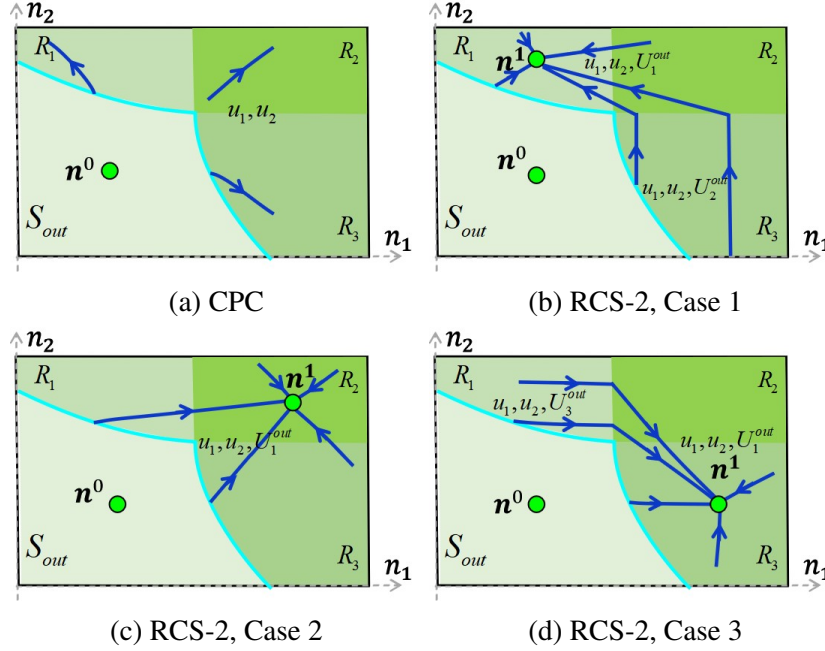


Figure 11 Schematic representation of phase portraits under CPC (a) and RCS-2 ((b), (c) and (d)). Note that there are three cases of control action, depending on the location of n^1 . Three cases of control action are chosen to prevent the emergence of new equilibrium points on the boundary of S_{out} .

the trajectories starting from $R_1 \vee R_2$ will move towards n^1 directly, as shown in Fig. 11(b). Thus, any trajectories entering $\mathbb{D} \setminus S_{out}$ will move towards n^1 under the controller.

Then consider Case 2, where n^1 lies in R_2 . In this case, $U_1^{out}(n_1, n_2) = (U_{1,1}^{out}(n_1, n_2), U_{1,2}^{out}(n_1, n_2))$ in $\mathbb{D} \setminus S_{out}$ will be applied. Subsequently, any trajectories going into $\mathbb{D} \setminus S_{out}$ will go to n^1 under our proposed controller, as shown in Fig. 11(c).

Finally consider Case 3, where n^1 lies in R_3 , as shown in Fig. 11(d). similarly, we will apply control action $U_1^{out}(n_1, n_2) = (U_{1,1}^{out}(n_1, n_2), U_{1,2}^{out}(n_1, n_2))$ in $R_3 \vee R_2$, and $U_3^{out}(n_1, n_2) = (U_{3,1}^{out}(n_1, n_2), U_{3,2}^{out}(n_1, n_2))$ in R_1 , where $U_3^{out}(n_1, n_2)$ are defined by:

$$\begin{aligned} U_{3,1}^{out}(n_1, n_2) &= -\gamma_1 n_1 - u_2 G_2(n_2(t)) + G_1(n_1(t)) - d_1, \\ U_{3,2}^{out}(n_1, n_2) &= -u_1 G_1(n_1(t)) + G_2(n_2(t)) - d_2. \end{aligned} \quad (17)$$

by adding proposed controller (17) to system (1), the trajectories starting from R_1 will horizontally escape from the right boundary of R_1 and enter R_2 . Moreover, by adding proposed controller (15) to system (1), the trajectories starting from $R_2 \vee R_3$ will move towards n^1 directly, as shown in Fig. 11(d). Thus, any trajectories entering $\mathbb{D} \setminus S_{out}$ will move towards n^1 under our proposed controller.

By doing so, we have developed another switched controlled system (She and Xue (2014), Skafidas et al. (1999), Gao et al. (2022), She et al. (2020)) as:

$$\dot{n} = F(n) + U_2(n),$$

where $U_2(\mathbf{n}) \equiv \mathbf{0}$ when $\mathbf{n} \in S_{out}$, and $U_2(\mathbf{n})$ features different formulation in different cases when $\mathbf{n} \in \mathbb{D} \setminus S_{out}$. Specifically,

- in case 1, $U_2(\mathbf{n}) = U_1^{out}(n_1, n_2)$ when $\mathbf{n} \in R_1 \vee R_2$ and $U_2(\mathbf{n}) = U_2^{out}(n_1, n_2)$ when $\mathbf{n} \in R_3$;
- in case 2, $U_2(\mathbf{n}) = U_1^{out}(n_1, n_2)$ when $\mathbf{n} \in \mathbb{D} \setminus S_{out}$;
- in case 3, $U_2(\mathbf{n}) = U_1^{out}(n_1, n_2)$ when $\mathbf{n} \in R_2 \vee R_3$ and $U_2(\mathbf{n}) = U_3^{out}(n_1, n_2)$ when $\mathbf{n} \in R_1$.

REMARK 2. $U^{in}(n_1, n_2)$ and $U_2^{out}(n_1, n_2)$ would have the same formulation if the alternative steady state \mathbf{n}^1 in both controllers are same. This implies that there may exist initial states, such that the system may end up with identical recovery trajectories under RCS- 1 and RCS-2, respectively.

Furthermore, for a given system (1), if a stable equilibrium point exists (i.e., Condition (\mathbb{K}^4) holds), a local Lyapunov function can be found (Wang et al. (2021), Willems (1971), Blanchini (1995)) for the new controlled system with RCS-2. Specifically, denoting $\mathbf{n} = (n_1, n_2)^T$, we can prove that the function $V = (\mathbf{n} - \mathbf{n}^0)^T \mathbf{B} (\mathbf{n} - \mathbf{n}^0) (\mathbf{n} - \mathbf{n}^1)^T (\mathbf{n} - \mathbf{n}^1)$ is a local Lyapunov function for system (1) with RCS-2, where $\mathbf{B} = (\mathbf{P}^{-1})^T \mathbf{P}^{-1}$ and

$$\mathbf{P} = \begin{pmatrix} p_{11} & p_{12} \\ p_{21} & p_{22} \end{pmatrix} = \begin{pmatrix} \frac{-a_1 s_1 + a_2 s_2 + Q}{2a_1 s_1 u_1} & \frac{-a_1 s_1 + a_2 s_2 - Q}{2a_1 s_1 u_1} \\ 1 & 1 \end{pmatrix}$$

with $Q = \sqrt{a_1^2 s_1^2 + a_2^2 s_2^2 - 2a_1 a_2 s_1 s_2 + 4a_1 a_2 s_1 s_2 u_1 u_2}$; $s_1 = \frac{1}{2} \sqrt{p_1^2 - \frac{4d_1 + 4u_2 d_2}{a_1(1-u_1 u_2)}}$; $s_2 = \frac{1}{2} \sqrt{p_2^2 - \frac{4d_2 + 4u_1 d_1}{a_2(1-u_1 u_2)}}$. Obviously, $V > 0$ holds for all $\mathbf{n} \in \mathbb{D}$ except for $\mathbf{n} = \mathbf{n}^0$ and $\mathbf{n} = \mathbf{n}^1$. Moreover, $V = 0$ holds if and only if $\mathbf{n} = \mathbf{n}^0$ and $\mathbf{n} = \mathbf{n}^1$. In addition, in the neighborhood of \mathbf{n}^0 , we have $\frac{dV(t)}{dt} < 0$ holds, and detailed proofs are as follows:

Letting $\mathbf{n} - \mathbf{n}^0 = \mathbf{P}\mathbf{y}$, where $\mathbf{y} = (y_1, y_2)^T$, we can transform the system (1) into:

$$\begin{aligned} \frac{dy_1(t)}{dt} &= \lambda_1 y_1(t) + H_1(y_1(t), y_2(t)), \\ \frac{dy_2(t)}{dt} &= \lambda_2 y_2(t) + H_2(y_1(t), y_2(t)), \end{aligned} \tag{18}$$

where $\lambda_1 = -a_1 s_1 - a_2 s_2 + Q < 0$; $\lambda_2 = -a_1 s_1 - a_2 s_2 - Q < 0$; $H_1(y_1(t), y_2(t))$ and $H_2(y_1(t), y_2(t))$ represent second-order remained terms.

By the above coordinate transformation, denoting $\delta = \mathbf{n}^1 - \mathbf{n}^0 = (\delta_1, \delta_2)^T$, we can obtain that:

$$\begin{aligned} V(t) &= (\mathbf{n} - \mathbf{n}^0)^T \mathbf{B} (\mathbf{n} - \mathbf{n}^0) (\mathbf{n} - \mathbf{n}^1)^T (\mathbf{n} - \mathbf{n}^1), \\ &= (\mathbf{P}\mathbf{y})^T \mathbf{B} (\mathbf{P}\mathbf{y}) (\mathbf{P}\mathbf{y} - \delta)^T (\mathbf{P}\mathbf{y} - \delta), \\ &= \mathbf{y}^T \mathbf{y} (\mathbf{P}\mathbf{y} - \delta)^T (\mathbf{P}\mathbf{y} - \delta), \\ &= V_1 \cdot V_2 \end{aligned} \tag{19}$$

where $V_1 = y_1^2 + y_2^2$ and $V_2 = (p_{11}y_1 + p_{12}y_2 - \delta_1)^2 + (p_{21}y_1 + p_{22}y_2 - \delta_2)^2$. Then we have:

$$\begin{aligned} \frac{dV(t)}{dt} &= \frac{\partial V}{\partial y_1} \cdot \frac{dy_1(t)}{dt} + \frac{\partial V}{\partial y_2} \cdot \frac{dy_2(t)}{dt}, \\ &= 2(\delta_1^2 + \delta_2^2)(\lambda_1 y_1(t)^2 + \lambda_2 y_2(t)^2) + H_v^1(y_1(t), y_2(t)). \end{aligned} \tag{20}$$

where $H_v^1(y_1(t), y_2(t))$ represents the high-order remained terms, and the lowest power of it is cubic. Obviously, $\frac{dV(t)}{dt} < 0$ holds for arbitrary (y_1, y_2) in the neighborhood of $(0, 0)$ except $(0, 0)$, as we have $\lambda_2 < \lambda_1 < 0$. That is, $\frac{dV(t)}{dt} < 0$ holds for arbitrary (n_1, n_2) in the neighborhood of \mathbf{n}^0 , implying function V serves as a local Lyapunov function for the system in the neighbor of \mathbf{n}^0 .

Similarly, we can prove that $\frac{dV(t)}{dt} < 0$ holds in the neighborhood of \mathbf{n}^0 . Specifically, letting $z_1 = n_1 - ns_1$ and $z_2 = n_2 - ns_2$, we have

$$\frac{dV(t)}{dt} = -2(\delta_1 \delta_2)B(\delta_1 \delta_2)^T(z_1(t)^2 + z_2(t)^2) + H_v^2(z_1(t), z_2(t)). \quad (21)$$

where $H_v^2(z_1(t), z_2(t))$ represents the high-order remained terms, and the lowest power of it is cubic. Obviously, $\frac{dV(t)}{dt} < 0$ holds for arbitrary (z_1, z_2) in the neighborhood of $(0, 0)$ except $(0, 0)$, as B is a symmetric positive definite matrix. In other words, $\frac{dV(t)}{dt} < 0$ holds for arbitrary (n_1, n_2) in the neighborhood of \mathbf{n}^1 , implying function V is also local Lyapunov function for system in the neighbor of \mathbf{n}^1 .

5. Case studies

In this section, the control performance of the proposed resilient control by comparative case studies are demonstrated. In particular, we benchmark with the classical perimeter control (CPC) and the traffic-resilience oriented control proposed in [Gao et al. \(2022\)](#).

5.1. Numerical verification

A two-region system is set up for case studies, where the network and traffic settings follow the Downtown San Francisco road network from Aboudolas and Geroliminis' work ([Aboudolas and Geroliminis \(2013\)](#)). We adopt the function form of the MFD models from [Gao et al. \(2022\)](#) for comparison purposes, i.e., $G_1(n_1) = -\frac{28}{289}n_1(n_1 - 850)$ for region 1 and $G_2(n_2) = -\frac{32}{961}n_2(n_2 - 1550)$ for region 2, with maximum capacity $G_{1,max} = 7 \times 10^4$, $G_{2,max} = 8 \times 10^4$ [veh/h] and jam accumulations $p_1 = 1700$, $p_2 = 3100$ [veh].

Based on this MFD data, we consider traffic flow dynamics following Eq. (1) and (2) as defined in Sec. 2.1. We first validate the theoretical results of inner and outer estimation of attraction regions for both two and four equilibria derived in Sec. 3 (refer to Theorems 1, 2 and 4, Figs. 7, 8 and 9), accumulating to a total of 28 distinct phase portraits (8 for two-equilibria system and 20 for four-equilibria system). To achieve this, we consider 28 different scenarios, labeled as Scenario 1 to Scenario 28. Each scenario has distinct allowed flow rates u_i and net fixed demand d_i ($i = 1, 2$), corresponding to the 28 conditions in Sec. 3. For example, Scenario 1 corresponds to Condition $\mathbb{K}^{2a} \wedge \mathbb{H}_1$. We showcase two scenarios (scenario 1 and scenario 9) in Fig. 12. Fig. 12(a) depicts the phase portrait for Scenario 1: $u_1 = 0.4, u_2 = 0.5128, d_1 = 3 \times 10^4, d_2 = 5 \times 10^4$ [veh/h], satisfying Condition $\mathbb{K}^{2a} \wedge \mathbb{H}_1$, corresponding to the two-equilibrium case. It verifies Theorem 1 (or Fig. 7(a)). Fig. 12(b) presents the phase portrait for Scenario 9: $u_1 = 0.3, u_2 = 0.4, d_1 = 3 \times 10^4, d_2 = 5 \times 10^4$ [veh/h], satisfying Condition $\mathbb{K}_1^4 \wedge \mathbb{H}_1$, corresponding to the four-equilibrium case. It verifies Theorem 2 (or

Fig. 9(a)). Parameters and numerical results for other scenarios can be found in App. B: Fig. 22, Fig. 23 and Table 4. The results are also consistent with our theoretical findings.

Next, numerical phase portraits of the controlled systems under RCS-1 and RCS-2 are demonstrated, as depicted in Fig. 13(b), 13(c), and 13(e), 13(f). Here we use Scenario 9 as a showcase, which corresponds to the complex four-equilibria case. For the simpler two-equilibria case, the control scheme can also be applicable. Note that Case i ($i = 1, 2, 3$) denotes the case where the alternative steady state $\mathbf{n}^1 \in R_i$. The illustration of R_i can be found in Fig. 11. Here, we take Case 1 ($\mathbf{n}^1 \in R_1$) and Case 3 ($\mathbf{n}^1 \in R_3$) as examples. Fig. 13(a) represents the results under CPC control, serving as a benchmark control. Let us focus on the part $\mathbb{D} \setminus S_{in}$ in Fig. 13(a), (b), and (e). In Fig. 13(a), a small portion of the trajectories in $\mathbb{D} \setminus S_{in}$ enters S_{in} , while a larger portion of the trajectories moves towards the upper or right boundaries of the phase portrait, approaching grid-lock, i.e., high traffic density but low outflow. In contrast, Fig. 13(b) and 13(e) demonstrate that RCS-1 is capable of guiding trajectories starting from $\mathbb{D} \setminus S_{in}$ towards either the non-congested equilibrium point \mathbf{n}^0 or the alternative steady state \mathbf{n}^1 in $\mathbb{D} \setminus S_{in}$, avoiding grid-lock. Similarly, in Fig. 13(a), trajectories in $\mathbb{D} \setminus S_{out}$ all move towards the upper and right boundaries of the phase portrait, while Fig. 13(c) and 13(f) confirm that RCS-2 directs trajectories in $\mathbb{D} \setminus S_{out}$ towards the alternative steady state \mathbf{n}^1 in $\mathbb{D} \setminus S_{out}$. These results demonstrate the recoverability under RCS-1 and RCS-2. Furthermore, the similar trajectories in $R1 \vee R2$ (upper region in $\mathbb{D} \setminus S_{out}$) in Fig. 13(b) and 13(c) confirm that there exist some initial states such that the recovery trajectories starting from them under RCS-1 and RCS-2 are identical, as illustrated in Remark 2. This is because, in $R1 \vee R2$, RCS-1 and RCS-2 have the same control formulation.

Moreover, for the case where the system has a stable equilibrium (we here use scenario 9 as a showcase), we can find the function $V(t)$ defined in Sec. 4.2, as shown in Fig. 14(a), is a local Lyapunov function for the controlled system with RCS-2. Moreover, the projection of $V(t)$ in the plane $n_1 - n_2$ is shown in the Fig. 14(b). Note that the local Lyapunov is only applicable to four-equilibria system, and is not suitable for two-equilibria system, as there exist no stable equilibria in two-equilibria system.

5.2. Comparison on proposed two control schemes with CPC and RCS-single

In this section, we compare our proposed control schemes (RCS-1 and RCS-2) with two classical perimeter control strategies (RCS-single in Gao et al. (2022) and CPC in Haddad and Geroliminis (2012)) to show the resilience of our approaches. We maintain the same MFD setup as in the previous section, and use scenario 9 as an example. Fig. 13(d) depicts the numerical simulation of phase portrait for the control system with RCS-single, where trajectories within the whole region recover to the original equilibrium \mathbf{n}^0 . The key distinction between RCS-single and proposed schemes lies in the trajectories within the part: our proposed control schemes can recover to the alternative steady state \mathbf{n}^1 , while RCS-single can only recover to the original equilibrium \mathbf{n}^0 .

Then, we calculate the resilience measure (defined in Eq. (10)) under different control schemes. Resilience measures are situation-dependent, where situations referring to states (vehicle accumulations)

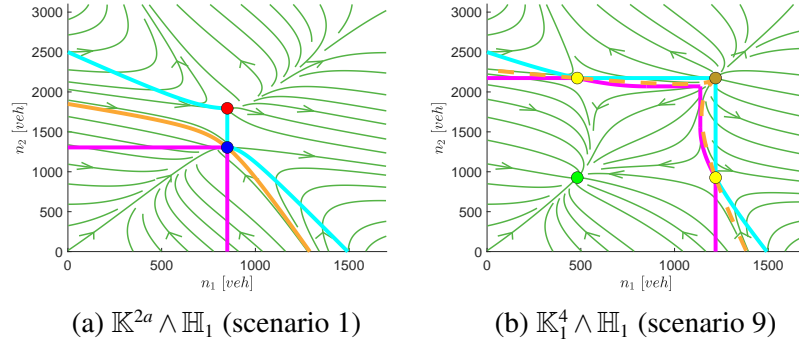


Figure 12 Numerical simulation phase portraits for system (1) under Conditions (a) $\mathbb{K}^{2a} \wedge \mathbb{H}_1$ (scenario 1) and (b) $\mathbb{K}_1^4 \wedge \mathbb{H}_2$ (scenario 9). Red circle: undesired saddle-node equilibrium. Blue circle: desired uncongested saddle-node equilibrium. Green circle: desired uncongested stable equilibrium. Yellow circle: saddle equilibrium. Yellow-brown circle: unstable equilibrium. Green line with arrows: the trajectories. Purple line and light blue line represent the inner and outer estimations of attraction regions, respectively. The yellow lines represent the numerical attraction region boundaries, solid yellow lines indicating the boundary line belongs to attraction region, while dashed yellow lines indicating the boundary line does not belong to attraction region. The agreement of this figure with Figs. 7(a) and Fig. 9(a) validate the theoretical analysis.

after disturbances, also known as initial recovery states. For instance, we assume state perturbations suddenly occur at moment $t = 0.5$ [h]. Situation i denotes the disturbed state at $t = 0.5$ [h] as A_i ($i = 1, 2, 3$). Here, we consider three situations, i.e., $A_1 = (500, 2800)$, $A_2 = (1500, 2800)$ and $A_3 = (1428, 1395)$, marked as three pentagrams in Fig. 13. Following these trajectories (the black lines in Fig. 13) departing from the pentagrams, we plot the vehicle accumulation $n_1(t)$, completion flow rate $G_1(n_1(t))$, and the numerical diagrams of deviation from maximum completion flow ($G_{1,max}$ and $G_{2,max}$) evolving with time under each control scheme (CPC, RCS-1, RCS-2, RCS-single) in Fig. 15. Here we use Case 1 (corresponding to Fig. 13(b) and 13(c)) as an example to illustrate performance the proposed control schemes, and the results for Case 2 and Case 3 can be found in App. B, Fig. 24 and Fig. 25.

Clearly, as depicted in Fig. 15(g), (h), and (i), traffic system collapses rapidly under CPC (blue solid line) (within 0.006 [h] for A_1 , 0.01 [h] for A_2 and 0.007 [h] for A_3); under RCS-single (red solid line), system initially rises slowly approaching maximum completion flow, then rebounds and stabilizes at a deviation of 26140 [veh/h] (within 0.70 [h] for A_1 , 1.61 [h] time for A_2 and 1.04 [h] for A_3); under the proposed RCS-1 (yellow solid line), the system swiftly recovers to a deviation of 17441 [veh/h] (within 0.16 [h] for A_1 and 0.16 [h] for A_2 , coinciding with the green solid line), or it first rises rapidly approaching the maximum completion flow, then rebounds and stabilizes at a deviation of 26140 [veh/h] (within 0.21 [h] for A_3); under the proposed RCS-2 (green solid line), the system swiftly recovers to a deviation of 17441 [veh/h] (within 0.16 [h] for A_1 and 0.16 [h] for A_2), or it resists the continued deterioration of the system, guiding a swift recovery, and stabilizes at a deviation of 17441 [veh/h] (within 0.19 [h] for A_3). Here, we take A_1 as an example to

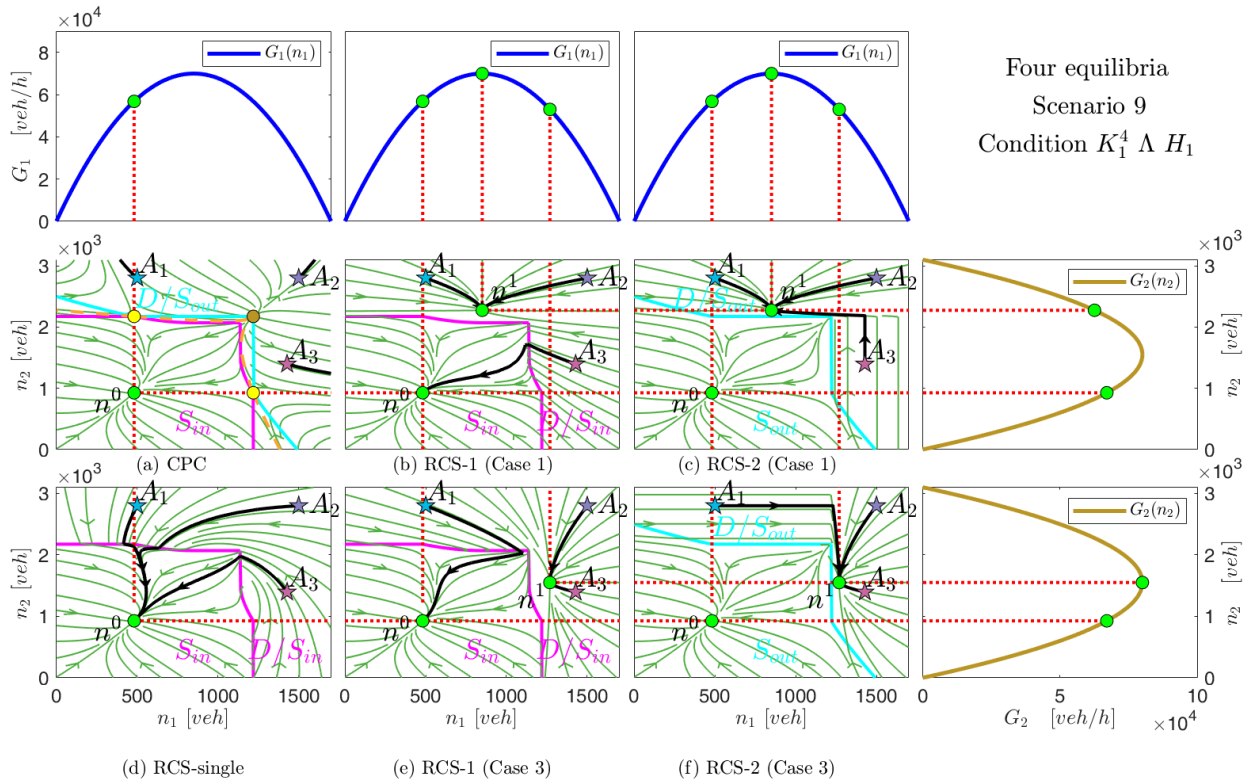


Figure 13 Numerical simulation phase portraits of system (1) with (a) CPC, (b) RCS-1 (case 1), (c) RCS-2 (case 1), (d) RCS-single, (e) RCS-1 (case 3) and (f) RCS-2 (case 3) under condition $\mathbb{K}_1^4 \wedge \mathbb{H}_1$ (scenario 9). Green circle: uncongested equilibrium n^0 and alternative steady state n^1 . Pentagrams denote three situations (i.e., three initial recovery states), black lines departing from the pentagrams are the corresponding recovery trajectories. CPC cannot recover the system; RCS-single recovers to the original equilibrium $n^0 = (481, 926)$, while RCS-1 and RCS-2 can recover to alternative stable states n^1 . Here we choose $n^1 = (850, 2274)$ for Case 1 and $n^1 = (1269, 1550)$ for Case 3, both satisfying the selectable range of alternative stable states Eq. 7. Note that Case $i (i = 1, 2, 3)$ denotes the case where the alternative steady state $n^1 \in R_i$. The illustration of R_i can be found in Fig. 11.

elucidate the reasons for the aforementioned phenomena. Under CPC, the vehicle accumulation $n_2(t)$ (Fig. 15(d), blue dotted line) develops from 2800 to a jam vehicle accumulation of 3100 [veh] within 0.006 [h], leading to the completion flow $G_2(n_2(t))$ (blue solid line) tending towards 0. This causes Region 2 to enter a gridlock state from which it cannot recover. Under RCS-single, the vehicle accumulation $n_1(t)$ (Fig. 15(a), red dotted line) initially decreases slowly from 500 [veh], then slowly increases before decreasing again, finally stabilizing at the original equilibrium of 481 [veh]. Correspondingly, the completion flow decreases slowly, then increases slowly, before decreasing again and stabilizing at 56818 [veh/h]. Simultaneously, the vehicle accumulation $n_2(t)$ (Fig. 15(d), red dotted line) decreases slowly at first, then rapidly decreases and stabilizes at 926 [veh]. Consequently, the completion flow $G_2(n_2(t))$ (Fig. 15(d), red solid line) first rises

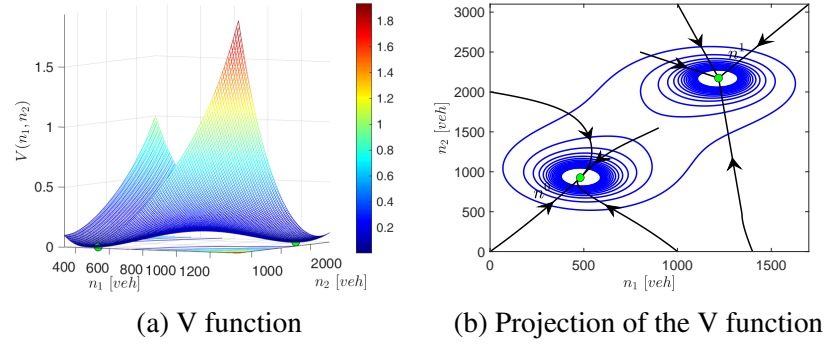


Figure 14 (a) V function with respect to n_1 and n_2 . (b) Projection of the V function on the $n_1 - n_2$ plane. The black line with arrows represents several trajectories of system with RCS-2. Green circle: the equilibrium points of system with RCS-2 (case 2). Note that scenario 9 is considered. Here, $n^0 = (481, 926)$ and $n^1 = (1219, 2174)$.

slowly to maximum completion flow, then rapidly decreases and stabilizes at 67045 [veh/h]. Therefore, the recoverability of RCS-single is guaranteed, but with a longer duration. Under the proposed RCS-1 and RCS-2, due to high travel demand, the vehicle accumulation $n_1(t)$ (Fig. 15(a), green dotted line) rapidly increases from 500 [veh] and stabilizes at 850 , resulting in the completion flow (Fig. 15(a), green solid line) rapidly rising and stabilizing at the maximum completion flow of 7×10^4 [veh/h]. Simultaneously, the vehicle accumulation $n_2(t)$ (Fig. 15(b), green dotted line) rapidly decreases from 2800 to 2274 [veh], leading the completion flow $G_2(n_2(t))$ quickly stabilized at 62559 [veh/h]. Consequently, RCS-1 and RCS-2 can ensure rapid recoverability, outperforming RCS-single. It is noteworthy that in this scenario, RCS-1 and RCS-2 exhibit identical recovery trajectories. We also provide the cases of RCS-1 and RCS-2 employing different recovery trajectories, as shown in Fig. 15(c), (f), and (i).

For a more accurate comparison, based on Fig. 15 and Eq. (10), we integrate the curve of $-D_s$ versus t to obtain the value of resilience measure, R under RCS-1, RCS-2, and RCS-single. The results are outlined in Table 2. Noteworthy, the absolute value of R corresponds to the area of the resilience triangle during the recovery period, and it signifies the loss of actual completed trips compared to the maximum number of trips that could have been completed during the recovery period. A larger resilience measure R corresponds to a smaller area of the resilience triangle (less loss), indicating greater resilience. As presented in Table 2, for all three Situations (A_1 , A_2 and A_3), resilience measures for RCS-1 and RCS-2 are significantly larger than RCS-single, demonstrating exceptional recovery capabilities.

6. Conclusion

In this paper, we define the ecological resilience of urban traffic, and further propose a resilience control methodology from the perspective of ecological resilience. Specifically, the ecological resilience of urban traffics is defined by the ability for a traffic system to resist uncertain perturbations by shifting to alternative states. The resilience control methodology comprises three aspects: portraying the recoverable scopes,

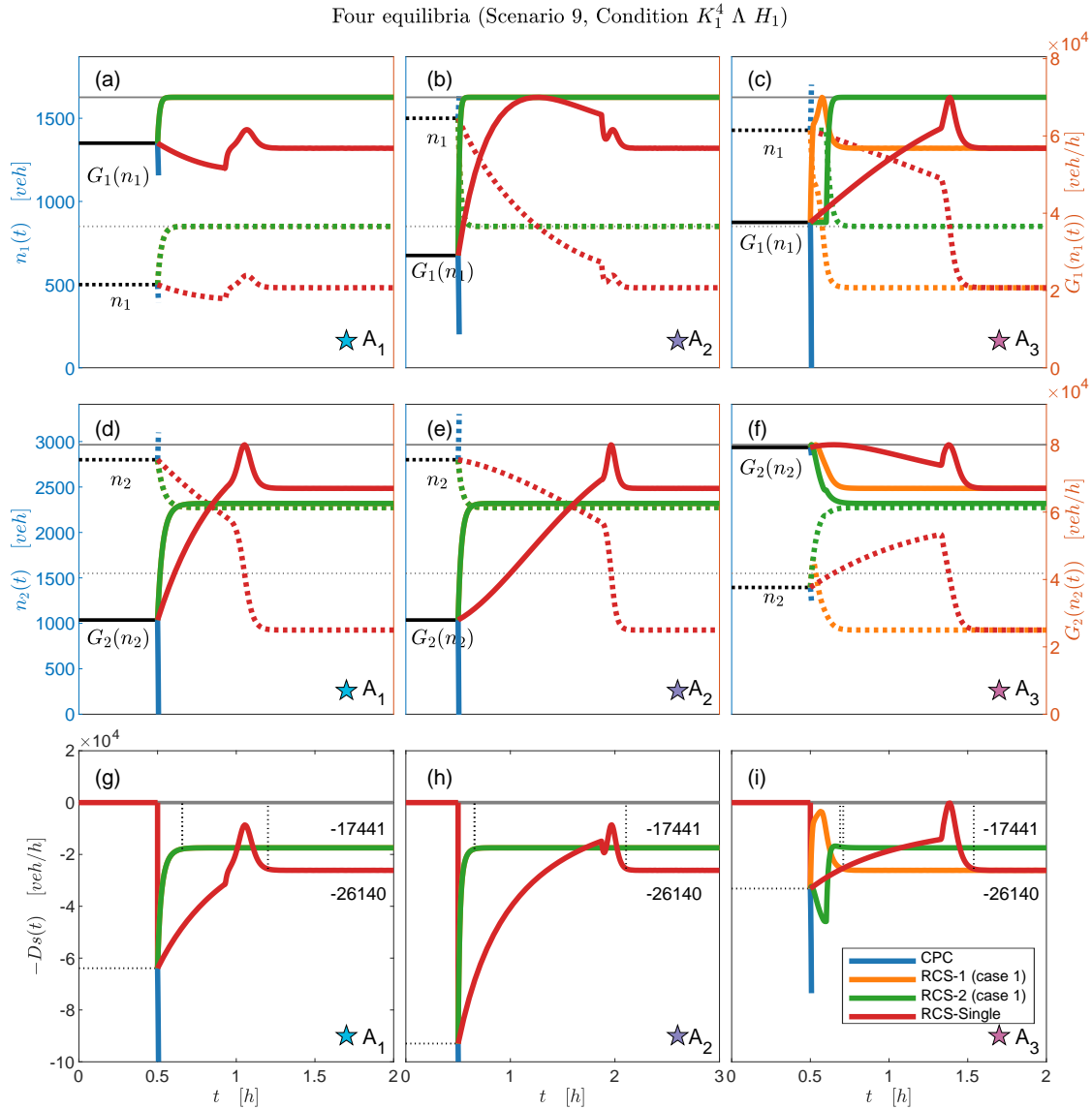


Figure 15 Vehicle accumulations (dotted line) and completion flow rates (solid line) of Region 1 ((a), (b) and (c)) and Region 2 ((d), (e) and (f)). The numerical diagrams of deviation from maximum complete flow $-D_s$ ((g), (h) and (i)) evolving with time t under CPC, RCS-1, RCS-2 and RCS-single. Scenario 9 is considered. Note that for (a)-(f), we employ dual y-axes. The left y-axis represents vehicle accumulation (density), while the right y-axis represents completion flow. A_i ($i = 1, 2, 3$) are the same as the three pentagrams in Fig. 13. The results in (a)(d)(g) ((b)(e)(h) and (c)(f)(i)) are obtained by following the recovery trajectories (black lines in Fig. 13) departing from the pentagram A_1 (A_2 and A_3). Reaffirming that RCS-single, RCS-1, and RCS-2 can ensure recoverability, while CPC can not. The resilience triangles in (g), (h) and (i) reveal that RCS-1 and RCS-2 outperform RCS-single, as RCS-1 and RCS-2 have smaller resilience triangles (loss) in most scenarios.

Table 2 Resilience measure [veh].

| resilience control | A_1 | | | A_2 | | | A_3 | | |
|--------------------|--------|--------|--------|--------|--------|--------|--------|--------|--------|
| | Case 1 | Case 2 | Case 3 | Case 1 | Case 2 | Case 3 | Case 1 | Case 2 | Case 3 |
| RCS-1 | -4031 | -4384 | -3110 | -4284 | -5646 | -3681 | -4250 | -3302 | -1710 |
| RCS-2 | -4031 | -4384 | -5800 | -4284 | -6558 | -6615 | -3776 | -3302 | -1744 |
| RCS-single | -24568 | -56501 | -20584 | -24568 | -56501 | -20584 | -24568 | -56501 | -20584 |

Case i ($i = 1, 2, 3$) denotes the case where the alternative steady state $\mathbf{n}^1 \in R_i$, as shown in Fig. 11. A_i denotes three situations, corresponding to three pentagrams in Fig. 13 and Fig. 15.

designing alternative steady states, controlling system to shift to alternative steady states for adapting large disturbances. Among them, the recoverable scopes are portrayed by inner and outer estimations of attraction regions; the alternative steady states are set close to the optimal state and outside the recoverable scopes of the original equilibrium; the controller ensures the local stability of the alternative steady states, without changing the trajectories inside the recoverable scopes of the original equilibrium as much as possible. We implemented the proposed control framework in a two-region traffic network described by parabolic MFD dynamic, and designed proposed control schemes (RCS-1 and RCS-2). Comparisons with the classical urban traffic resilience control schemes (CPC and RCS-single, etc.) show that, proposed resilience control schemes (RCS-1 and RCS-2) has a better adaptability and generates a greater resilience measure. Noteworthy, RCS-1 differs with RCS-2 in control intensity, control formulation and control effect. Note that, for multi-region (more than two-region) MFD dynamics, our resilience control idea can still be applied. The difficulty in implementing the resilience control idea is that for N-dimensional system, the equilibrium point will be more complex, and the attraction region maybe more difficult to obtain. Moreover, the inner estimation of attraction region we can obtain may shrink and the outer estimation of attraction region may expand, potentially affecting the effectiveness of the regulation scheme.

There is still work to be done in the future. Given this paper considers mainly constant MFD dynamics, and it is worth to extend the methodology of this paper to more general time-varying MFD dynamics in the future. Moreover, a feasible resilience control is provided in this paper, and future work will be extended to find an optimal resilience control scheme.

Acknowledgments

This work was supported by the National Key R&D Program of China (No.2022YFA1005103), the National Natural Science Foundation of China (12371452, 72225012, 72288101, 71822101, 12101030) and the Fundamental Research Funds for the Central Universities.

References

Aboudolas K, Geroliminis N, 2013 *Perimeter and boundary flow control in multi-reservoir heterogeneous networks. Transportation Research Part B: Methodological* 55:265–281.

-
- Aghamohammadi R, Laval JA, 2020 *Dynamic traffic assignment using the macroscopic fundamental diagram: A review of vehicular and pedestrian flow models. Transportation Research Part B: Methodological* 137:99–118.
- Ampountolas K, Zheng N, Geroliminis N, 2017 *Macroscopic modelling and robust control of bi-modal multi-region urban road networks. Transportation Research Part B: Methodological* 104:616–637.
- Blanchini F, 1995 *Nonquadratic lyapunov functions for robust control. Automatica* 31(3):451–461.
- Bruneau M, Chang SE, Eguchi RT, Lee GC, O'Rourke TD, Reinhorn AM, Shinozuka M, Tierney K, Wallace WA, Von Winterfeldt D, 2003 *A framework to quantitatively assess and enhance the seismic resilience of communities. Earthquake spectra* 19(4):733–752.
- Daganzo CF, Gayah VV, Gonzales EJ, 2011 *Macroscopic relations of urban traffic variables: Bifurcations, multivaluedness and instability. Transportation Research Part B: Methodological* 45(1):278–288.
- Dakos V, Kéfi S, 2022 *Ecological resilience: What to measure and how. Environmental Research Letters* 17(4):043003.
- Dantsuji T, Fukuda D, Zheng N, 2021 *Simulation-based joint optimization framework for congestion mitigation in multimodal urban network: a macroscopic approach. Transportation* 48:673–697.
- Folke C, 2006 *Resilience: The emergence of a perspective for social ecological systems analyses. Global Environ Change* 16(3):253–267.
- Folke C, Carpenter SR, Walker B, Scheffer M, Chapin T, Rockström J, 2010 *Resilience thinking: integrating resilience, adaptability and transformability. Ecology and society* 15(4).
- Gao S, Li D, Zheng N, Hu R, She Z, 2022 *Resilient perimeter control for hyper-congested two-region networks with mfd dynamics. Transportation Research Part B: Methodological* 156:50–75.
- Geroliminis N, Daganzo CF, 2008 *Existence of urban-scale macroscopic fundamental diagrams: Some experimental findings. Transportation Research Part B: Methodological* 42(9):759–770.
- Gunderson LH, 2000 *Ecological resilience—in theory and application. Annual review of ecology and systematics* 425–439.
- Haddad J, 2015 *Robust constrained control of uncertain macroscopic fundamental diagram networks. Transportation Research Part C* 59(OCT.):323–339.
- Haddad J, Geroliminis N, 2012 *On the stability of traffic perimeter control in two-region urban cities. Transportation Research Part B: Methodological* 46(9):1159–1176.
- Haddad J, Mirkin B, 2020 *Resilient perimeter control of macroscopic fundamental diagram networks under cyberattacks. Transportation Research Part B: Methodological* 132:44–59.
- Haddad J, Zheng Z, 2020 *Adaptive perimeter control for multi-region accumulation-based models with state delays. Transportation Research Part B: Methodological* 137:133–153.
- Holling CS, 1973 *Resilience and stability of ecological systems. Annual review of ecology and systematics* 1–23.
- Holling CS, 1996 *Engineering resilience versus ecological resilience. Engineering within ecological constraints* 31(1996):32.

-
- Hosseini S, Barker K, Ramirez-Marquez JE, 2016a *A review of definitions and measures of system resilience. Reliability Engineering & System Safety* 145:47–61.
- Hosseini S, Barker K, Ramirez-Marquez JE, 2016b *A review of definitions and measures of system resilience. Reliability Engineering & System Safety* 145:47–61.
- Huang HJ, Xia T, Tian Q, Liu TL, Wang C, Li D, 2020a *Transportation issues in developing china's urban agglomerations. Transport Policy* 85:A1–A22.
- Huang Y, Xiong J, Sumalee A, Zheng N, Lam W, He Z, Zhong R, 2020b *A dynamic user equilibrium model for multi-region macroscopic fundamental diagram systems with time-varying delays. Transportation Research Part B: Methodological* 131:1–25.
- Johari M, Keyvan-Ekbatani M, Leclercq L, Ngoduy D, Mahmassani HS, 2021 *Macroscopic network-level traffic models: Bridging fifty years of development toward the next era. Transportation Research Part C: Emerging Technologies* 131:103334.
- Khwais M, Haddad J, 2022 *Optimal presignal control for two-mode traffic at isolated signalized intersections. Transportation science* 57(2):376–398.
- Kouvelas A, Saeedmanesh M, Geroliminis N, 2023 *A linear-parameter-varying formulation for model predictive perimeter control in multi-region mfd urban networks. Transportation Science* 57(6):1496–1515.
- Laval JA, Leclercq L, Chiabaut N, 2017 *Minimal parameter formulations of the dynamic user equilibrium using macroscopic urban models: Freeway vs city streets revisited. Transportation research procedia* 23:517–530.
- Li Y, Yildirimoglu M, Ramezani M, 2021 *Robust perimeter control with cordon queues and heterogeneous transfer flows. Transportation Research Part C: Emerging Technologies* 126:103043.
- Liao KH, 2012 *A theory on urban resilience to floods-a basis for alternative planning practices. Ecology and society* 17(4).
- Mariotte G, Leclercq L, Laval JA, 2017 *Macroscopic urban dynamics: Analytical and numerical comparisons of existing models. Transportation Research Part B: Methodological* 101:245–267.
- Martin-Breen P, Anderies JM, 2011 *Resilience: A literature review* .
- Mohajerpoor R, Cai C, Ramezani M, 2023 *Optimal traffic signal control of isolated oversaturated intersections using predicted demand. IEEE Transactions on Intelligent Transportation Systems* 24(1):815–826.
- O'Neill RV, Deangelis DL, Waide JB, Allen TF, Allen GE, 1986 *A hierarchical concept of ecosystems* (Princeton University Press).
- Pimm SL, 1984 *The complexity and stability of ecosystems. Nature* 307(5949):321–326.
- Ramezani M, Haddad J, Geroliminis N, 2015 *Dynamics of heterogeneity in urban networks: aggregated traffic modeling and hierarchical control. Transportation Research Part B: Methodological* 74:1–19.
- Ratschan S, She Z, 2010 *Providing a basin of attraction to a target region of polynomial systems by computation of lyapunov-like functions. SIAM Journal on Control and Optimization* 48(7):4377–4394.

- Rölfer L, Celliers L, Abson D, 2022 *Resilience and coastal governance: knowledge and navigation between stability and transformation. Ecology and Society* 27(2).
- Scheffer M, Hosper SH, Meijer ML, Moss B, Jeppesen E, 1993 *Alternative equilibria in shallow lakes. Trends in ecology & evolution* 8(8):275–279.
- Scoones I, Stirling A, Abrol D, Atela J, Charli-Joseph L, Eakin H, Ely A, Olsson P, Pereira L, Priya R, et al., 2020 *Transformations to sustainability: combining structural, systemic and enabling approaches. Current Opinion in Environmental Sustainability* 42:65–75.
- She Z, Xue B, 2014 *Discovering multiple lyapunov functions for switched hybrid systems. SIAM Journal on Control and Optimization* 52(5):3312–3340.
- She Z, Zhang A, Lu J, Hu R, Sam Ge S, 2020 *Design proportional-integral-derivative/proportional-derivative controls for second-order time-varying switched nonlinear systems. International Journal of Robust and Nonlinear Control* 30(5):1979–2000.
- Skafidas E, Evans RJ, Savkin AV, Petersen IR, 1999 *Stability results for switched controller systems. Automatica* 35(4):553–564.
- Su Z, Chow AH, Zheng N, Huang Y, Liang E, Zhong R, 2020 *Neuro-dynamic programming for optimal control of macroscopic fundamental diagram systems. Transportation Research Part C: Emerging Technologies* 116:102628.
- Tilman D, Downing JA, 1994 *Biodiversity and stability in grasslands. Nature* 367(6461):363–365.
- Tsitsokas D, Kouvelas A, Geroliminis N, 2023 *Two-layer adaptive signal control framework for large-scale dynamically-congested networks: Combining efficient max pressure with perimeter control. Transportation Research Part C: Emerging Technologies* 152:104128.
- Walker B, Holling CS, Carpenter SR, Kinzig A, 2004 *Resilience, adaptability and transformability in social–ecological systems. Ecology and society* 9(2).
- Walker B, Salt D, 2012 *Resilience thinking: sustaining ecosystems and people in a changing world* (Island press).
- Wang S, She Z, Ge SS, 2020a *Estimating minimal domains of attraction for uncertain nonlinear systems. IEEE Transactions on Systems, Man, and Cybernetics: Systems* .
- Wang S, She Z, Ge SS, 2020b *Inner-estimating domains of attraction for nonpolynomial systems with polynomial differential inclusions. IEEE transactions on cybernetics* .
- Wang S, Wu W, Lu J, She Z, 2021 *Inner-approximating domains of attraction for discrete-time switched systems via multi-step multiple lyapunov-like functions. Nonlinear Analysis: Hybrid Systems* 40:100993.
- Willems JC, 1971 *The generation of lyapunov functions for input-output stable systems. SIAM Journal on Control* 9(1):105–134.
- Yang K, Menendez M, Zheng N, 2019 *Heterogeneity aware urban traffic control in a connected vehicle environment: A joint framework for congestion pricing and perimeter control. Transportation Research Part C: Emerging Technologies* 105:439–455.

-
- Yang K, Zheng N, Menendez M, 2018 *Multi-scale perimeter control approach in a connected-vehicle environment. Transportation Research Part C: Emerging Technologies* 94:32–49.
- Zeng G, Gao J, Shekhtman L, Guo S, Lv W, Wu J, Liu H, Levy O, Li D, Gao Z, et al., 2020 *Multiple metastable network states in urban traffic. Proceedings of the National Academy of Sciences* 117(30):17528–17534.
- Zeng G, Li D, Guo S, Gao L, Gao Z, Stanley HE, Havlin S, 2019 *Switch between critical percolation modes in city traffic dynamics. Proceedings of the National Academy of Sciences* 116(1):23–28.
- Zeng X, Yu Y, Yang S, Lv Y, Sarker MNI, 2022 *Urban resilience for urban sustainability: Concepts, dimensions, and perspectives. Sustainability* 14.
- Zhang Z, 2006 *Qualitative theory of differential equations*, volume 101 (American Mathematical Soc.).
- Zheng X, She Z, Liang Q, Li M, 2018 *Inner approximations of domains of attraction for a class of switched systems by computing lyapunov-like functions. International Journal of Robust and Nonlinear Control* 28(6):2191–2208.
- Zhong R, Cai H, Xu D, Chen C, Sumalee A, Pan T, 2020a *Dynamic feedback control of day-to-day traffic disequilibrium process. Transportation Research Part C: Emerging Technologies* 114:297–321.
- Zhong R, Chen C, Huang Y, Sumalee A, Lam W, Xu D, 2018a *Robust perimeter control for two urban regions with macroscopic fundamental diagrams: A control-lyapunov function approach. Transportation Research Part B: Methodological* 117:687–707.
- Zhong R, Huang Y, Chen C, Lam W, Xu D, Sumalee A, 2018b *Boundary conditions and behavior of the macroscopic fundamental diagram based network traffic dynamics: A control systems perspective. Transportation Research Part B: Methodological* 111:327–355.
- Zhong R, Xie X, Luo J, Pan T, Lam W, Sumalee A, 2020b *Modeling double time-scale travel time processes with application to assessing the resilience of transportation systems. Transportation research part B: methodological* 132:228–248.

Appendix A: Global phase portrait and attraction region for four-equilibria system

we will consider the four-equilibria cases, derive its qualitative characteristics under CPC (u_1 and u_2), and further provide an inner and outer estimations of attraction regions. Specifically, local stability verification of the four-equilibria system will be shown in App. A.1; global phase portrait derivation is performed in App. A.2; and spontaneous attraction region estimation of four-equilibria system will be included in App. A.3.

A.1. Local stability verification

According to Condition (\mathbb{K}^4), we have:

$$\begin{aligned} u_2 d_2 + d_1 - (1 - u_1 u_2) G_{1,max} &< 0, \\ u_1 d_1 + d_2 - (1 - u_1 u_2) G_{2,max} &< 0. \end{aligned} \quad (22)$$

For system (1) satisfying (22), the four equilibria are denoted as $P_m^4 = (p_{m,1}^4, p_{m,2}^4)$, where $m = 1, 2, 3, 4$, $p_{m,1}^4 = \frac{p_1 + (-1)^m \sqrt{p_1^2 - \frac{4d_1 + 4d_2 u_2}{a_1(1-u_1 u_2)}}}{2}$; $p_{m,2}^4 = \frac{p_2 - \sqrt{p_2^2 - \frac{4d_2 + 4d_1 u_1}{a_2(1-u_1 u_2)}}}{2}$ when $m = 1, 2$ and $p_{m,2}^4 = \frac{p_2 + \sqrt{p_2^2 - \frac{4d_2 + 4d_1 u_1}{a_2(1-u_1 u_2)}}}{2}$ when $m = 3, 4$.

We first verify the local stability of the four equilibria for system (1) satisfying (22). Under Condition ($\mathbb{K}^4 \wedge \mathbb{H}$), we have the following proposition for its four equilibria.

PROPOSITION 2. *Under Condition ($\mathbb{K}^4 \wedge \mathbb{H}$), for system (1), P_1^4 is a locally stable node, P_2^4 and P_3^4 are saddle points, P_4^4 is an unstable node.*

Proof: For system (1), we can get the derivative operator $A|_{P_m^4}$ ($m = 1, 2, 3, 4$) at the equilibrium P_m^4 as follows:

$$A|_{P_m^4} = Df|_{P_m^4} = \begin{pmatrix} \frac{\partial F_1(n_1, n_2)}{\partial n_1} & \frac{\partial F_1(n_1, n_2)}{\partial n_2} \\ \frac{\partial F_2(n_1, n_2)}{\partial n_1} & \frac{\partial F_2(n_1, n_2)}{\partial n_2} \end{pmatrix} \Big|_{P_m^4} = \begin{pmatrix} 2a_1(p_{m,1}^4 - \frac{p_1}{2}) & -2u_2 a_2(p_{m,2}^4 - \frac{p_2}{2}) \\ -2u_1 a_1(p_{m,1}^4 - \frac{p_1}{2}) & 2a_2(p_{m,2}^4 - \frac{p_2}{2}) \end{pmatrix}.$$

Thus, the two eigenvalues $\lambda_{m,j}$ ($j = 1, 2$) of $A|_{P_m^4}$ satisfy:

$$\lambda_{m,j}^2 - 2 \left[a_1(p_{m,1}^4 - \frac{p_1}{2}) + a_2(p_{m,2}^4 - \frac{p_2}{2}) \right] \lambda_{m,j} + 4(1 - u_1 u_2) a_1 a_2 (p_{m,1}^4 - \frac{p_1}{2})(p_{m,2}^4 - \frac{p_2}{2}) = 0. \quad (23)$$

Note that the discriminant Δ_m for Eq. (23) is:

$$\Delta_m = 4 \left[a_1(p_{m,1}^4 - \frac{p_1}{2}) + a_2(p_{m,2}^4 - \frac{p_2}{2}) \right]^2 - 16(1 - u_1 u_2) a_1 a_2 (p_{m,1}^4 - \frac{p_1}{2})(p_{m,2}^4 - \frac{p_2}{2}).$$

1. For $P_1^4 = (p_{1,1}^4, p_{1,2}^4)$, we can get $\Delta_1 > 0$, then Eq. (23) has two real roots $\lambda_{1,1}$ and $\lambda_{1,2}$. Moreover, we have: $\lambda_{1,1} + \lambda_{1,2} = 2 \left[a_1(p_{1,1}^4 - \frac{p_1}{2}) + a_2(p_{1,2}^4 - \frac{p_2}{2}) \right] < 0$, $\lambda_{1,1} \lambda_{1,2} = 4(1 - u_1 u_2) a_1 a_2 (p_{1,1}^4 - \frac{p_1}{2})(p_{1,2}^4 - \frac{p_2}{2}) > 0$, which implies $\lambda_{1,1} < 0, \lambda_{1,2} < 0$. Thus, we can conclude the equilibrium point P_1^4 is a locally stable node.
2. For $P_2^4 = (p_{2,1}^4, p_{2,2}^4)$, we can get $\Delta_2 > 0$, then Eq. (23) has two real roots $\lambda_{2,1}$ and $\lambda_{2,2}$, where $\lambda_{2,1} < \lambda_{2,2}$. Moreover, we have: $\lambda_{2,1} \lambda_{2,2} = 4(1 - u_1 u_2) a_1 a_2 (p_{2,1}^4 - \frac{p_1}{2})(p_{2,2}^4 - \frac{p_2}{2}) < 0$, which implies $\lambda_{2,1} < 0 < \lambda_{2,2}$. Thus, we have that the equilibrium point P_2^4 is a saddle point.
3. For $P_3^4 = (p_{3,1}^4, p_{3,2}^4)$, we also have $\Delta_3 > 0$, then Eq. (23) has two real roots $\lambda_{3,1}$ and $\lambda_{3,2}$, where $\lambda_{3,1} < \lambda_{3,2}$. Moreover, we have: $\lambda_{3,1} \lambda_{3,2} < 0$, which indicates $\lambda_{3,1} < 0 < \lambda_{3,2}$. Thus, P_3^4 is a saddle point.
4. For $P_4^4 = (p_{4,1}^4, p_{4,2}^4)$, we have $\Delta_4 > 0$, Moreover, the two real roots $\lambda_{4,1}$ and $\lambda_{4,2}$ of Eq. (23) satisfy $\lambda_{4,1} + \lambda_{4,2} > 0$, $\lambda_{4,1} \lambda_{4,2} > 0$, which implies $\lambda_{4,1} > 0, \lambda_{4,2} > 0$. Thus, P_4^4 is an unstable node.

□

A.2. Global phase portrait derivation

Subsequently, for the four-equilibria system (1) under Condition $(\mathbb{K}^4 \wedge \mathbb{H})$, the global phase portrait will be derived.

First letting $x_1(t) = n_1(t) - p_{1,1}^4$ and $x_2(t) = n_2(t) - p_{1,2}^4$, we simplify system (1) as:

$$\begin{aligned}\frac{dx_1(t)}{dt} &= -u_2 a_2 (x_2 - s_2)^2 + a_1 (x_1 - s_1)^2 + M_1, \\ \frac{dx_2(t)}{dt} &= -u_1 a_1 (x_1 - s_1)^2 + a_2 (x_2 - s_2)^2 + M_2,\end{aligned}\tag{24}$$

where $s_1 = \frac{1}{2} \sqrt{p_1^2 - \frac{4d_1 + 4u_2 d_2}{a_1(1-u_1 u_2)}}$, $s_2 = \frac{1}{2} \sqrt{p_2^2 - \frac{4d_2 + 4u_1 d_1}{a_2(1-u_1 u_2)}}$, $M_1 = d_1 + u_2 \frac{a_2 p_2^2}{4} - \frac{a_1 p_1^2}{4}$, and $M_2 = d_2 + u_1 \frac{a_1 p_1^2}{4} - \frac{a_2 p_2^2}{4}$. Obviously, the corresponding four equilibria of system (24) are $\hat{P}_1^4 = (0, 0)$, $\hat{P}_2^4 = (2s_1, 0)$, $\hat{P}_3^4 = (0, 2s_2)$ and $\hat{P}_4^4 = (2s_1, 2s_2)$. Note that the four equilibria of the original system (1) are $P_1^4 = (\frac{p_1 - 2s_1}{2}, \frac{p_2 - 2s_2}{2})$, $P_2^4 = (\frac{p_1 + 2s_1}{2}, \frac{p_2 - 2s_2}{2})$, $P_3^4 = (\frac{p_1 - 2s_1}{2}, \frac{p_2 + 2s_2}{2})$, and $P_4^4 = (\frac{p_1 + 2s_1}{2}, \frac{p_2 + 2s_2}{2})$. Moreover, since $M_1 + u_2 M_2 = d_1 + u_2 d_2 - (1 - u_1 u_2) G_{1,max}$ and $M_2 + u_1 M_1 = d_2 + u_1 d_1 - (1 - u_1 u_2) G_{2,max}$, we have that Condition \mathbb{K}^4 (or inequality (22)) holds if and only if Condition $(\hat{\mathbb{K}}^4)$:

$$\begin{aligned}M_1 + u_2 M_2 &< 0, \\ M_2 + u_1 M_1 &< 0,\end{aligned}\tag{25}$$

holds. Further, Condition $(\hat{\mathbb{K}}^4)$ can be divided into five sub-conditions:

- (1) Condition $(\hat{\mathbb{K}}_1^4)$: $M_1 < 0 \wedge M_2 < 0$;
- (2) Condition $(\hat{\mathbb{K}}_2^4)$: $M_1 = 0 \wedge M_2 < 0$
- (3) Condition $(\hat{\mathbb{K}}_3^4)$: $M_1 < 0 \wedge M_2 = 0$
- (4) Condition $(\hat{\mathbb{K}}_4^4)$: $M_1 > 0 \wedge M_2 < \min \left\{ -\frac{M_1}{u_2}, -u_1 M_1 \right\}$;
- (5) Condition $(\hat{\mathbb{K}}_5^4)$: $M_1 < \min \left\{ -u_2 M_2, -\frac{M_2}{u_1} \right\} \wedge M_2 > 0$

Thus in the following, we will discuss the global qualitative characteristics and attraction region for equivalence system (24) under Condition $(\hat{\mathbb{K}}_i^4 \wedge \mathbb{H})$ respectively, where $i = 1, 2, \dots, 5$.

To begin with, we consider the phase portrait under Condition $(\hat{\mathbb{K}}_1^4 \wedge \mathbb{H})$, which can be partitioned into four sub-Conditions: $(\hat{\mathbb{K}}_1^4 \wedge \mathbb{H}_1)$, $(\hat{\mathbb{K}}_1^4 \wedge \mathbb{H}_2)$, $(\hat{\mathbb{K}}_1^4 \wedge \mathbb{H}_3)$ and $(\hat{\mathbb{K}}_1^4 \wedge \mathbb{H}_4)$.

First consider Condition $(\hat{\mathbb{K}}_1^4 \wedge \mathbb{H}_1)$. Following the steps in Sec. 3.2, we have that: the demarcation lines are $\frac{(x_1 - s_1)^2}{\frac{M_1}{a_1}} - \frac{(x_2 - s_2)^2}{\frac{M_2}{a_2}} = 1$ and $\frac{(x_2 - s_2)^2}{\frac{M_2}{a_2}} - \frac{(x_1 - s_1)^2}{\frac{M_2}{u_1 a_1}} = 1$, portrayed as the red and blue dotted curve respectively in Fig. 16(a). In addition, we have $\frac{dx_1(t)}{dt} = 0$ and $\frac{dx_2(t)}{dt} = (1 - u_1 u_2) a_2 x_2(t) (x_2(t) - 2s_2)$ on these two red curves, indicating $\frac{dx_2(t)}{dt} > 0$ when $x_2(t) < 0$ or $x_2(t) > 2s_2$ holds and $\frac{dx_2(t)}{dt} < 0$ when $0 < x_2(t) < 2s_2$ holds. Similarly, we have $\frac{dx_2(t)}{dt} = 0$ and $\frac{dx_1(t)}{dt} = (1 - u_1 u_2) a_1 x_1(t) (x_1(t) - 2s_1)$ on these two blue curves, implying $\frac{dx_1(t)}{dt} > 0$ when $x_1(t) < 0$ or $x_1(t) > 2s_1$ holds and $\frac{dx_1(t)}{dt} < 0$ when $0 < x_1(t) < 2s_1$ holds. Obviously, we can obtain nine unbounded regions in \mathbb{R}^2 divided by these four curves. Moreover, Table 3 summarizes the symbols of $\frac{dx_i(t)}{dt}$ ($i = 1, 2$) in these nine regions. On the basis of Table 3, the phase portrait of (24) under Condition $(\hat{\mathbb{K}}_1^4 \wedge \mathbb{H}_1)$ can be obtained, as shown in Fig. 16(a). Subsequently, based on the phase portrait 5(a), by utilizing proof by contradiction, we can verify that regions B, G and F are positive invariant sets. Since the trajectories starting from B, G and F will not escape, there exist no close orbits for system (24) under Condition $(\hat{\mathbb{K}}_1^4 \wedge \mathbb{H}_1)$.

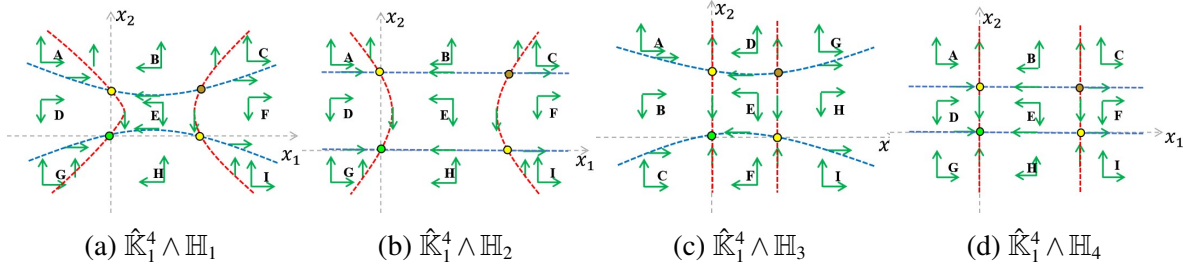


Figure 16 Theoretical schematic phase portraits of system (24) under Condition $(\hat{\mathbb{K}}_1^4 \wedge \mathbb{H})$. Green circle: desired uncongested stable equilibrium. Yellow circle: saddle equilibrium. Yellow-brown circle: unstable equilibrium. Red dotted curves: $\dot{x}_1 = 0$, blue dotted curves: $\dot{x}_2 = 0$, green arrows: trajectory directions.

Table 3 Symbols of the nine regions for system (24) under Condition $\hat{\mathbb{K}}_1^4 \wedge \mathbb{H}_1$.

| Derivative | Symbol in the region | | | | | | | | |
|----------------------|----------------------|---|---|---|---|---|---|---|---|
| | A | B | C | D | E | F | G | H | I |
| $\frac{dx_1(t)}{dt}$ | + | - | + | + | - | + | + | - | + |
| $\frac{dx_2(t)}{dt}$ | + | + | + | - | - | - | + | + | + |

Then, for Conditions $(\hat{\mathbb{K}}_1^4 \wedge \mathbb{H}_2)$, $(\hat{\mathbb{K}}_1^4 \wedge \mathbb{H}_3)$ and $(\hat{\mathbb{K}}_1^4 \wedge \mathbb{H}_4)$, we can also simplify the system (24) and then perform the above analysis. In a similar way, we can obtain four corresponding curves under each Condition, which separate \mathbb{R}^2 to nine unbounded regions. Then the corresponding phase portraits of (24) under these three Conditions can be acquired, as shown in Figs. 16(b), 16(c) and 16(d). Further, we can also obtain the positive invariant sets under each Condition, which verify that there is no close orbit for system (24) under Conditions $(\hat{\mathbb{K}}_1^4 \wedge \mathbb{H}_2)$, $(\hat{\mathbb{K}}_1^4 \wedge \mathbb{H}_3)$ and $(\hat{\mathbb{K}}_1^4 \wedge \mathbb{H}_4)$. Thus, there exists no close orbit, for the system (1) under Condition $\hat{\mathbb{K}}_1^4 \wedge \mathbb{H}$.

A.3. Spontaneous attraction region estimation

Based on the nonexistence of close orbits and Fig. 16, we will next analyze the attraction region of the locally stable node P_1^4 . For this purpose, we wish to find certain corresponding separatrices of system (24) under Conditions $(\hat{\mathbb{K}}_1^4 \wedge \mathbb{H}_1)$, $(\hat{\mathbb{K}}_1^4 \wedge \mathbb{H}_2)$, $(\hat{\mathbb{K}}_1^4 \wedge \mathbb{H}_3)$ and $(\hat{\mathbb{K}}_1^4 \wedge \mathbb{H}_4)$. However, due to the increased number of equilibria, it seems very difficult to find certain separatrices directly. Thus, we will first find inner and outer estimations of attraction regions, and then find certain corresponding separatrices under the above four conditions.

To start with, we consider Condition $(\hat{\mathbb{K}}_1^4 \wedge \mathbb{H}_1)$. The two red dotted demarcation lines can be denoted as $x_1 = \hat{r}_i^{4,1}(x_2)$ ($i = 1, 2$), where $\hat{r}_i^{4,1}(x_2) = (-1)^i \sqrt{\frac{u_2 a_2}{a_1} (x_2 - s_2)^2 - \frac{M_1}{a_1}} + s_1$. Similarly, the two blue dotted demarcation lines can be denoted as $x_2 = \hat{b}_i^4(x_1)$ ($i = 1, 2$), where $\hat{b}_i^4(x_1) = (-1)^i \sqrt{\frac{u_1 a_1}{a_2} (x_1 - s_1)^2 - \frac{M_2}{a_2}} + s_2$. Obviously, the vertex of the line $x_1 = \hat{r}_i^{4,1}(x_2)$ is $Ve_i = ((-1)^i \sqrt{-\frac{M_1}{a_1}} + s_1, s_2)$ and the vertex of the line $x_2 = \hat{b}_i^4(x_1)$ ($i = 1, 2$) is $Ve_{i+2} = (s_1, (-1)^{i+2} \sqrt{-\frac{M_2}{a_2}} + s_2)$. Subsequently, in light of Fig. 16(a), we can similarly verify that the region \hat{U}^4 (the light yellow region shown in Fig. 17(a)) is a positive invariant set, where $\hat{U}^4 = \{(x_1, x_2) | x_1 \geq \hat{l}_{out}^2(x_2) \vee x_2 \geq \hat{l}_{out}^1(x_1)\}$ with

$$\hat{l}_{out}^i(x_i) = \begin{cases} \sqrt{\frac{u_i a_i}{a_j} (x_i - s_i)^2 - \frac{M_j}{a_j}} + s_j & x_i < 0 \\ 2s_j & 0 < x_i < 2s_j \end{cases}$$

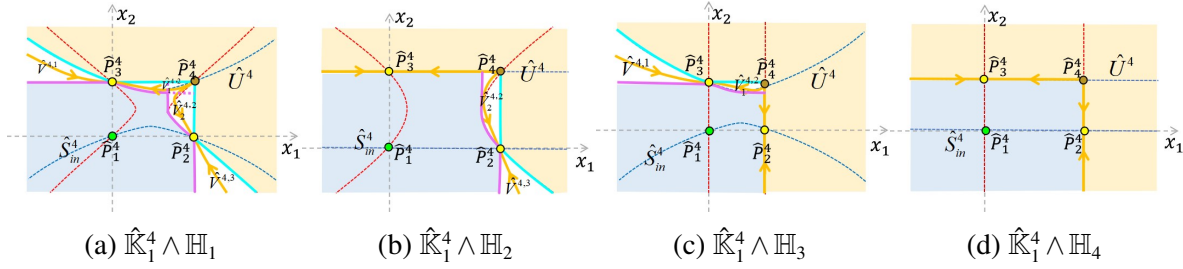


Figure 17 Qualitative characteristics of system (24) ((a)-(d)) and system (1) ((e)-(h)) under Condition $(\mathbb{K}_1^4 \wedge \mathbb{H})$. **Green circle: desired uncongested stable equilibrium. Yellow circle: saddle equilibrium. Yellow-brown circle: unstable equilibrium. Red dotted curves: $\dot{x}_1 = 0$, blue dotted curves: $\dot{x}_2 = 0$, yellow curves: the separatrices, also serving as boundaries of attraction region. Light pink region: attraction region of P_1^4 .**

Moreover, by similar analysis to \hat{U}^{2a} in two-equilibria case, we can arrive that $\mathcal{R}(\hat{P}_1^4) \subset \mathbb{R}^2 \setminus \hat{U}^4$, i.e., $\hat{S}_{out}^4 = \mathbb{R}^2 \setminus \hat{U}^4 = \{(x_1, x_2) | x_1 < \hat{l}_{out}^2(x_2), x_2 < \hat{l}_{out}^1(x_1)\}$ is an outer estimation of attraction region for \hat{P}_1^4 .

In addition, \hat{S}_{in}^4 (the light blue region shown in Fig. 17(a)) is also a positive invariant set, where

$$\hat{S}_{in}^4 = \{(x_1, x_2) | x_1 \leq \hat{l}_{in}^2(x_2), x_2 \leq \hat{l}_{in}^1(x_1)\}$$

with

$$\hat{l}_{in}^i(x_i) = \begin{cases} 2s_j & x_i < 0 \\ \sqrt{\frac{u_i a_i}{a_j} (x_i - s_i)^2 - \frac{M_j}{a_j}} + s_j & 0 < x_i < s_i \\ \sqrt{-\frac{M_j}{a_j}} + s_j & s_i \leq n_2 < 2s_i \end{cases}$$

Further, we can prove that \hat{S}_{in}^4 is an inner estimation of attraction region for \hat{P}_1^4 by following two steps. Firstly, the trajectory starting from any point in \hat{S}_{in}^4 will enter the bounded region $\hat{S}_{in}^4 \wedge \mathbb{R}_1^2$ as $t \rightarrow +\infty$, where

$$\mathbb{R}_1^2 = \left\{ (x_1, x_2) | x_1 \geq -\frac{p_1 - 2s_1}{2}, x_2 \geq -\frac{p_2 - 2s_2}{2} \right\},$$

as we have $\dot{x}_1 > 0$ on the left boundary of $\hat{S}_{in}^4 \wedge \mathbb{R}_1^2$ and $\dot{x}_2 > 0$ on the lower boundary of $\hat{S}_{in}^4 \wedge \mathbb{R}_1^2$. Secondly, the trajectory starting from any point in bounded region $\hat{S}_{in}^4 \wedge \mathbb{R}_1^2$ will go to \hat{P}_1^4 as $t \rightarrow +\infty$, since there is no closed orbit, and there exists only one stable node \hat{P}_1^4 in the bounded region (Zhang (2006)).

As for Conditions $(\mathbb{K}_1^4 \wedge \mathbb{H}_2)$, $(\mathbb{K}_1^4 \wedge \mathbb{H}_3)$ and $(\mathbb{K}_1^4 \wedge \mathbb{H}_4)$, through similar analysis, we can obtain the inner and outer estimations of attraction regions for \hat{P}_1^4 , as shown in the Figs. 17(b), 17(c) and 17(d). Further, letting $n_1(t) = x_1(t) + \frac{p_1 - 2s_1}{2}$ and $n_2(t) = x_2(t) + \frac{p_2 - 2s_2}{2}$, the inner and outer estimations of attraction regions for P_1^4 can be obtained. Denoting $\hat{l}_{in}^i(n_i) = \hat{l}_{in}^i(n_i - \frac{p_i - 2s_i}{2}) + \frac{p_i - 2s_i}{2}$ and $\hat{l}_{out}^i(n_i) = \hat{l}_{out}^i(n_i - \frac{p_i - 2s_i}{2}) + \frac{p_i - 2s_i}{2}$, where $i, j = 1, 2$ and $i \neq j$, we can arrive at the following theorem.

THEOREM 2. Under Condition $(\mathbb{K}_1^4 \wedge \mathbb{H})$, for the local stable point P_1^4 , we have $S_{in}^4 \subset \mathcal{R}(P_1^4) \subset S_{out}^4$, where the inner estimation of attraction region S_{in}^4 and the outer estimation of attraction region S_{out}^4 are defined as follows:

(1) Under Condition $(\mathbb{K}_1^4 \wedge \mathbb{H}_1)$,

$$S_{in}^4 = \{(n_1, n_2) | n_1 \leq \hat{l}_{in}^2(n_2), n_2 \leq \hat{l}_{in}^1(n_1)\}; S_{out}^4 = \{(n_1, n_2) | n_1 \leq \hat{l}_{out}^2(n_2), n_2 \leq \hat{l}_{out}^1(n_1)\}.$$

(2) Under Condition $(\hat{\mathbb{K}}_1^4 \wedge \mathbb{H}_2)$,

$$S_{in}^4 = \left\{ (n_1, n_2) \mid n_1 \leq l_{in}^2(n_2), n_2 < \frac{n_2 + 2s_2}{2} \right\}; S_{out}^4 = \left\{ (n_1, n_2) \mid n_1 \leq l_{out}^2(n_2), n_2 < \frac{n_2 + 2s_2}{2} \right\}.$$

(3) Under Condition $(\hat{\mathbb{K}}_1^4 \wedge \mathbb{H}_3)$,

$$S_{in}^4 = \left\{ (n_1, n_2) \mid n_1 < \frac{n_1 + 2s_1}{2}, n_2 \leq l_{in}^1(n_1) \right\}; S_{out}^4 = \left\{ (n_1, n_2) \mid n_1 < \frac{n_1 + 2s_1}{2}, n_2 \leq l_{out}^1(n_1) \right\}.$$

(4) Under Condition $(\hat{\mathbb{K}}_1^4 \wedge \mathbb{H}_4)$, $S_{in}^4 = S_{out}^4 = \left\{ (n_1, n_2) \mid n_1 < \frac{n_1 + 2s_1}{2}, n_2 < \frac{n_2 + 2s_2}{2} \right\}$.

Note that $n_i \geq 0$ ($i = 1, 2$) holds all the time.

Clearly, according to Theorem 2, the inner and outer estimations of attraction regions for P_1^4 under $(\hat{\mathbb{K}}_1^4 \wedge \mathbb{H}_i)$ with $i = 1, 2, 3, 4$ can be obtained, as shown in the Figs. 9(a)–9(d).

Moreover, we will derive the boundaries of the attraction region of P_1^4 under Condition $(\hat{\mathbb{K}}_1^4 \wedge \mathbb{H}_1)$, by finding certain corresponding separatrices located in $\bigcup_{i=1}^3 \hat{V}^{4,i} = \hat{S}_{out}^4 \setminus \hat{S}_{in}^4$ of equivalent systems (24), as shown in Fig. 17(a), where

$$\hat{V}^{4,1} = \{(x_1, x_2) \mid x_1 < 0, \hat{l}_{in}^1(x_1) < x_2 < \hat{l}_{out}^1(x_1)\},$$

$$\hat{V}^{4,3} = \{(x_1, x_2) \mid \hat{l}_{in}^2(x_2) < x_1 < \hat{l}_{out}^2(x_2), x_2 < 0\},$$

and $\hat{V}^{4,2} = \hat{V}_1^{4,2} \vee \hat{V}_2^{4,2}$, where

$$\hat{V}_1^{4,2} = \{(x_1, x_2) \mid 0 < x_1 < 2s_1, \hat{l}_{in}^1(x_1) < x_2 < \hat{l}_{out}^1(x_1)\},$$

$$\hat{V}_2^{4,2} = \{(x_1, x_2) \mid \hat{l}_{in}^2(x_2) < x_1 < \hat{l}_{out}^2(x_2), 0 < x_2 < 2s_2\}.$$

Obviously, we can obtain a stable separatrix $\hat{\Phi}^1(\hat{P}_3^4) \in \hat{V}^{4,1}$ for the saddle point \hat{P}_3^4 and a stable separatrix $\hat{\Phi}^1(\hat{P}_2^4) \in \hat{V}^{4,3}$ for the saddle point \hat{P}_2^4 . Moreover, we can further obtain another stable separatrix $\hat{\Phi}^2(\hat{P}_3^4)$ of \hat{P}_3^4 , which satisfy $\hat{\Phi}^2(\hat{P}_3^4) \in \hat{V}_1^{4,2}$ and $\lim_{t \rightarrow -\infty} \hat{\Phi}^2(\hat{P}_3^4) = \hat{P}_4^4$, by following two steps. Firstly, we can verify that the region $\hat{V}_1^{4,2}$ is a negative invariant set, otherwise there will exist contradiction with the trajectory direction at the boundary line of region $\hat{V}_1^{4,2}$. Secondly, the trajectory starting from any point in bounded region $\hat{V}_1^{4,2}$ will go to \hat{P}_4^4 as $t \rightarrow -\infty$, since there is no closed orbit, and there exists only one unstable node \hat{P}_4^4 in the bounded region (Zhang (2006)). Similarly, we can obtain another stable separatrix $\hat{\Phi}^2(\hat{P}_2^4)$ for \hat{P}_2^4 , which satisfies $\hat{\Phi}^2(\hat{P}_2^4) \in \hat{V}_2^{4,2}$ and $\lim_{t \rightarrow -\infty} \hat{\Phi}^2(\hat{P}_2^4) = \hat{P}_4^4$. Clearly, these four separatrices are exactly the boundaries of the attraction region for \hat{P}_1^4 .

Further, letting $n_1(t) = x_1(t) + \frac{p_1 - 2s_1}{2}$ and $n_2(t) = x_2(t) + \frac{p_2 - 2s_2}{2}$, the attraction region boundary for P_1^4 under Condition $(\hat{\mathbb{K}}_1^4 \wedge \mathbb{H}_1)$ can be obtained. Denoting $\Phi^i(P_2^4)$ ($i = 1, 2$) to be the two stable separatrices of P_2^4 , and $\Phi^j(P_3^4)$ ($j = 1, 2$) to be the two stable separatrices of P_3^4 , the below theorem can be arrived.

THEOREM 3. Under Condition $(\hat{\mathbb{K}}_1^4 \wedge \mathbb{H}_1)$, for the local stable point P_1^4 , we have $S_A^4 = \mathcal{R}(P_1^4)$, where

$$S_A^4 := \{(n_1, n_2) \mid n_i < g_j^4(n_j), i, j = 1, 2, j \neq i\}$$

satisfying $l_{in}^j(n_j) < g_j^4(n_j) < l_{out}^j(n_j)$, and $g_j^4(n_j)$, $j = 1, 2$ are defined as:

$$g_1^4(n_1) = \begin{cases} \Phi^1(P_3^4) & n_1 < \frac{p_1 - 2s_1}{2} \\ \Phi^2(P_3^4) & \frac{p_1 - 2s_1}{2} < n_1 < \frac{p_1 + 2s_1}{2} \end{cases}$$

and

$$g_2^4(n_2) = \begin{cases} \Phi^1(P_2^4) & n_2 < \frac{p_2 - 2s_2}{2} \\ \Phi^2(P_2^4) & \frac{p_2 - 2s_2}{2} < n_2 < \frac{p_2 + 2s_2}{2} \end{cases}$$

with $\lim_{t \rightarrow -\infty} \Phi^2(P_2^4) = P_4^4$ and $\lim_{t \rightarrow -\infty} \Phi^2(P_3^4) = P_4^4$. Note that $n_i \geq 0$ ($i = 1, 2$) holds all the time.

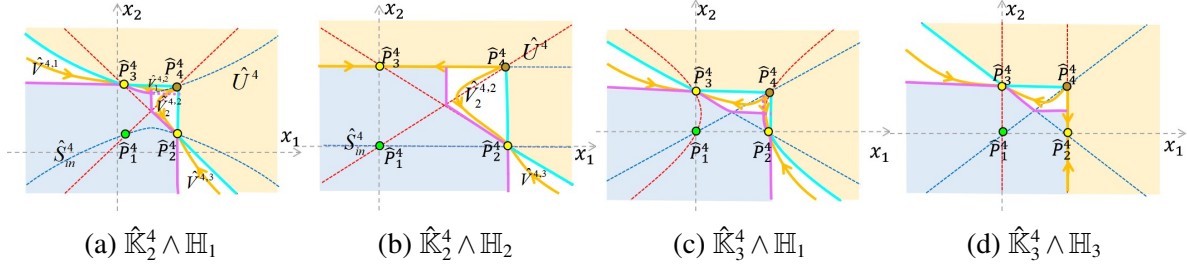


Figure 18 Qualitative characteristics of system (24) under corresponding conditions.

In summary, the attraction region of P_1^4 under corresponding conditions are plotted as light pink zones in the Figs. 9(a)-9(d).

Secondly, we consider Condition $(\hat{\mathbb{K}}_2^4 \wedge \mathbb{H})$, which can be partitioned into two sub-Conditions: $(\hat{\mathbb{K}}_2^4 \wedge \mathbb{H}_1)$ and $(\hat{\mathbb{K}}_2^4 \wedge \mathbb{H}_2)$. Note that $\hat{\mathbb{K}}_2^4 \wedge \mathbb{H}_3 = \emptyset$ and $\hat{\mathbb{K}}_2^4 \wedge \mathbb{H}_4 = \emptyset$. By repeating the analysis as above, the corresponding phase portraits of (24) under these two sub-conditions can be obtained; and further prove that there is no close orbit for system (24) under above two sub-conditions. In addition, we can obtain the inner and outer estimations of attraction regions for \hat{P}_1^4 , and deduce the boundary of attraction region for \hat{P}_1^4 , as shown in the Figs. 18(a) and 18(b). Further, letting $n_1(t) = x_1(t) + \frac{p_1 - 2s_1}{2}$ and $n_2(t) = x_2(t) + \frac{p_2 - 2s_2}{2}$, we can obtain the inner and outer estimations of attraction regions for P_1^4 which are defined in Theorem 2 (1), and the attraction region boundary for P_1^4 under Conditions $(\hat{\mathbb{K}}_2^4 \wedge \mathbb{H}_1)$ and $(\hat{\mathbb{K}}_2^4 \wedge \mathbb{H}_2)$, as shown in Figs. 9(e) and 9(f).

Thirdly, we analyze the phase portrait and the attraction region of P_1^4 under Condition $(\hat{\mathbb{K}}_3^4 \wedge \mathbb{H})$, which can be partitioned into two sub-Conditions: $(\hat{\mathbb{K}}_3^4 \wedge \mathbb{H}_1)$ and $(\hat{\mathbb{K}}_3^4 \wedge \mathbb{H}_3)$. Note that $\hat{\mathbb{K}}_3^4 \wedge \mathbb{H}_2 = \emptyset$ and $\hat{\mathbb{K}}_3^4 \wedge \mathbb{H}_4 = \emptyset$. Notice that Condition $(\hat{\mathbb{K}}_3^4 \wedge \mathbb{H})$ is symmetric to Condition $(\hat{\mathbb{K}}_2^4 \wedge \mathbb{H})$, so the analysis process and results are similar. Thus, we can obtain the inner and outer estimations of attraction regions for \hat{P}_1^4 in a similar way, as shown in Figs. 18(c) and 18(d). Further, letting $n_1(t) = x_1(t) + \frac{p_1 - 2s_1}{2}$ and $n_2(t) = x_2(t) + \frac{p_2 - 2s_2}{2}$, the attraction region of P_1^4 under Conditions $(\hat{\mathbb{K}}_3^4 \wedge \mathbb{H}_1)$ and $(\hat{\mathbb{K}}_3^4 \wedge \mathbb{H}_3)$ can be obtained, as shown in Figs. 9(g) and 9(h).

Fourthly, we consider Condition $(\hat{\mathbb{K}}_4^4 \wedge \mathbb{H})$, which can be partitioned into two sub-Conditions: Condition $(\hat{\mathbb{K}}_4^4 \wedge \mathbb{H}_1)$ and $(\hat{\mathbb{K}}_4^4 \wedge \mathbb{H}_2)$. Note that $\hat{\mathbb{K}}_4^4 \wedge \mathbb{H}_3 = \emptyset$ and $\hat{\mathbb{K}}_4^4 \wedge \mathbb{H}_4 = \emptyset$.

We first consider Condition $(\hat{\mathbb{K}}_4^4 \wedge \mathbb{H}_1)$. For system (24) under Condition $(\hat{\mathbb{K}}_4^4 \wedge \mathbb{H}_1)$, following the steps as Condition $(\hat{\mathbb{K}}_1^4 \wedge \mathbb{H}_1)$, the global phase portrait can be obtained, as shown in Fig. 19(a); further prove that there exist no close orbits; and subsequently derive the inner estimation of attraction region $\hat{S}_{in}^{4,1} = \{(x_1, x_2) | x_1 \leq 2s_1, x_2 \leq \hat{l}_{in}^{1,1}(x_1)\}$ and the outer estimation of attraction region $\hat{S}_{out}^{4,1} = \mathbb{R}^2 \setminus \hat{U}^{4,1} = \{(x_1, x_2) | x_1 \in \mathbb{R}, x_2 < \hat{l}_{out}^{1,1}(x_1)\}$, where

$$\hat{l}_{in}^{1,1}(x_1) = \begin{cases} -\sqrt{\frac{M_1}{u_2 a_2}} + s_2 & x_1 < s_1 \\ -\sqrt{\frac{a_1}{u_2 a_2} (x_1 - s_1)^2 + \frac{M_1}{u_2 a_2}} + s_2 & s_1 < x_1 < 2s_1 \end{cases}$$

and

$$\hat{l}_{out}^{1,1}(x_1) = \begin{cases} \sqrt{\frac{u_1 a_1}{a_2} (x_1 - s_1)^2 - \frac{M_2}{a_2}} + s_2 & x_1 < 0 \\ 2s_2 & 0 < x_1 < 2s_1 \\ -\sqrt{\frac{a_1}{u_2 a_2} (x_1 - s_1)^2 + \frac{M_1}{u_2 a_2}} + s_2 & x_1 > 2s_1 \end{cases}$$

Thus, we will next deduce the boundaries of the attraction region of P_1^4 by finding certain corresponding separatrices located in $\bigcup_{i=3}^4 \hat{V}^{4,i} = \hat{S}_{out}^{4,1} \setminus \hat{S}_{in}^{4,1}$ of equivalent systems (24), as shown in Fig. 19(b), where $\hat{V}^{4,4} =$

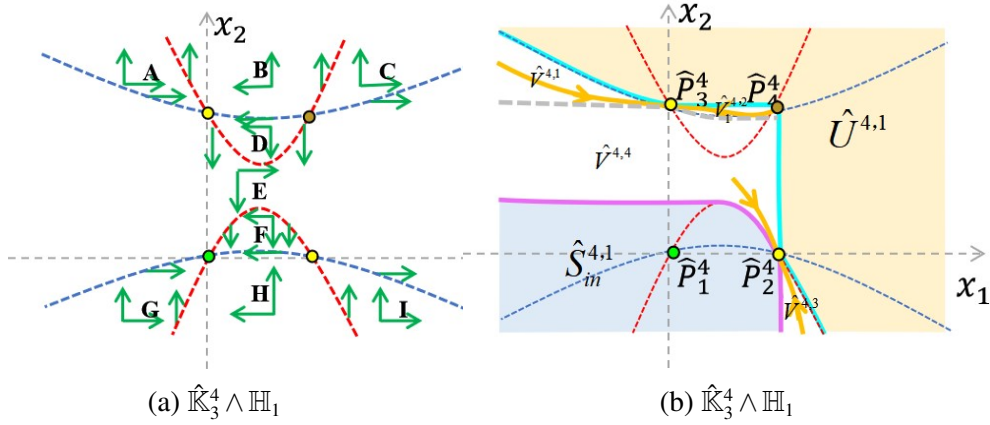


Figure 19 Phase diagram (a) and qualitative characteristics (b) of system (24) under Condition $(\hat{\mathbb{K}}_4^4 \wedge \mathbb{H}_1)$.

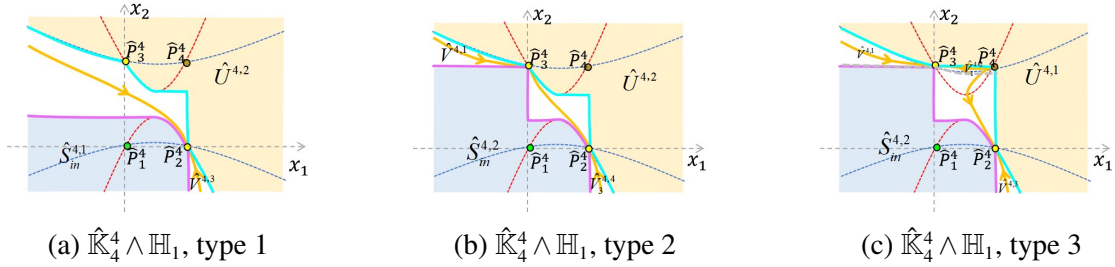


Figure 20 Three types of qualitative characteristics of system (24) ((a)-(c)) and system (1) ((d)-(f)) under Condition $(\hat{\mathbb{K}}_4^4 \wedge \mathbb{H}_1)$.

$\{(x_1, x_2) | x_1 < 2s_1, \hat{l}_{in}^{1,1}(x_1) < x_2 < \hat{l}_{out}^{1,1}(x_1)\}$ and $\hat{V}^{4,3} = \{(x_1, x_2) | x_1 > 2s_1, x_2 < \hat{l}_{out}^{1,1}(x_1)\}$. By similar analysis as above, we can obtain a stable separatrix $\hat{\Phi}^1(\hat{P}_3^4) \in \hat{V}^{4,1}$ for the saddle point \hat{P}_3^4 ; a stable separatrix $\hat{\Phi}^1(\hat{P}_2^4) \in \hat{V}^{4,3}$ for the saddle point \hat{P}_2^4 ; and another stable separatrix $\hat{\Phi}^2(\hat{P}_3^4)$ of \hat{P}_3^4 , which satisfy $\hat{\Phi}^2(\hat{P}_3^4) \in \hat{V}_1^{4,2}$ and $\lim_{t \rightarrow -\infty} \hat{\Phi}^2(\hat{P}_3^4) = \hat{P}_4^4$. Note that $\hat{V}^{4,1}$ and $\hat{V}_1^{4,2}$ are defined above. As for another stable separatrix for \hat{P}_2^4 in $\hat{V}^{4,4}$, there are three types, where in type 1, $\lim_{t \rightarrow -\infty} \hat{\Phi}^2(\hat{P}_2^4) = -\infty$; in type 2, $\lim_{t \rightarrow -\infty} \hat{\Phi}^2(\hat{P}_2^4) = \hat{P}_3^4$; and in type 3, $\lim_{t \rightarrow -\infty} \hat{\Phi}^2(\hat{P}_2^4) = \hat{P}_4^4$; as shown in Figs. 20(a), 20(b) and 20(c), respectively.

Further, we can refine the inner and outer estimations of attraction regions under each type. Specifically, In type 1, the outer estimation of attraction region can be refined as $\hat{S}_{out}^{4,2} = \{(x_1, x_2) | x_1 \in \mathbb{R}, x_2 < \hat{l}_{out}^{1,2}(x_1)\}$, where

$$\hat{l}_{out}^{1,2}(x_1) = \begin{cases} \sqrt{\frac{u_1 a_1}{a_2} (x_1 - s_1)^2 - \frac{M_2}{a_2}} + s_2 & x_1 < 0 \\ \sqrt{\frac{a_1}{u_2 a_2} (x_1 - s_1)^2 + \frac{M_1}{u_2 a_2}} + s_2 & 0 < x_1 < s_1 \\ \sqrt{\frac{M_1}{u_2 a_2}} + s_2 & s_1 < x_1 < 2s_1 \\ -\sqrt{\frac{a_1}{u_2 a_2} (x_1 - s_1)^2 + \frac{M_1}{u_2 a_2}} + s_2 & x_1 > 2s_1 \end{cases}$$

since the region $\hat{V}_1^{4,4} = \hat{S}_{out}^{4,2} \setminus \hat{S}_{out}^{4,1}$ is a negative invariant set and the trajectory starting from any point in bounded region $\hat{V}_1^{4,4}$ will go to \hat{P}_4^4 as $t \rightarrow -\infty$. In type 2, the outer estimation of attraction region can also be refined as $\hat{S}_{out}^{4,2}$ for the same reason. Moreover, the inner estimation of attraction region can be refined as $\hat{S}_{in}^{4,2} = \{(x_1, x_2) | x_1 \in \mathbb{R}, x_2 < \hat{l}_{in}^{1,2}(x_1)\}$,

where

$$\hat{l}_{in}^{1,2}(x_1) = \begin{cases} 2s_2 & x_1 < 0 \\ -\sqrt{\frac{M_1}{u_2 a_2}} + s_2 & 0 < x_1 < s_1 \\ -\sqrt{\frac{a_1}{u_2 a_2} (x_1 - s_1)^2 + \frac{M_1}{u_2 a_2}} + s_2 & s_1 < x_1 < 2s_1 \end{cases}$$

since any trajectory starting from the region $\hat{V}_2^{4,4} = \hat{S}_{in}^{4,1} \setminus \hat{S}_{in}^{4,2}$ will also go to \hat{P}_1^4 as $t \rightarrow +\infty$. In type 3, the inner estimation of attraction region can be refined as $\hat{S}_{in}^{4,2}$ for the same reason.

In summary, the refined inner and outer estimations of attraction regions in each type are obtained, as shown in Figs. 20(a), 20(b) and 20(c). Then, letting $n_1(t) = x_1(t) + \frac{p_1 - 2s_1}{2}$ and $n_2(t) = x_2(t) + \frac{p_2 - 2s_2}{2}$, we can obtain the attraction region, inner and outer estimations of attraction regions in each type of system (1) under Conditions $(\hat{\mathbb{K}}_4^4 \wedge \mathbb{H}_1)$, which are shown in Fig. 20. Moreover, denoting $l_{out}^{1,i}(n_1) = \hat{l}_{out}^{1,i}(n_1 - \frac{p_1 - 2s_1}{2}) + \frac{p_2 - 2s_2}{2}$ and $l_{in}^{1,i}(n_1) = \hat{l}_{in}^{1,i}(n_1 - \frac{p_1 - 2s_1}{2}) + \frac{p_2 - 2s_2}{2}$, where $i = 1, 2$, the below theorem can be arrived.

THEOREM 4. *Under Condition $(\hat{\mathbb{K}}_4^4 \wedge \mathbb{H}_1)$, for the local stable point P_1^4 , we have $S_{in}^4 \subset S_A^4 = \mathcal{B}(P_1^4) \subset S_{out}^4$, where S_A^4 , the inner estimation of attraction region S_{in}^4 and outer estimation of attraction region S_{out}^4 have three types, which are defined as follows:*

- (1) *In type 1: $S_A^4 = \{(n_1, n_2) | n_1 \leq p_1, n_2 < g_3^4(n_1)\}$, where $g_3^4(n_1)$ represents $\Phi^1(P_2^4)$ when $n_1 < \frac{p_1 + 2s_1}{2}$ and $\Phi^2(P_2^4)$ when $\frac{p_1 + 2s_1}{2} < n_1 \leq p_1$;*

$$S_{in}^4 = \{(n_1, n_2) | n_1 \leq p_1, n_2 < l_{in}^{1,1}(n_1)\}; S_{out}^4 = \{(n_1, n_2) | n_1 \leq p_1, n_2 < l_{out}^{1,2}(n_1)\}.$$

- (2) *In type 2: $S_A^4 = \{(n_1, n_2) | n_1 \leq p_1, n_2 < g_4^4(n_1)\}$, where $g_4^4(n_1)$ represents $\Phi^1(P_3^4)$ when $n_1 < \frac{p_1 - 2s_1}{2}$, represents $\Phi^2(P_2^4)$ when $\frac{p_1 - 2s_1}{2} < n_1 < \frac{p_1 + 2s_1}{2}$, and represents $\Phi^1(P_2^4)$ when $\frac{p_1 + 2s_1}{2} < n_1 \leq p_1$;*

$$S_{in}^4 = \{(n_1, n_2) | n_1 \leq p_1, n_2 < l_{in}^{1,2}(n_1)\}; S_{out}^4 = \{(n_1, n_2) | n_1 \leq p_1, n_2 < l_{out}^{1,2}(n_1)\}.$$

- (3) *In type 3: S_A^4 is defined in Theorem 3;*

$$S_{in}^4 = \{(n_1, n_2) | n_1 \leq p_1, n_2 < l_{in}^{1,2}(n_1)\}; S_{out}^4 = \{(n_1, n_2) | n_1 \leq p_1, n_2 < l_{out}^{1,1}(n_1)\}.$$

Note that $n_i \geq 0$ ($i = 1, 2$) holds all the time.

Then, for Conditions $(\hat{\mathbb{K}}_4^4 \wedge \mathbb{H}_2)$, we can also simplify the system (24) and then perform the above analysis. In a similar way, we can obtain the phase portrait for system (24) and further verify that there are no close orbits under Conditions $(\hat{\mathbb{K}}_4^4 \wedge \mathbb{H}_2)$. Thus, we can obtain three types of attraction regions, and further obtain three types of refined the inner and outer estimations of attraction regions under each type, as shown in Figs. 21(a), 21(b) and 21(c). Then letting $n_1(t) = x_1(t) + \frac{p_1 - 2s_1}{2}$ and $n_2(t) = x_2(t) + \frac{p_2 - 2s_2}{2}$, we can obtain three types of attraction regions of (1) under Conditions $(\hat{\mathbb{K}}_4^4 \wedge \mathbb{H}_2)$, as shown in Figs. 9(j), 9(n) and 9(r).

Finally, we analyze the phase portrait and the attraction region of P_1^4 under Condition $(\hat{\mathbb{K}}_5^4 \wedge \mathbb{H})$, which can be partitioned into two sub-Conditions: $(\hat{\mathbb{K}}_5^4 \wedge \mathbb{H}_1)$ and $(\hat{\mathbb{K}}_5^4 \wedge \mathbb{H}_3)$. Note that $\hat{\mathbb{K}}_5^4 \wedge \mathbb{H}_2 = \emptyset$ and $\hat{\mathbb{K}}_5^4 \wedge \mathbb{H}_4 = \emptyset$. Notice that Condition $(\hat{\mathbb{K}}_5^4 \wedge \mathbb{H})$ is symmetric to Condition $(\hat{\mathbb{K}}_4^4 \wedge \mathbb{H})$, so the analysis process and results are similar. By repeating the analysis as above, we can get the refined results under Conditions $(\hat{\mathbb{K}}_5^4 \wedge \mathbb{H}_1)$ and $(\hat{\mathbb{K}}_5^4 \wedge \mathbb{H}_3)$, as shown in Figs. 21 and 9.

Appendix B: Numerical verification of the Global phase portrait and attraction region

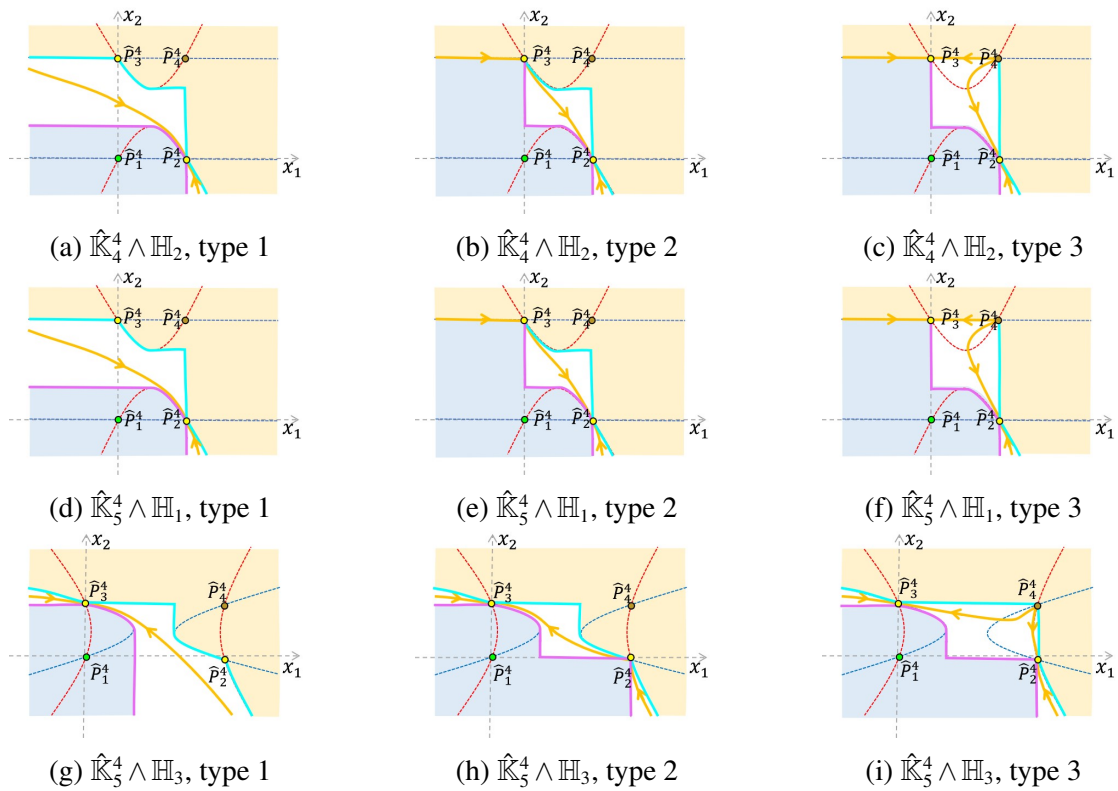


Figure 21 Three types of qualitative characteristics of system (24) under corresponding condition.

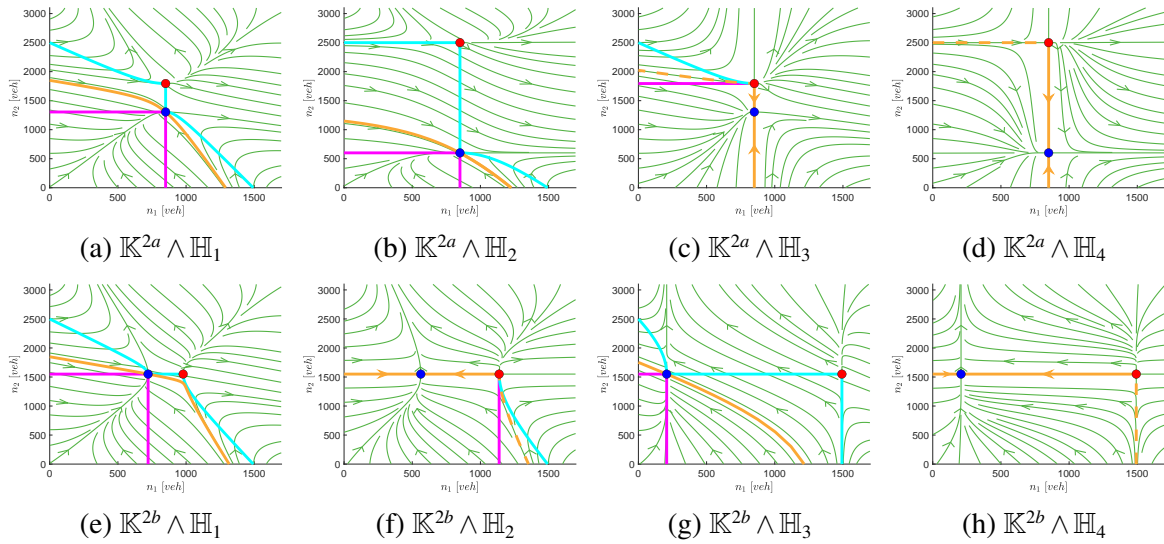


Figure 22 Numerical simulation phase portraits for system (1) under Condition under Conditions (\mathbb{K}^{2a}) and (\mathbb{K}^{2b}). Red circle: undesired saddle-node equilibrium. Blue circle: desired uncongested saddle-node equilibrium. Green line with arrows: the trajectories. Purple line and light blue line represent the inner and outer estimations of attraction regions, respectively. The yellow lines represent the numerical attraction region boundaries, solid yellow lines indicating the boundary line belongs to attraction region, while dashed yellow lines indicating the boundary line does not belong to attraction region. The agreement of this figure with Figs. 7 and Fig. 8 validate the theoretical analysis.

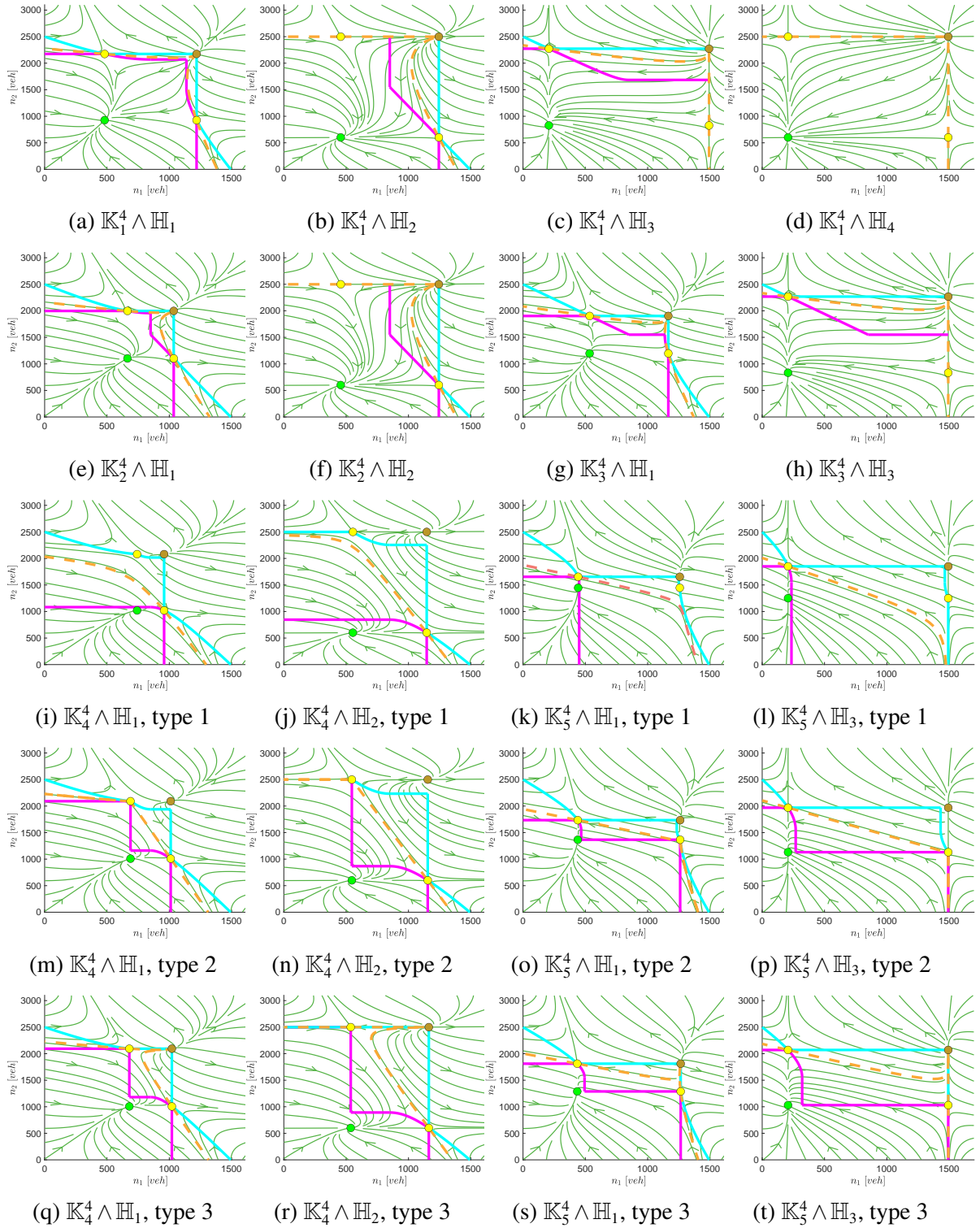


Figure 23 Numerical simulation phase portraits for system (1) under Condition (\mathbb{K}^4). Green circle: desired uncongested stable equilibrium. Yellow circle: saddle equilibrium. Yellow-brown circle: unstable equilibrium. Green line with arrows: the trajectories. Purple line and light blue line represent the inner and outer estimations of attraction regions, respectively. The yellow lines represent the numerical attraction region boundaries, solid yellow lines indicating the boundary line belongs to attraction region, while dashed yellow lines indicating the boundary line does not belong to attraction region. The agreement of this figure with Fig. 9 validate the theoretical analysis.

Table 4 Parameter values for different scenarios

| Scenarios | Flow rates | | Network-outside demands [veh/h] | | Satisfying Condition | Corresponding phase portrait |
|-------------|----------------|--------------|---------------------------------|--------------------------|--|------------------------------|
| Scenario 1 | $u_1 = 0.3$ | $u_2 = 0.4$ | $d_1 = 3 \times 10^4$ | $d_2 = 5 \times 10^4$ | Condition $(\mathbb{K}^{2a} \wedge \mathbb{H}_1)$ | Fig. 22(a) |
| Scenario 2 | $u_1 = 0$ | $u_2 = 0.8$ | $d_1 = 3 \times 10^4$ | $d_2 = 5 \times 10^4$ | Condition $(\mathbb{K}^{2a} \wedge \mathbb{H}_2)$ | Fig. 22(b) |
| Scenario 3 | $u_1 = 0.4$ | $u_2 = 0$ | $d_1 = 7 \times 10^4$ | $d_2 = 5 \times 10^4$ | Condition $(\mathbb{K}^{2a} \wedge \mathbb{H}_3)$ | Fig. 22(c) |
| Scenario 4 | $u_1 = 0$ | $u_2 = 0$ | $d_1 = 7 \times 10^4$ | $d_2 = 5 \times 10^4$ | Condition $(\mathbb{K}^{2a} \wedge \mathbb{H}_4)$ | Fig. 22(d) |
| Scenario 5 | $u_1 = 0.4386$ | $u_2 = 0.48$ | $d_1 = 3 \times 10^4$ | $d_2 = 5 \times 10^4$ | Condition $(\mathbb{K}^{2b} \wedge \mathbb{H}_1)$ | Fig. 22(e) |
| Scenario 6 | $u_1 = 0$ | $u_2 = 0.4$ | $d_1 = 3 \times 10^4$ | $d_2 = 8 \times 10^4$ | Condition $(\mathbb{K}^{2b} \wedge \mathbb{H}_2)$ | Fig. 22(f) |
| Scenario 7 | $u_1 = 0.8$ | $u_2 = 0$ | $d_1 = 0.5 \times 10^4$ | $d_2 = 8 \times 10^4$ | Condition $(\mathbb{K}^{2b} \wedge \mathbb{H}_3)$ | Fig. 22(g) |
| Scenario 8 | $u_1 = 0$ | $u_2 = 0.8$ | $d_1 = 6 \times 10^4$ | $d_2 = 8 \times 10^4$ | Condition $(\mathbb{K}^{2b} \wedge \mathbb{H}_4)$ | Fig. 22(h) |
| Scenario 9 | $u_1 = 0.4$ | $u_2 = 0.4$ | $d_1 = 3 \times 10^4$ | $d_2 = 5 \times 10^4$ | Condition $(\hat{\mathbb{K}}_1^4 \wedge \mathbb{H}_1)$ | Fig. 23(a) |
| Scenario 10 | $u_1 = 0$ | $u_2 = 0.8$ | $d_1 = 5 \times 10^4$ | $d_2 = 1 \times 10^4$ | Condition $(\hat{\mathbb{K}}_1^4 \wedge \mathbb{H}_2)$ | Fig. 23(b) |
| Scenario 11 | $u_1 = 0.8$ | $u_2 = 0$ | $d_1 = 0.2 \times 10^4$ | $d_2 = 5 \times 10^4$ | Condition $(\hat{\mathbb{K}}_1^4 \wedge \mathbb{H}_3)$ | Fig. 23(c) |
| Scenario 12 | $u_1 = 0$ | $u_2 = 0$ | $d_1 = 4 \times 10^4$ | $d_2 = 3 \times 10^4$ | Condition $(\hat{\mathbb{K}}_1^4 \wedge \mathbb{H}_4)$ | Fig. 23(d) |
| Scenario 13 | $u_1 = 0.8$ | $u_2 = 0.8$ | $d_1 = 0.6 \times 10^4$ | $d_2 = 2 \times 10^4$ | Condition $(\hat{\mathbb{K}}_2^4 \wedge \mathbb{H}_1)$ | Fig. 23(e) |
| Scenario 14 | $u_1 = 0$ | $u_2 = 0.8$ | $d_1 = 0.6 \times 10^4$ | $d_2 = 3 \times 10^4$ | Condition $(\hat{\mathbb{K}}_2^4 \wedge \mathbb{H}_2)$ | Fig. 23(f) |
| Scenario 15 | $u_1 = 0.8$ | $u_2 = 0.8$ | $d_1 = 0.3 \times 10^4$ | $d_2 = 2.4 \times 10^4$ | Condition $(\hat{\mathbb{K}}_3^4 \wedge \mathbb{H}_1)$ | Fig. 23(g) |
| Scenario 16 | $u_1 = 0.8$ | $u_2 = 0$ | $d_1 = 4 \times 10^4$ | $d_2 = 2.4 \times 10^4$ | Condition $(\hat{\mathbb{K}}_1^4 \wedge \mathbb{H}_3)$ | Fig. 23(h) |
| Scenario 17 | $u_1 = 0.8$ | $u_2 = 0.8$ | $d_1 = 2 \times 10^4$ | $d_2 = 0.5 \times 10^4$ | Condition $(\hat{\mathbb{K}}_4^4 \wedge \mathbb{H}_1)$ | Fig. 23(i) |
| Scenario 18 | $u_1 = 0.8$ | $u_2 = 0.8$ | $d_1 = 0.78 \times 10^4$ | $d_2 = 1.99 \times 10^4$ | Condition $(\hat{\mathbb{K}}_4^4 \wedge \mathbb{H}_1)$ | Fig. 23(m) |
| Scenario 19 | $u_1 = 0.8$ | $u_2 = 0.8$ | $d_1 = 0.72 \times 10^4$ | $d_2 = 2 \times 10^4$ | Condition $(\hat{\mathbb{K}}_4^4 \wedge \mathbb{H}_1)$ | Fig. 23(q) |
| Scenario 20 | $u_1 = 0$ | $u_2 = 0.8$ | $d_1 = 1.5 \times 10^4$ | $d_2 = 6 \times 10^4$ | Condition $(\hat{\mathbb{K}}_4^4 \wedge \mathbb{H}_2)$ | Fig. 23(j) |
| Scenario 21 | $u_1 = 0$ | $u_2 = 0.8$ | $d_1 = 1.5 \times 10^4$ | $d_2 = 5.6 \times 10^4$ | Condition $(\hat{\mathbb{K}}_4^4 \wedge \mathbb{H}_2)$ | Fig. 23(n) |
| Scenario 22 | $u_1 = 0$ | $u_2 = 0.8$ | $d_1 = 1.5 \times 10^4$ | $d_2 = 5 \times 10^4$ | Condition $(\hat{\mathbb{K}}_4^4 \wedge \mathbb{H}_2)$ | Fig. 23(r) |
| Scenario 23 | $u_1 = 0.8$ | $u_2 = 0.8$ | $d_1 = 0.02 \times 10^4$ | $d_2 = 2.85 \times 10^4$ | Condition $(\hat{\mathbb{K}}_5^4 \wedge \mathbb{H}_1)$ | Fig. 23(k) |
| Scenario 24 | $u_1 = 0.8$ | $u_2 = 0.8$ | $d_1 = 0.02 \times 10^4$ | $d_2 = 2.82 \times 10^4$ | Condition $(\hat{\mathbb{K}}_5^4 \wedge \mathbb{H}_1)$ | Fig. 23(o) |
| Scenario 25 | $u_1 = 0$ | $u_2 = 0.8$ | $d_1 = 0.02 \times 10^4$ | $d_2 = 2.6 \times 10^4$ | Condition $(\hat{\mathbb{K}}_5^4 \wedge \mathbb{H}_1)$ | Fig. 23(s) |
| Scenario 26 | $u_1 = 0.8$ | $u_2 = 0$ | $d_1 = 5 \times 10^4$ | $d_2 = 3.9 \times 10^4$ | Condition $(\hat{\mathbb{K}}_5^4 \wedge \mathbb{H}_3)$ | Fig. 23(l) |
| Scenario 27 | $u_1 = 0.8$ | $u_2 = 0$ | $d_1 = 5 \times 10^4$ | $d_2 = 3.78 \times 10^4$ | Condition $(\hat{\mathbb{K}}_5^4 \wedge \mathbb{H}_3)$ | Fig. 23(p) |
| Scenario 28 | $u_1 = 0.8$ | $u_2 = 0$ | $d_1 = 5 \times 10^4$ | $d_2 = 3 \times 10^4$ | Condition $(\hat{\mathbb{K}}_5^4 \wedge \mathbb{H}_3)$ | Fig. 23(t) |

Note that these are all the scenarios used in this paper. In each scenario, the different formula of the inner and outer estimations of attraction regions are derived (see in Sec. 3), and we have plotted the phase portraits in each scenario, as shown in Figs. 22 and 23.

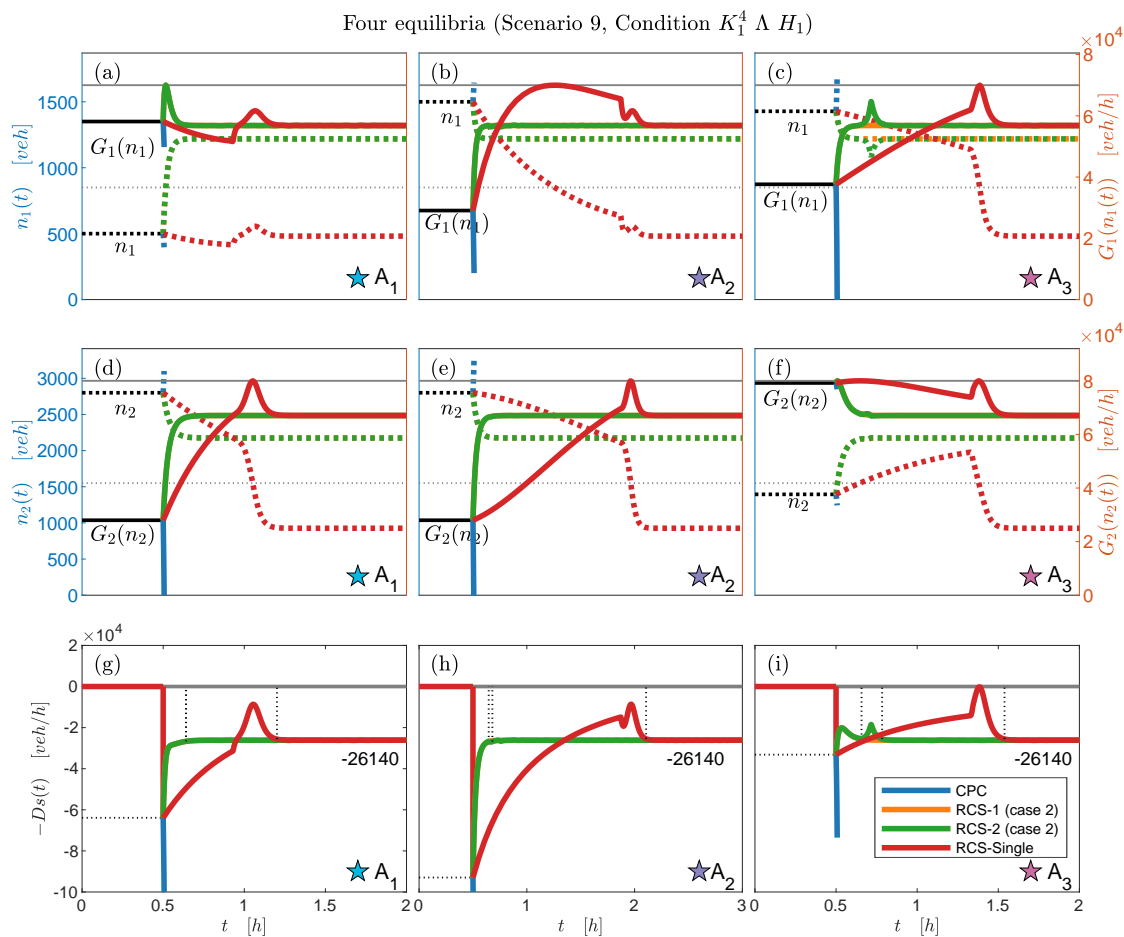


Figure 24 Vehicle accumulations (dotted line) and completion flow rates (solid line) of Region 1 ((a), (b) and (c)) and Region 2 ((d), (e) and (f)). The numerical diagrams of deviation from maximum complete flow $-D_s$ ((g), (h) and (i)) evolving with time t under CPC, RCS-1, RCS-2 and RCS-single. Scenario 9 is considered. Note that for (a)-(f), we employ dual y-axes. The left y-axis represents vehicle accumulation (density), while the right y-axis represents completion flow. Scenario 9 is considered. Here we consider case 2 (in Fig. 15 we consider case 1). Other data settings are the same as Fig. 15.

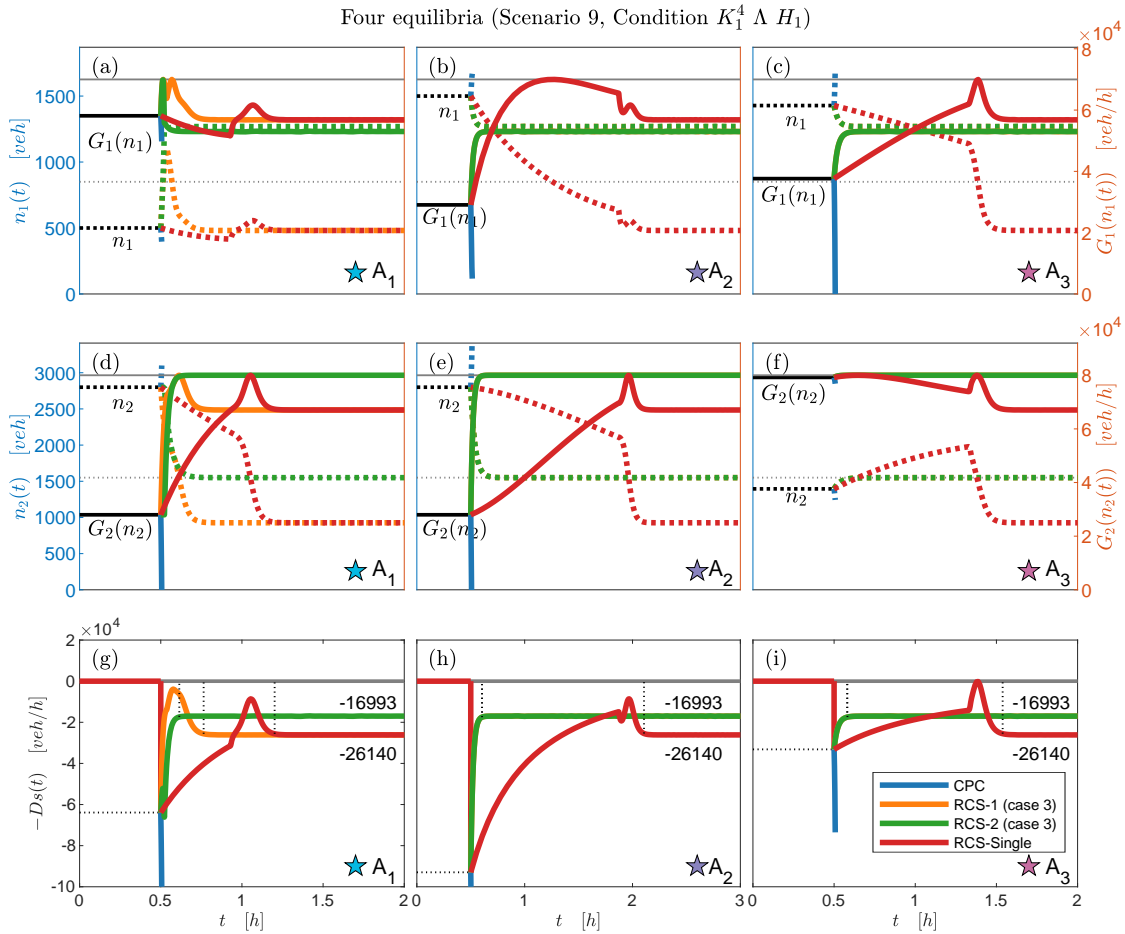


Figure 25 Vehicle accumulations (dotted line) and completion flow rates (solid line) of Region 1 ((a), (b) and (c)) and Region 2 ((d), (e) and (f)). The numerical diagrams of deviation from maximum complete flow $-D_s$ ((g), (h) and (i)) evolving with time t under CPC, RCS-1, RCS-2 and RCS-single. Scenario 9 is considered. Note that for (a)-(f), we employ dual y-axes. The left y-axis represents vehicle accumulation (density), while the right y-axis represents completion flow. Scenario 9 is considered. Here we consider case 3 (in Fig. 15 we consider case 1). Other data settings are the same as Fig. 15.